Mecanosíntesis y caracterización de materiales multiferroicos nanoestructurados

(Mechanosynthesis and characterization of nanostructured multiferroic materials)

Tesis presentada para optar al título de Doctor por:

Eva Gil González

Director-Tutor:

Dr. Luis Allan Pérez Maqueda

Co-director:

Dr. Antonio Perejón Pazo

Instituto de Ciencia de Materiales de Sevilla (ICMSE-CSIC)

Departamento de Química Inorgánica (Universidad de Sevilla)

Sevilla, 2017

A mis padres y familia

AGRADECIMIENTOS

Llega la hora de hacer balance sobre esta etapa de mi vida, que sin duda ha estado marcada por esta tesis doctoral. Por ello, quisiera dedicar unas breves palabras a todas aquellas personas que de una manera u otra han contribuido a la realización de este trabajo y han hecho que el día a día haya sido mucho más agradable y llevadero.

En primer lugar quisiera agradecer a Luis la confianza depositada en mí y el haberme dado la oportunidad de llevar a cabo este proyecto. A Antonio, por la transferencia de conocimiento, su ayuda constante desde el primer hasta el último momento y la gran paciencia que ha demostrado tener. A Pedro, por inculcarme su visión crítica al estudiar la bibliografía científica. A José Manuel Criado, por transmitirme parte de su meticuloso orden y limpieza en el trabajo de laboratorio. Al profesor Michael Hayward de la Universidad de Oxford, por aceptarme en su grupo de investigación y por la caracterización magnética de mis materiales. Al profesor Jan Subrt de la Academia de Ciencias Checa, por la cálida acogida y la atención constante que recibí durante mi estancia en su grupo de investigación. Al personal técnico del ICMSE, por la gran ayuda prestada ante múltiples cuestiones.

También quisiera dedicarle unas palabras a mis compañeros de batalla durante toda mi etapa como investigadora, puesto que de cada uno de ellos he aprendido algo. Para ello seguiré un orden cronológico. Agradezco a los estudiantes de doctorado que comenzamos nuestras carreras científicas simultáneamente en Abengoa Research, particularmente a Pau y Nicolás, ya que las grandes "glorias" sin vosotros

no hubieran sido tan llevaderas. A Verónica Carcelén, por todo lo que aprendí de ella. A mis compañeros de laboratorio de la UAM, Marta, Azin y Moha y a aquellas personas que hicieron que mi estancia en Madrid fuera tremendamente positiva. A Alex y Fon, por ser los mejores compañeros de piso que nadie pueda imaginar.

De manera muy especial a mis compañeros de laboratorio del ICMSE, puesto que con ellos he compartido mi día a día además de infinitas confidencias. A Cristina, por su increíble disposición a ayudar a todo el mundo desinteresadamente y acabar con la lista de nombres de reconocidos científicos. A Rocío, por haberme acompañado en los inicios de esta tesis. A Alma, por sus contrastes tan peculiares y el cariño que se deja coger. A Bea, por alegrarnos los días de trabajo en el laboratorio. A Mónica, por su sentido del humor tan especial que tanto se parece al mío y por ayudarme a sacar las bolas del molino que se me cayeron por el fregadero. A Ernesto, Carlos Latre no te llega ni a las suelas de los zapatos. A Hamid, el hispano-iraní. A los demás compañeros del ICMSE: Juan, Sara, Antonio, Jaime, César y Mariana. A las personas que hicieron que mis estancias en el extranjero fueran memorables: Midori, Rona, Monika, Eva y los coetáneos del NOOC.

A mis amigos: a mi archiconocida Tamara, por nuestra longeva amistad; a Juanma, porque echo de menos salir contigo los fines de semana, fines de año y ferias, ¡vuelve ya!; a Clara, Elena y Gabri, los músicos del Aljarafe; a Jose, por los numerosos planes que hacemos desde que nos conocemos; a Isa, porque el tiempo y la distancia no deteriora nuestra amistad; a Rafa, por sufrir y compartir información sobre los trámites de este programa de Doctorado; a Jaime, por las cervezas en la terracita y las tertulias sobre empleo público.

Por último, a los verdaderamente responsables de que haya llegado hasta aquí, mi familia. A mis padres Miguel y Carmen, por hacerme la vida tremendamente fácil, sin vosotros sencillamente no hubiera sido posible. A mi hermana Irene, por aguantarme y ser la persona a la que más me gusta chinchar. A mis abuelos, por todo el cariño que me habéis dado y me dais, no hay ni un solo día que no piense en vosotros. A mi tía Juana, por corregirme el resumen y mil cosas más. A Carlos, por dedicarme lo más valioso que tiene y que nunca podré devolverle: su tiempo.

A todos vosotros, ¡Gracias de corazón!

RESUMEN

El óxido mixto de hierro y bismuto, $BiFeO_3$, con estructura tipo perovskita, es uno de los materiales magnetoeléctricos más estudiados, ya que a temperatura ambiente presenta simultáneamente propiedades ferroeléctricas y antiferromagnéticas. A pesar de su versatilidad y alto potencial de uso como electrocerámica, su implementación se ve frenada por varios factores, tales como la difícil obtención de fases puras y el débil acoplamiento magnetoeléctrico. Concretamente, es extremadamente difícil la obtención del material libre de fases secundarias mediante procedimentos convencionales, como la reacción en estado sólido a partir de óxidos o carbonatos. Así, los tratamientos prolongados a altas temperaturas empleados en los métodos de síntesis y sinterización tradicionales favorecen la aparición de fases secundarias que, inevitablemente, deterioran las propiedades físicas del material. Por lo tanto, es de gran interés buscar métodos alternativos para la síntesis y sinterización de la perovskita $BiFeO_3$. Asimismo, explorar distintas estrategias para mejorar las propiedades físicas, tales como la sustitución parcial del catión Bi^{3+} por cationes isovalentes de tierras raras (RE^{3+}), también podrían suponer un impulso para la implementación de este material.

Esta tesis doctoral abarca la preparación mediante mecanosíntesis de óxidos mixtos de fórmula general $Bi_{1-x}RE_xFeO_3$ con estructura tipo perovskita, donde el bismuto ha sido sustituido parcialmente por cationes de tierras raras: yterbio y samario. Ambas series ($Bi_{1-x}Yb_xFeO_3$ y $Bi_{1-x}Sm_xFeO_3$) se han caracterizado mediante un análisis exhaustivo de su

estructura cristalina, microestructura, comportamiento en función de la temperatura, así como la evaluación de sus propiedades ópticas, eléctricas y magnéticas. Con respecto a la serie sustituida parcialmente con yterbio, $Bi_{1-x}Yb_xFeO_3$, se ha demostrado que la solubilidad del mismo en el sistema está limitada a una composición de aproximadamente el 3% de sustitución ($x \sim 0.03$). A pesar de la formación de una fase enriquecida en yterbio para composiciones mayores al 3% ($x > 0.03$), las muestras preparadas mediante mecanosíntesis y sinterización convencional resultaron ser eléctricamente homogéneas y muy aislantes a temperatura ambiente. Desafortunadamente, las propiedades magnéticas no pudieron evaluarse adecuadamente, debido a que las fases enriquecidas en yterbio enmascaran los resultados. En cuanto a la serie sustituida con samario, $Bi_xSm_{1-x}FeO_3$, se consiguió preparar muestras puras en un amplio rango de composición ($0.05 \leq x \leq 0.2$). Se comprobó que se obtienen distintas fases cristalográficas puras en función del contenido en samario, permitiendo medir las propiedades físicas de estos materiales sin la posible influencia de fases secundarias. Además, a partir de los datos obtenidos mediante difracción de rayos X, calorimetría diferencial de barrido y análisis de la constante dieléctrica en función de la temperatura se ha propuesto un diagrama de fases para la serie $Bi_{1-x}Sm_xFeO_3$, en el que se demuestra que la fase de alta temperatura en todos los casos es ortorrómbica Pnma. Todas las muestras preparadas por mecanosíntesis y sinterización convencional son eléctricamente homogéneas, altamente aislantes a temperatura ambiente y además exhiben propiedades magnéticas mejoradas, especialmente la composición $x = 0.15$.

En esta tesis doctoral también se ha estudiado la sinterización instantánea (*flash sintering*) de polvos de $BiFeO_3$ preparados mediante mecanosíntesis. Esta técnica de sinterización es relativamente novedosa y permite la densificación de cerámicas en unos pocos segundos y a

temperaturas mucho más bajas que las empleadas en técnicas de sinterización convencionales, gracias a la aplicación de un campo eléctrico. Concretamente, se investiga el efecto de ciertos parámetros experimentales, como el campo eléctrico aplicado y la intensidad de corriente, en la densificación del $BiFeO_3$. En las condiciones óptimas de sinterización instantánea, la muestra resultante de $BiFeO_3$ es pura, densa, nanoestructurada y homogénea eléctricamente.

Como un paso más allá a la sinterización instantánea, esta tesis doctoral también explora la síntesis de $BiFeO_3$ mediante reacción en estado sólido asistida con campo eléctrico a partir de Bi_2O_3 y Fe_2O_3. Se ha estudiado el efecto del campo eléctrico aplicado y la intensidad de corriente límite en la pureza de las muestras obtenidas. Asimismo, se ha investigado el mecanismo de reacción, llegando a la conclusión que tanto la reacción en estado sólido como la densificación del material ocurren simultáneamente. Las muestras de $BiFeO_3$ preparadas en las condiciones óptimas de reacción en estado sólido asistida por campo eléctrico resultaron ser puras, con un tamaño de grano medio de aproximadamente 83 nm y altamente aislantes a temperatura ambiente. Cabe destacar que la reacción en estado sólido asistida con campo eléctrico tiene lugar de manera prácticamente instantánea y a temperaturas mucho más bajas que las empleadas en los métodos de síntesis convencionales basados en reacción en estado sólido. Esto favorece la obtención de materiales puros, libres de fases secundarias, a diferencia de las muestras de $BiFeO_3$ preparadas por métodos convencionales que se recogen en la bibliografía científica.

Por último, se estudia la cinética de cristalización del $BiFeO_3$. La cristalización es un aspecto fundamental con gran influencia en las propiedades finales de los materiales funcionales, como es la perovskita de

$BiFeO_3$. Sin embargo, los estudios de cinética de cristalización de $BiFeO_3$ son escasos. Además, están limitados al análisis de la información obtenida por una sola técnica de caracterización, que generalmente aporta información incompleta y puede dar lugar a la interpretación errónea de los resultados. Por lo tanto, debido a su interés, esta tesis doctoral aborda el estudio de la cinética de cristalización de polvos nanocristalinos de $BiFeO_3$, preparados mediante mecanosíntesis, procesando conjuntamente los datos obtenidos de diferentes técnicas de caracterización: difracción de rayos X en función de la temperatura, microscopía electrónica de transmisión y calorimetría diferencial de barrido.

ABSTRACT

The perovskite oxide $BiFeO_3$ is one of the most studied and promising magnetoelectric materials because it presents ferroelectric and antiferromagnetic order at room temperature. This makes $BiFeO_3$ an interesting and versatile material with potential technological applications. However, there are several issues that are slowing down its implementation in devices, such as its poor magnetoelectric coupling and its difficult preparation. Particularly, the synthesis of phase-pure $BiFeO_3$ by conventional solid-state reaction is extremely tricky. It normally yields impurities and secondary phases due to the required long treatments at high temperatures, which causes a notorious deterioration of the physical properties. Hence, looking for alternative procedures for the synthesis and sintering of $BiFeO_3$, as well as exploring other approaches in order to enhance its physical properties, such as the partial substitution of Bi^{3+} with rare earth isovalent cations (RE^{3+}), are of the most interest.

This thesis encompasses the preparation by mechanosynthesis of rare-earth substituted $BiFeO_3$ systems ($Bi_{1-x}RE_xFeO_3$), where bismuth has been partially substituted by ytterbium and samarium. Both systems ($Bi_{1-x}Yb_xFeO_3$ and $Bi_{1-x}Sm_xFeO_3$) were conventionally sintered and characterized by an exhaustive analysis of the crystal structure, microstructure, temperature dependant behaviour and the evaluation of the optical, electrical and magnetic properties. Regarding the $Bi_{1-x}Yb_xFeO_3$ system, it was found that the solubility limit of ytterbium in $Bi_{1-x}Yb_xFeO_3$ is limited to $x \sim 0.03$. In spite of the amount of ytterbium enriched secondary phases in the samples with $x > 0.03$, they resulted to be electrically

homogenous and highly insulating at room temperature. Unfortunately, the magnetic data interpretation was hampered by the presence of these secondary phases. The samples of the $Bi_xSm_{1-x}FeO_3$ system were successfully prepared by mechanosynthesis, and were also sintered conventionally. X-ray diffraction demonstrates that, basically, single-phase ceramics were obtained, and that the samarium content governs the crystallographic structure of the samples. This allows measuring the physical properties of the samples unencumbered by the presence of secondary phases. Moreover, by a combination of the crystallographic information extracted from X-ray diffraction, DSC and permittivity data, a tentative phase diagram has been constructed, where the presence of the high temperature orthorhombic Pnma phase has been confirmed for the $Bi_xSm_{1-x}FeO_3$ system. All the samples resulted to be electrically homogeneous and highly insulted at room temperature. Moreover, they exhibit enhanced magnetic properties, especially for composition x = 0.15.

This thesis also explores the densification of mechanosynthesized $BiFeO_3$ powders by a novel alternative technique to conventional sintering, denominated flash sintering. This approach allows the densification of ceramics within seconds and at lower furnace temperatures than those employed in conventional sintering, by applying an electric field. The effects of the experimental parameters, such as the applied electric field and the current density, on the densification of $BiFeO_3$ have been investigated. In the optimum flash sintering conditions, the obtained $BiFeO_3$ sample resulted to be phase-pure, highly-dense, with a nanostructured microstructure and electrically homogenous.

Inspired by the flash sintering technique and as a step further, the electric field-assisted solid-state reaction of the pristine oxides, Fe_2O_3 and Bi_2O_3, to prepare $BiFeO_3$ have been addressed. The effects of the applied-

electric field and the current density on the purity of the samples have been investigated. Additionally, the reaction mechanism has been studied, concluding that two processes, the chemical reaction and densification take place simultaneously. The $BiFeO_3$ sample obtained in the optimum experimental conditions of electric field-assisted solid-state reaction resulted to be phase-pure, with an average grain size of approximately of 83 nm and highly insulating at room temperature. It is noteworthy that the applied-electric field solid-state reaction takes place within seconds and at much lower furnace temperatures than those typically employed in conventional solid-state reaction. This favour the preparation of single phase specimens, unlike the $BiFeO_3$ samples prepared by conventional procedures based on solid-state reactions, commonly found in the scientific literature.

Finally, the thermal crystallization kinetics of $BiFeO_3$ has been studied. The crystallization is one key aspect in the resulting properties of functional materials, such as $BiFeO_3$. However, studies of the thermal crystallization kinetics in $BiFeO_3$ are scarce and are limited to the analysis of the information obtained just by one characterization technique. This fact generally gives incomplete information about the crystallization process and can mislead the data interpretation. For this reason, a complete description of the thermal crystallization event of nanocrystalline $BiFeO_3$ has been performed by a combination of the information obtained from three characterization techniques: *in-situ* temperature-dependent X-ray diffraction, transmission electron microscopy and differential scanning calorimetry.

CONTENTS

1. INTRODUCTION

1.1. MULTIFERROIC MATERIALS

Ferroelectricity, ferromagnetism and ferroelasticity are classically known as "ferroic" properties [1]. Ferroelectricity can be described as the property of certain materials to present spontaneous electric polarization, which direction can be switched by an applied field. These materials undergo a phase transition from a high-temperature phase, where the material behaves as an ordinary dielectric, to a low-temperature phase, where the spontaneous polarization appears [2]. Ferromagnetism is analogously described as the property of certain materials to present spontaneous magnetic moment, including any kind of magnetic order (ferromagnetic, antiferromagnetic or ferrimagnetic). Similarly, these materials also present a phase transition from a high-temperate phase that does not have a macroscopic magnetic moment (paramagnetic) to a low-temperature phase that has a spontaneous magnetization even in the absence of an applied magnetic field [3]. By extension, ferroelasticity can be understood as the phenomena in which a material presents spontaneous strain. In an equivalent way to ferroelectricity and ferromagnetism, ferroelastic materials undergo a phase transition from a high-temperature phase to a low-temperature phase, where spontaneous strain appears [4].

The term multiferroism is used to describe materials that present at least two of these defined "ferroic" properties in the same phase [5]. As Figure 1. 1 illustrates, in a "ferroic" material the electric polarization (P), magnetization (M), or strain (Ɛ) are spontaneously created to produce

individually ferroelectricity, ferromagnetism or ferroelasticity, respectively, whereas a multiferroic material combines at least two "ferroic" forms of ordering that leads to additional interactions.

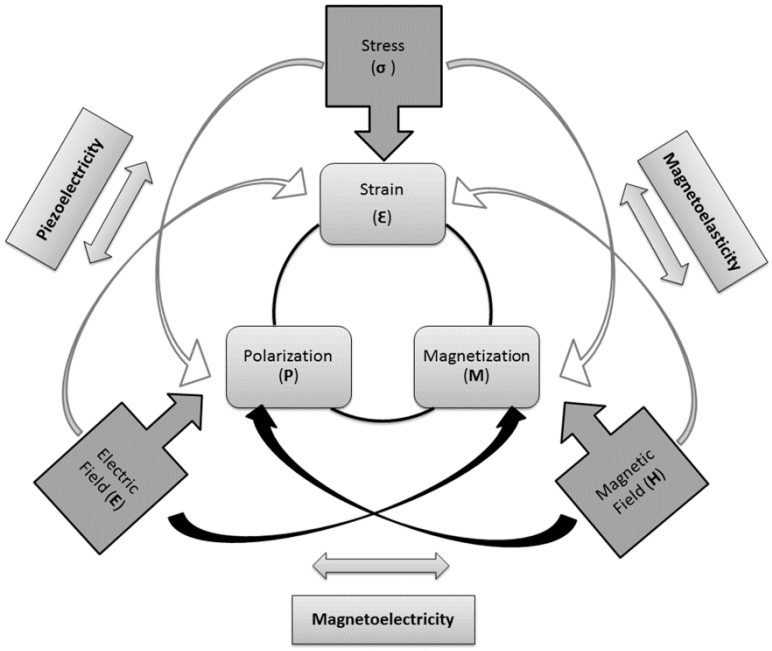

Figure 1. 1. Schematic phase control in ferroic and multiferroic materials.

These additional interactions give rise to materials with interesting properties for different potential technological applications. For example, it is well known that ferroelectric materials display ferroelasticity as well, such us the $PbZr_{1-x}Ti_xO_3$ system, especially for certain values of composition (x). This means that a change in electric polarization implies a change in shape and vice versa, which can prove useful for several applications, such as high-energy electrical pulse generators. Analogously, there are also well known materials that exhibit simultaneously both ferromagnetic and ferroelastic properties, like some amorphous ferromagnetic alloys, which have been proposed for sensor applications

[6]. Materials that combine electrical and magnetic properties in the same phase, known as magnetoelectric multiferroics, have been the target of especially intense research, due to interesting functionalities arising from the interactions between the magnetic and electric polarization. Thus, the application of a magnetic field could be used to control the electric polarization (P), or an electric field to control the magnetization (M), as it is illustrated by the black arrows in the scheme of Figure 1. 1 [3, 7-10].

Although the term multiferroic is quite recent [5], research about magnetoelectric multiferroics dates back to the middle of the twentieth century. The first discovered magnetoelectric material was $Ni_3B_7O_{13}I$ [11]. Later on, intensive research was developed especially in Russia in the second half of the twentieth century looking for magnetoelectric mixed oxides with perovskite structures. However, despite the obvious potential of these kinds of materials and the important effort made, very few materials were actually synthesised. Moreover, those prepared not only exhibited poor coupling between the electrical and magnetic properties but also displayed their multiferroic behaviour only at cryogenic temperatures [12-15]. Those inconveniences made the materials apparently unsuitable for technological applications, which joined to the little understanding of the subjacent nature of the microscopic phenomena, eventually led the scientific community to lose the interest in them. However, since the year 2000 the research about multiferroic materials has seen a sound revival. The number of publications keeps growing by the year as clearly illustrated by Figure 1. 2, which highlights the remarkable growth of publications on the topic within the last 16 years.

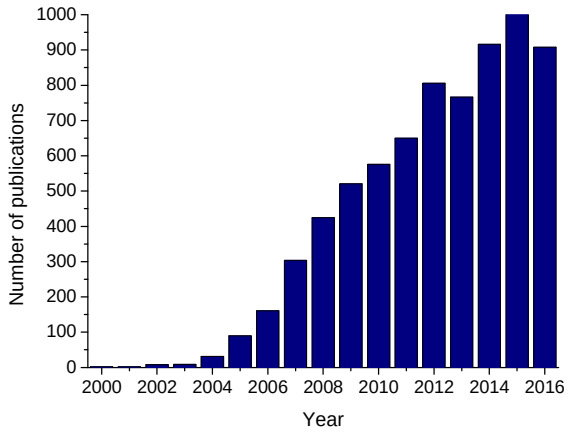

Figure 1. 2. Number of publications per year in the period 2000-2016 using the keyword "multiferroic" in Web of Science (WoS).

The renovated interest in multiferroic materials in the last few years may be motivated by several reasons:

- Multiferroelectricity and ferroganetism can be given together in oxides, although they are seldom met, according to the research carried out by Hill (now Spaldin) [3].
- General improvement and development in methods of synthesis and characterization techniques in material science [16].
- Nowadays trend toward device miniaturization and industrial needs which leads to an increased interest in looking for functional materials with novel properties for new technological applications [7].

1.2. THE PEROVSKITE OXIDE $BiFeO_3$

$BiFeO_3$ is one of the most studied and promising magnetoelectric materials due to its relatively high Néel and Curie temperatures, well above room temperature. The displayed multiferroic behaviour at room temperature makes of $BiFeO_3$ an interesting candidate to be used in practical applications. Research on $BiFeO_3$ started at the end of the fifties of the twentieth century when it was first synthesised [17-25]. However, its properties remained controversial and it wasn't until 2003 when the interest for this material was renewed. Wang et al. reported unexpected high spontaneous electric polarization, of approximately 50-60 μC cm^{-2}, together with very large ferromagnetism of approximately 1.0 Bohr magneton (μ_B) per unit cell, in $BiFeO_3$ thin films [26]. Wang et al.'s findings [26] motivated intensive research in $BiFeO_3$ and related materials, both in thin films and bulk, that still continues nowadays.

1.2.1. $BiFeO_3$ crystal structure

$BiFeO_3$ exhibits a rhombohedral distorted perovskite structure, where Bi^{3+} and Fe^{3+} are in twelvefold and sixfold coordination, respectively [27]. The tolerance factor (t), proposed by Goldschmidt, accounts for the structural distortions from the ideal cubic perovskite (t = 1) with general formula ABO_3, due to the ionic radii of the atoms in the A and B positions [28]. The tolerance factor is described according to equation (1. 1):

$$t = \frac{(r_A + r_O)}{\sqrt{2}(r_B + r_O)} \quad (1.\ 1)$$

Where r_A and r_B are the ionic radii of the ions in the A-site and B-site, and r_O is the ionic radius of the oxygen ion. According to Shannon, the ionic radii of Bi^{3+} in eightfold coordination (the value for twelvefold coordination has not been reported) and Fe^{3+} in sixfold coordination and high spin are 1.17 Å and 0.645 Å, respectively [29]. Hence, the Goldschmidt tolerance factor for $BiFeO_3$ is t = 0.88. When t is smaller than one, the B-O bonds are compressed whereas the A-O are under tension, causing the BO_6 octahedra to tilt co-operatively to relieve the lattice stress [30, 31]. This is directly related to the fact that $BiFeO_3$ exhibits a rhombohedral structure, belonging to the R3c space group at room temperature, rather than the ideal cubic structure [32]. The unit cell has a lattice parameter, a_{rh}, of 3.965 Å and a rhombohedral angle, α_{rh}, of 89.3°–89.48° at room temperature [33]. Additionally, the unit cell can be described with hexagonal symmetry as well, whose lattice parameters values are, a_{hex}= b_{hex} = 5.58 Å and c_{hex} = 13.90 Å [34]. Figure 1. 3 shows the pseudo-cubic representation of the crystal structure diagram of the R3c space-grouped perovskite $BiFeO_3$.

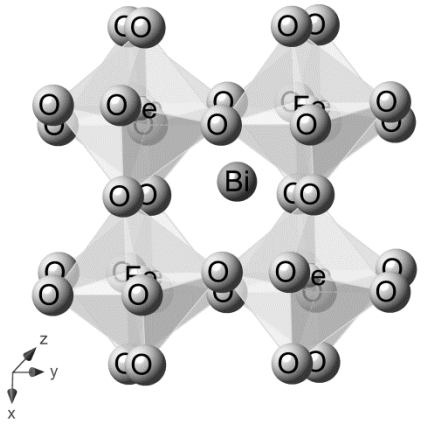

Figure 1. 3. Pseudo-cubic representation of the crystal structure diagram of the R3c space-grouped perovskite $BiFeO_3$.

1.2.2. Multiferroism in $BiFeO_3$

It is well known that bulk $BiFeO_3$ presents ferroelectric and antiferromagnetic order at room temperature. The origin of ferroelectricity in $BiFeO_3$ is caused by the stereochemically active lone-pair orbital of bismuth cation, Bi^{3+} ($6s^2$), that does not participate in the chemical bond and causes the Bi *6p* (empty) orbital to come closer in energy to the O *2p* orbitals. This leads to hybridization between the Bi *6p* and O *2p* orbitals and drives the off-centering of Bi^{3+} with respect to the FeO_6 octahedra, generating spontaneous polarization along the [111] axis of the rhombohedral unit cell [35]. Figure 1. 4 shows schematically how the lone-pair orbital causes the off-centering of Bi^{3+} cation and hence spontaneous polarization.

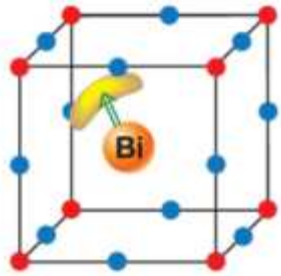

Figure 1. 4. Schematic representation of lone-pair orbital causing the off-centering Bi^{3+} [36].

Additionally, the magnetic order in $BiFeO_3$ is due to the presence of Fe^{3+} cations, a transition metal with partially filled *d* shells ($3d^5$). Each Fe^{3+} spin is surrounded by six antiparallel spins on the nearest Fe neighbours, generating G-type antiferromagnetism [27]. There is a weak canting moment due to the distortion of the FeO_6 octahedra, which does not allow perfect antiparallel alignments of spins and generates a weak magnetic moment in the unit cell. Nevertheless, $BiFeO_3$ presents a long-range

superstructure, incommensurable with the crystallographic structure, which consists of a spin cycloid of the antiferromagnetically ordered sublattices, as it is shown in Figure 1. 5. It is repeated every 62-64 nm with a propagation vector along the [110] direction [37, 38]. This means that, in principle, the net magnetization in crystals with sizes larger than the spin cycloid is zero. However, net magnetization can be achieved by the frustration of the spin cycloid, as it is discussed in Section 1.2.4.

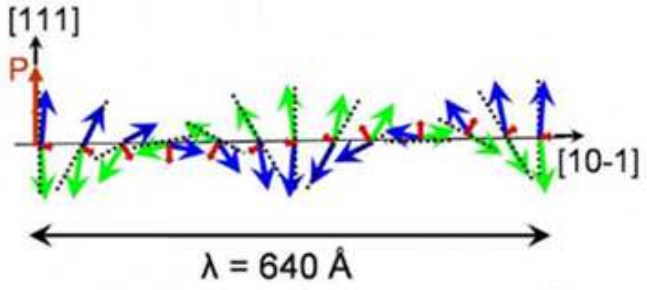

Figure 1. 5. Schematic representation of the spin cycloid [38].

Therefore, due to its multiferroic nature, $BiFeO_3$ exhibits several phase transitions. The room temperature phase of $BiFeO_3$ is also known as α-phase. Upon heating, the first transition is found at approximately 643 K (370 ^oC), corresponding to the Néel Temperature (T_N) [20, 27, 32]. It is a second order phase transition from the antiferromagnetic to the paramagnetic state [34, 39]. At approximately 1098 K (825 ^oC), there is another phase transition associated with the Curie Temperature (T_C). This is a first order phase transition, which is accompanied by an abrupt change in volume and displays a maximum peak in the dielectric constant [40, 41]. It corresponds to a ferroelectric-paraelectric phase transition. Although there was much controversy regarding the crystal structure of this high-temperature phase, commonly known as β-$BiFeO_3$, the centrosymmetric orthorhombic space group Pbnm (equivalent to Pnma)

has been well accepted within the scientific community [27, 39, 42-44]. It was first proposed by Arnold et al., who carried out high-temperature neutron diffraction experiments [43], which are much more accurate than laboratory XRD experiments, especially for the determination of oxygen ions positions. Finally, a third phase transition, which is known as β−γ phase transition, takes place at 1203 K (930 ^{o}C) [40]. The nature of this last transition, as well as its structure has been intensively discussed without yet reaching a clear consensus [45-48]. Nevertheless, it is generally accepted that corresponds to a metal-insulator transition [40].

1.2.3. Potential applications of $BiFeO_3$

Most of the applied research in $BiFeO_3$ has been devoted to explore its multiferroic behaviour. However, there are other potential fields related to different features of $BiFeO_3$. Some of them are listed below:

a) Ferroelectric memories

The first application to come out to the markets probably would be related to the ferroelectric properties of $BiFeO_3$ instead of its multiferroic behaviour. $BiFeO_3$ has a large remnant electric polarization, specifically 100 μC cm^{-2} along the polar [111] direction. This value is twice the remnant electric polarization of the most widely used material in ferroelectric memories, the $PbZr_xTi_{1-x}O_3$ system (PZT) [27]. Moreover, unlike PZT, $BiFeO_3$ is free of lead, which is an additional advantage due to the lower toxicity and the environmental friendly feature. Hence, it is not surprising that ferroelectric memories manufacturers such as FUJITSU (Japan) are considering $BiFeO_3$ as an unchallengeable candidate for the next generation of ferroelectric memory devices [49]. However, some flaws need to be overcome before its implementation, such as thermal

decomposition under applied voltages and its tendency to fatigue in certain direction [27].

b) Spintronic

Due to the multiferroic behaviour of $BiFeO_3$, its introduction in magnetoelectric random access memories (MeRAMs) has been explored [27, 50]. These devices can be read magnetically and written electrically, presenting several advantages over traditional ferroelectric memories. For example, they can be implemented in a solid-state circuit without mobile parts, requiring lower energy [27]. Additionally, the readout process is non-destructive, unlike direct ferroelectric reading, which requires switching the polarization. Nevertheless, more research is required before its implementation, being one of the mayor issues to be overcome that antiferromagnetic domains cannot be easily read [27]. Figure 1. 6 shows a scheme of a feasible MeRAM device based on $BiFeO_3$.

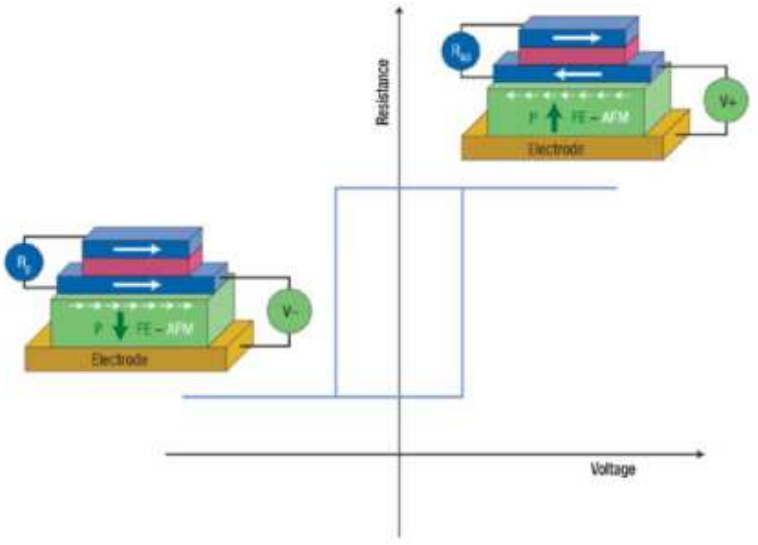

Figure 1. 6. MeRAM based on exchange-bias coupling, proposed by Bibes and Barthelemy [50].

This arrangement has been proposed by Bibes and Barthelemy and, in principle, it would overcome the problem of reading antiferromagnetic domains [50].

c) Photocatalytic applications

$BiFeO_3$ has a small optical band gap (2.1-2.8 eV), which means that can absorb considerable amount of light in the UV-Visible region, in contrast to TiO_2-based photocatalyst, the most widely used material, which is effective just in the UV region due to its relatively large band gap energy (3.2 eV) [51]. Therefore, $BiFeO_3$ is an interesting material to be used in photocatalytic applications. It has been widely reported that $BiFeO_3$ nanoparticles can degrade different organic pollutants in water, such as methyl orange, rhodamine B and methylene blue [52-54]. Photocatalytic hydrogen generation (water splitting) with $BiFeO_3$ thin films has been explored as well [55, 56].

d) Photovoltaic applications

Solar energy harvesting seems to be other potential application of $BiFeO_3$. Photovoltaic cells based on ferroelectric domains of $BiFeO_3$ have also been a subject of enquiry [57-61]. The maximum photovoltage generated at a single ferroelectric junction was determined to be of the order of 10 mV. Photovoltages up to 15 V have been reported with tens to hundreds of ferroelectric domains connected in series [61]. Nevertheless, there are several intrinsic problems related to its efficiency that make difficult its implementation. Furthermore, most photons from the sun have energies below the band gap of $BiFeO_3$ (2.1-2.8 eV) which makes the process even less efficient [62].

e) Gas sensors

Gas sensing properties of materials are generally studied by the comparison of their electrical resistance response in the absence and presence of the target gas. The potential use of $BiFeO_3$ and related materials as gas sensors, for the detection of different organic and inorganic gases, has been investigated. Yu et al. reported in 2009 that $BiFeO_3$ nanoparticles can effectively detect different organic gases, such as acetone and alcohol [63]. Recent studies show good performance of $BiFeO_3$ detecting other gases. For instance, detection of NH_3 has been reported using $BiFeO_3$ synthesized by conventional solid state reaction, although it is noteworthy that there is considerable amount of secondary phases in the resulting material [64]. Sensors for the detection of SO_2 and O_2 based on $BiFeO_3$ and related materials have been recently investigated as well [65, 66].

1.2.4. Challenges in bulk $BiFeO_3$

As it has been mentioned before, in spite of the promising features of $BiFeO_3$, there are some challenges that are slowing down its development for its implementation in practical applications. As thin films are out of the scope of this thesis, we have just focused on bulk $BiFeO_3$. The main obstacle is probably related to the difficulties in the preparation of phase-pure $BiFeO_3$ and related materials. Most employed synthesis methods normally produce impurities, which joined to an intrinsic poor magnetolectric coupling, results in a significant deterioration of the physical properties. This section is devoted to briefly explain the phase diagram and the most common impurities in $BiFeO_3$ as well as how to

overcome the weak magnetoelectric coupling, caused by the incommensurate spin cycloid.

Phase diagram and impurities in $BiFeO_3$

Many works declare the difficulties in preparing phase-pure $BiFeO_3$, without the presence of secondary phases, such as $Bi_{25}FeO_{39}$ and $Bi_2Fe_4O_9$ [47, 67-69]. The key for understanding this issue can be found in the most widely accepted compositional phase diagram, which is depicted in Figure 1. 7 [40]. It is noteworthy to point out that other alternative compositional phase diagrams have been reported, containing certain discrepancies [47, 70-73]. These discrepancies may be related to the intrinsic difficulties in preparing phase-pure materials as well as the non-equilibrium conditions at which the experiments were performed [40, 47]. As it can be inferred from the phase diagram (Figure 1. 7), phase-pure $BiFeO_3$ only exists in a narrow compositional window, hence, slight deviations from the stoichiometry towards the Bi_2O_3 or Fe_2O_3 rich areas would result in a mixture of $BiFeO_3$ with $Bi_{25}FeO_{39}$ or $Bi_2Fe_4O_9$. Additionally, it has been reported that $BiFeO_3$ is actually a metastable phase and that the Gibbs energy differences between $BiFeO_3$ and the decomposition products are so small that in certain conditions $BiFeO_3$ can easily decompose according to the following reaction (1. 2) [68, 69]:

$$49BiFeO_3 \rightarrow Bi_{25}FeO_{39} + 12Bi_2Fe_4O_9 \quad (1.\ 2)$$

Whereas there are discrepancies in the range of temperatures at which $BiFeO_3$ decomposes [67, 69, 71], it is well known that Bi_2O_3 melts at temperatures above 830 ^oC. Hence, synthesis methods which rely on temperatures higher than Bi_2O_3 melting point can lead to materials with uncertain stoichiometry due to bismuth deficiencies with the ensuing

presence of secondary phases and the deterioration of the physical properties of $BiFeO_3$, which is normally translated in low remnant polarization (P_r) and high leakage currents. Specifically, high leakage currents have been attributed to Bi^{3+} deficiencies during the synthesis, which lead to the reduction of Fe^{3+} to Fe^{2+} and the formation of anion and cation vacancies [74-76]. Bi^{3+} ion vacancies can also lead to oxygen vacancy formation which can result in an extra increase of conductivity [77].

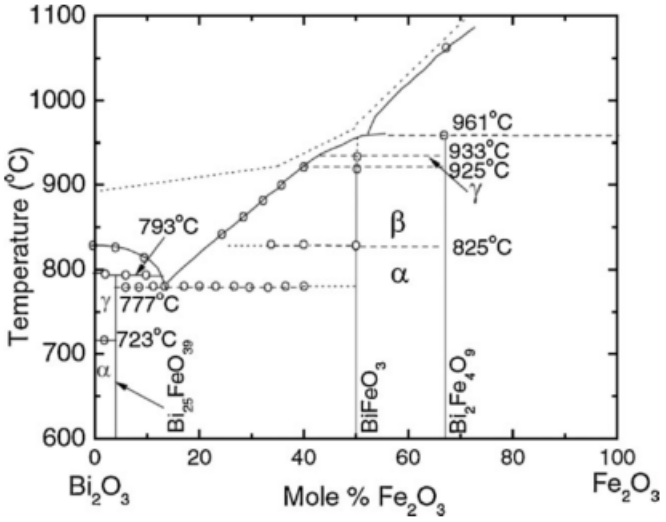

Figure 1. 7. Compositional phase diagram of $BiFeO_3$ modified by Palai et al. [40].

Magnetoelectric coupling and spin cycloid

In addition to the extremely difficult synthesis, $BiFeO_3$ exhibits weak magnetoelectric coupling. The magnetoelectric coupling in $BiFeO_3$ manifests the relationship between ferroelectric polarization and magnetization such as ferroelectric control of magnetism or magnetic control of ferroelectricity. As it was explained in Section 1.2.2, the spin cycloid averages out the net macroscopic magnetization in crystals bigger

than its wavelength (62-64 nm). Nevertheless, there are several strategies to improve the physical properties as well as to overcome the issue of the spin cycloid:

- Applying high magnetic fields: it has been reported that above certain values of magnetic field (~20 Teslas), also known as "critical field" the spin cycloid is destructed and the magnetoelectric polarization change sings and becomes linear dependent of the magnetic field [7, 78].

- Particle size reduction: enhanced magnetization has been reported in nanoparticles with sizes smaller than 92 nm, synthesized by different wet chemical methods [79-84].

- Chemical substitution: this approach is probably the most widely used to improve the magnetic and electrical behaviour and to favour the synthesis of high quality samples. As this is one of the main scopes of this thesis, it will be discussed with more detail in Section 1.2.5. Different substitution strategies have been employed at either A- or B-site cations of the $BiFeO_3$ perovskite, as well as co-substitutions or the preparation of solid solutions with other oxides [85-90]. The partial substitution of Bi^{3+} for isovalent cations, such as rare earths (RE) has attracted special attention [91]. It has been widely reported that the different chemical substitution strategies result in an enhancement of the magnetization, depending on the substituent and composition, which can be correlated to an increase of the magnetocrystalline anisotropy, making the cycloidal spin structure energetically unfavourable [30]. All

seems to be related to the ionic radius of the substituent and the subsequent distortion of the perovskite structure [91, 92].

1.2.5. $Bi_{1-x}A_xFeO_3$ systems (A: isovalent cation)

As it has been introduced, the substitution of Bi^{3+} for isovalent cations is common not only for allowing the synthesis of phase-pure samples but also for the improvement of its ferroelectric properties, the reduction of leakage currents and the enhancement of the magnetoelectric coupling. Additionally, this also offers the possibility of synthesizing materials which compositions are closed to structural morphotropic phase boundaries, which leads to an additional enhancement of the physical properties of the materials [93]. It has been reported that the structural and physical properties strongly depend on the ionic size of the substituent as well as its concentration [92]. Although it is difficult to generalize and further research is required, Arnold proposed a schematic phase diagram for the lanthanide series that relates the ionic radii of the substituents to the phase transformations that the $Bi_{1-x}A_xFeO_3$ systems undergo, as shown in Figure 1. 8. It is concluded that for the largest rare earth ions, an anti-polar Pnam or Pbam phase is stabilized between the R3c space group of the parent compound, $BiFeO_3$, and the Pnma space group of the rare earth orthoferrites, $REFeO_3$. Conversely, for the smallest rare earths ions, phase segregation and co-existence of R3c and Pnma phases are observed rather than the transformation to an intermediate phase.

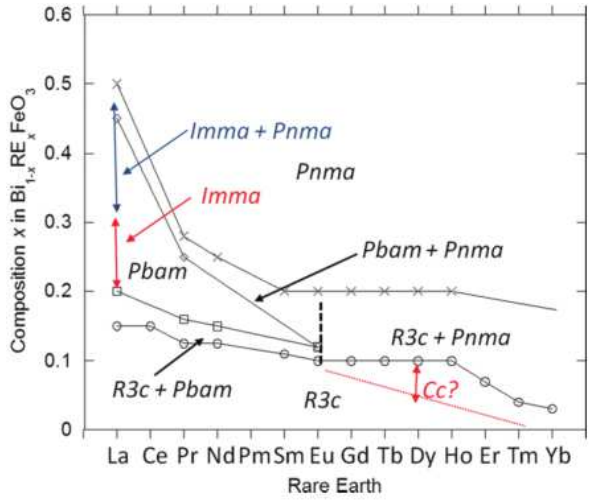

Figure 1. 8. Schematic representation of $Bi_{1-x}RE_xFeO_3$ phase diagram [91].

Additionally, Karimi et al. studied the correlation of the ferroelectric-paraelectric transition temperature (T_C) with the average A-site ionic radii for La^{3+}, Nd^{3+}, Sm^{3+}, and Gd^{3+}-substituted $BiFeO_3$, concluding that as the average A-site ionic radii decreases the T_C declines with a reasonably linear relationship, as can be observed in Figure 1. 9 [94].

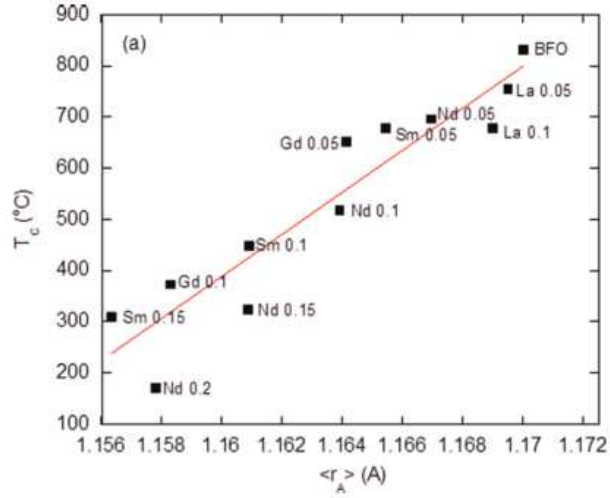

Figure 1. 9. Variation of T_c for some La^{3+}, Nd^{3+}, Sm^{3+}, and Gd^{3+}-substituted $BiFeO_3$ ceramics with average A-site ionic radii, $\langle r_A \rangle$ [94].

Despite these common features within different $Bi_{1-x}RE_xFeO_3$ systems, it is noteworthy to highlight that much controversy can be found in the literature regarding the effects of rare-earth substitution, not only on the physical properties but also on the crystal structure. Thus, many contradictory results have been reported for the same systems. As one of the main scopes of this thesis is to study the effect of Yb^{3+} and Sm^{3+} substitution in $BiFeO_3$, a brief survey of the existing literature for these systems can be found in the introduction of Chapters 4 and 5, respectively.

1.2.6. Synthesis methods of $BiFeO_3$

Due to the notorious difficult preparation of phase-pure $BiFeO_3$ ceramics and related materials such as $Bi_{1-x}RE_xFeO_3$ systems, numerous synthesis methods have been tested. Some of them are listed as follows:

a) Conventional solid-state method

$BiFeO_3$ was first synthesized by conventional solid-state reaction [24]. This method consists in intimately mixing the starting materials in suitable stoichiometric ratios and the subsequent calcination at high temperature to allow the interdiffusion of the reactants. There are several problems regarding the synthesis of $BiFeO_3$ by conventional solid-state reaction. One of them is related to the different diffusion rates of bismuth and iron [95]. For example, at 700 ^oC the tracer diffusion coefficient of Fe^{3+} in Fe_2O_3 (D_{700^oC}~$2.8 \cdot 10^{-25}$ $m^2\ s^{-1}$) is five orders of magnitude lower than that of Bi^{3+} in Bi_2O_3 (D_{700^oC}~$6.8 \cdot 10^{-20}$ $m^2\ s^{-1}$) [96]. Therefore, below 700 ^oC the reaction would be incomplete. Nevertheless, the diffusion rate can be enhanced by increasing the calcination temperature. However, $Bi_{25}FeO_{39}$, which is a reaction intermediate prior to the formation of $BiFeO_3$ from the starting oxides, melts at approximately 793 ^oC. It may cause loss of Bi_2O_3

through segregation of the resulting liquid phase. Thus, the calcination temperature should be limited in principle. Additionally, according to Selbach et al. [69], $BiFeO_3$ is metastable in the temperature region from 447 ^oC up to 767 ^oC, where $Bi_{25}FeO_{39}$ and $Bi_2Fe_4O_9$ have a slightly higher stability than $BiFeO_3$, and it would decompose according to the reaction (1. 2). Therefore, the synthesis of phase-pure $BiFeO_3$ and related materials through solid state reaction seems to be not compatible in terms of temperature range. Other alternative methods have been addressed to overcome this issue.

b) Rapid liquid sintering

Rapid liquid sintering was first reported by Wang et al. for the synthesis of $BiFeO_3$ [76]. This method is basically a modification of the conventional solid-state reaction method explained above. The differences rely on the modification of the calcination step which is just held for a few seconds (450 s) at a temperature of 880 ^oC, with extremely fast heating and cooling rates (~100 $^oC\ s^{-1}$). The authors claimed that as the reaction takes place well above the melting point of Bi_2O_3, the liquid phase together with the fast heating and cooling rates, accelerate the formation of pure $BiFeO_3$, preventing the formation of secondary phases. Nevertheless, the purity of the samples synthesized by this method has been questioned as the reported works just prove the phase purity by means of laboratory XRD, which is not particularly accurate in the detection of small amounts of secondary phases [75, 76, 97, 98].

c) Wet chemical methods

The wet chemical routes have also been widely used in an attempt to synthesize phase-pure $BiFeO_3$ as well as related materials. On the one

hand, chemical methods require much lower temperatures, avoiding the problem of bismuth loss typically found in conventional solid-state reactions. On the other hand, they allow an intimate contact of the reactants in an atomic scale which ensure chemical homogeneity. Control of the particle size, morphology and increase of specific surface area is possible as well. However, these methods are based on complex solution processes or involve toxic precursors. Some of the most employed wet chemical methods are:

- **Sol-gel methods**. They are typically used to prepare metal oxides via the hydrolysis of metal alkoxides in an alcoholic solution, resulting in the corresponding hydroxides. The hydroxide is then calcined and the corresponding oxide is obtained at lower temperatures than those used in conventional solid-sate reactions. Different modified sol-gel techniques, such as modified Pechini method, metal complex or sol-gel based on the glycol reaction, have been used for the preparation of $BiFeO_3$ and related materials [82, 99-105]. Besides their differences, the common feature in sol-gel-based methods are the use of metal salts, such as $Bi(NO_3)_3 \cdot XH_2O$ and $Fe(NO_3)_3 \cdot XH_2O$, dissolved in a diluted acidic media as well as the use of a chelating agent.

- **Solution combustion method**. The starting materials are normally hydrated nitrates of bismuth and iron, which are employed in stoichiometric ratios and act as oxidizers. Water is commonly used as solvent and glycine or urea as fuel. The autocombustion temperatures are below those employed in conventional solid-state reactions and normally depend on the oxidizers/fuel ratio. Once the autocombustion process is

completed and the water is totally evaporated, a gel is formed, which is subsequently burnt, resulting in the final oxide product [79, 106-108].

- **Co-precipitation synthesis.** The scope of these methods is the simultaneous precipitation of previously dissolved reactants under certain conditions of pH, concentration, temperature, etc. A subsequent thermal treatment allows the reaction between the co-precipitated metal hydroxides, giving as a result the final oxide. The most employed starting materials are metal salts, such as hydrated nitrates of bismuth and iron, which are normally dissolved in a solution media, such as ammonium hydroxide. During the precipitation process, the pH and concentration of metal ions should be carefully controlled in order to avoid the precipitation of undesired products [109-114].

- **Hydrothermal and solvothermal synthesis.** Hydrothermal and solvothermal methods have been widely used in the synthesis of advanced materials in the last few years, due to their versatility in terms of compositional and morphological control and the purity of the resulting materials [115]. These techniques are based on the crystallization of substances from aqueous or non-aqueous solutions, whether hydrothermal or solvothermal syntheses are carried out, at a moderate temperature and high vapour pressure. Besides the mentioned advantages, these kinds of methods depend on a considerable number of experimental parameters, such as purity of the staring materials, pH, temperature, pressure, nature of the mineralizer, etc. Particularly for $BiFeO_3$, Han et al. reported that slight variations

on the experimental conditions can result in the formation of $Bi_{25}FeO_{39}$ and $Bi_2Fe_4O_9$ or even in other phases of the Bi_2O_3-Fe_2O_3 system, such as $Bi_{12}Fe_{0.63}O_{18.945}$ [116]. Much effort has been devoted in understanding the influence of the different experimental parameters involved in the synthesis of $BiFeO_3$ and related materials by hydrothermal and solvothermal reactions [116-122]. Microwave-assisted hydrothermal synthesis of $BiFeO_3$ has also been reported as an effective method for the preparation of phase-pure $BiFeO_3$ [123, 124].

- **Sonochemical synthesis.** These methods apply high power ultrasound waves (20 kHz and 10 MHz) in liquid solutions with previously dissolved reactants. The ultrasound waves cause the acoustic cavitation due to the continuous formation, growth and implosive collapse of nanometre solvent bubbles in a liquid. High temperatures are obtained during the collapse of the bubble what induces the break of chemical bonds and the consequent reaction and precipitation of the products. There are a few reports in the literature of $BiFeO_3$ synthesized by sonochemistry [65, 125].

d) Mechanochemistry

Mechanochemistry has been proved to be a successful method for the synthesis of $BiFeO_3$ and related materials [126-130]. The most important features of mechanochemistry are discussed in Section 1.3, as the preparation of $Bi_{1-x}RE_xFeO_3$ systems by mechanochemistry is one of the main objectives of this thesis. Previous reports confirm, by a deep characterization, that by the mechanochemical approach, it is possible to

obtain phase-pure $BiFeO_3$ and related materials [128-130]. The quality of the samples prepared by mechanosynthesis has been evidenced through the study of their electrical properties. Unlike $BiFeO_3$ and related materials prepared by other synthesis techniques [131, 132], the mechanosynthesized materials resulted to be highly insulating at room temperature [128-130], which is essential for a ferroelectric material.

1.3. MECHANOCHEMISTRY

Mechanochemistry is a branch of chemistry which is concerned with chemical and physico-chemical transformations of substances in all states of aggregation produced by the effect of mechanical energy. This definition was given by Heinicke and it is probably the most widely accepted nowadays [133].

The mechanochemical processes are normally carried out in the so-called ball mills, where the energy from the working medium is transferred to the solid through impact strength and shear due to the collisions of the balls with the powders and the friction with the walls of the milling containers. Although somehow mechanochemistry has been present since the Prehistory in human development (fire produced by the shear of stones), it has attracted much attention in the last few years due to its unique features. Starting from an environmental point of view, mechanochemistry is normally a dry process where chemical reactions can be induced without the use of solvents. This makes mechanochemistry more environmental friendly than traditional wet chemical methods, where solvents are totally essential and considerable amount of toxic and harmful by-products are obtained. This fact has been recently highlighted in an informative article of the New York Times by Dr. James Mack of the

University of Cincinnati [134]. Additionally, it is possible to obtain metastable phases such as supersaturated solid solutions, due to the extension of solid solubility, crystalline and quasicrystalline intermediate phases, which can be tricky to prepare by other conventional synthesis methods. Chemical reactions can be given at room temperature and, therefore, the use of high temperatures, typical from solid state reactions, are avoided. It is particularly useful for the synthesis of materials such as $BiFeO_3$, as it has been previously discussed in Section 1.2.4. Moreover, the resulting materials are homogeneously distributed and nanostructured with exceptional high reactivity and sinterability due to the high free energy accumulated in the defective crystal lattice and the increment of grains boundary volume created during the milling process. Additionally, it is a versatile and simple technique that can be applied to prepare and process a wide range of materials like pure metals, ceramics, polymers and composites, normally in one step. Furthermore, the mechanochemical approaches allow a direct scaling-up to industrial production which can be beneficial for the implementation of mechanosynthesized materials into practical applications [135-137].

Despite these advantages, mechanochemical processes depend on a considerable amount of experimental parameters to achieve a desired chemical composition or microstructure. The main experimental variables are commented as follows, as well as its main drawback: i.e. contamination. Considerations about how to overcome, or at least minimize, contamination issues are discussed as well. Additionally, a brief summary about the main theories and models related to the transformation of mechanical energy into chemical energy are also reported.

1.3.1. Process variables

The general idea of a mechanochemical process is quite simple and basically consists in the insertion of the maximum amount of energy into the solid to generate defects and fresh surface area, which greatly affect the chemical reactivity of the solids. However, it is a stochastic process that involves the optimization of a considerable number of parameters to achieve the desired products in terms of chemical composition and microstructure. Some of the most important experimental variables are:

- **Type of mill:** mills are responsible to transfer the energy from the working media into the solid. They differ on their design, capacity, speed of operation, efficiency of milling, and additional parameters, such as their configuration for heat dissipation. Some of the most commonly used are: centrifugal mills, planetary mills, vibration mills and attritor mills. Figure 1. 10 represents the characteristic movements of the mills to transfer the energy to the solids.

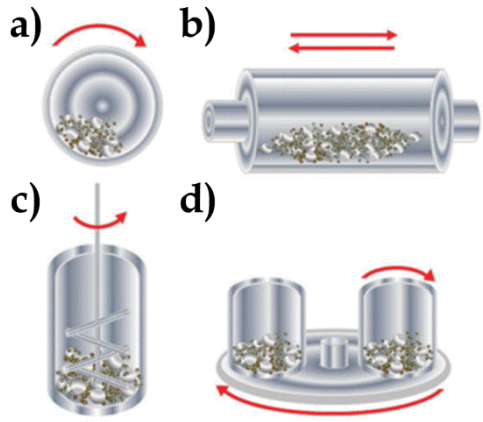

Figure 1. 10. Types of mills a) centrifugal mill, b) vibration mill, c) attritor mill and d) planetary mill. Modified from reference [135].

- **Milling container:** the material and the shape of the milling container are of vital importance to avoid contamination problems and compositional changes in the nominal stoichiometry of the milled products. Due to the milling process some of the container material will be unavoidably incorporated in the resulting products. Some of the most common materials used for milling containers are hardened steel, tool steel, chromium steel, tempered steel, stainless steel, WC-Co, WC-lined steel, bearing steel, agate, alumina, zirconia and silicon nitride.
- **Grinding medium (balls):** Some of the most common materials used as grinding medium are hardened steel, tool steel, hardened chromium steel, tempered steel, stainless steel, WC-Co, bearing steel, agate, alumina, zirconia and silicon nitride. The density must be high enough so that the balls can create enough impact force on the starting materials. The size of the balls is other parameter to take into account and it should be adapted to the size of the milling container. Nevertheless, in general terms bigger diameters produce higher collision energies.

- **Milling speed:** it determines the kinetic energy (KE), designated according to equation (1. 3):

$$KE = \frac{1}{2}mv^2 \quad (1.\ 3)$$

Where m is the mass of the grinding medium and v the velocity at which it is traveling. Hence, the milling speed is one of the most important parameters to be considered. In general terms,

the higher the milling speed, the higher energy input into the materials. However, depending on the design of the mill, there is a critical speed value at which the balls will be pinned to the inner wall of the milling container, due to centrifugal forces, and avoiding the balls to take down. Therefore, it is very important to optimize the milling speed in order to maximize the height at which the balls should take down, and which maximizes the collision energy with the material.

- **Milling time:** this parameter should be optimized depending on the type of mill, speed, ball-to-power ratio, temperature, nature of the materials to be milled etc. Nevertheless, it is noteworthy that milling times longer than those strictly necessary to obtain the desired products can lead to the formation of undesired phases and can contaminate the samples from the grinding medium and milling container.

- **Ball-to-powder weight ratio (BPR):** it is the ratio of weight of balls to the weight of powders. It has been widely varied. Nevertheless, the higher the BPR, the shorter the time required to carry out a milling process. This is due to the fact that at high BPR the number of collisions per unit of time increases and consequently more energy is transferred to the powder. The heat generated, which can significantly influence the milling process, also increases at higher BPR.

- **Extent to filling the vial:** around 50% of the grinding container is left empty. It is important to leave enough free space for the balls and powder to move inside the container so that the impact forces can be maximized. Therefore, it is necessary to

reach a commitment between the production rate and the left space to optimize the energy impact.

- **Milling atmosphere:** a proper control of the milling atmosphere is important to avoid contamination problems. In most cases, mechanochemical processes are carried out under air. However, it is possible to work under inert atmospheres (Ar or He of high purity) to prevent oxidation or contamination of the resulting materials. Reactive atmospheres are also common, such as nitrogen or ammonium for the synthesis of nitrides and hydrogen for hydrides.

- **Process control agents (PCAs):** PCAs are generally organic substances that act as surface-active agents, lowering the surface tension. PCAs can be useful to minimize cold welding and therefore inhibiting agglomeration. This is translated in lower milling times to achieve a specific particle size. The most common PCAs are ethanol, methanol, hexane and stearic acid. The nature and amount of PCAs used during milling depends on its own nature and chemical stability as well as the nature of the starting materials, purity, grinding medium and the desired final product specification such as particle size and yield.

- **Temperature of milling:** unfortunately, most commercial mills do not allow a direct control of this parameter, although milling temperature can significantly influence the diffusivity, reaction kinetics and microstructure of the resulting products [138].

1.3.2. Contamination

One of the major drawbacks of milling, and perhaps the most important, is contamination. The large surface area of the milled products as well as the fresh surface created and the continuous abrasion and shear with the grinding media and milling container contribute to the contamination of the products. Therefore, special precaution must be taken into account. The main sources of contamination have been related to the purity of the starting materials, milling atmosphere, milling container, milling media and the nature of the used PCAs. Some considerations regarding each of them are discussed as follows.

The starting materials should be of high chemical purity. The particle size is also important because lower particle sizes means higher surface areas and thus, the probability of contaminants adsorption, such as nitrogen, oxygen and water vapor, is also higher.

Milling atmosphere plays a major role in the contamination of mechanosynthesized products. Therefore, it is common the use of inert atmospheres such as argon or helium of high purity in hermetic milling containers to avoid air leakage from the exterior. It is necessary to distinguish these processes and mechanosynthesis processes working under reactive atmospheres.

Previous coating with the materials to be milled helps to minimize the contamination from the milling container and milling medium. Moreover, the use of harder materials as milling medium than those to be milled also contributes to minimize the contamination.

PCAs can decompose during the mechanosynthesis process and as they are normally organic compounds, they are an additional source of

impurities, such as carbon, oxygen, nitrogen and hydrogen. Hence, the use of PCAs should be avoided, unless it is strictly necessary.

Other additional precautions can be taken into account in order to minimize contamination. For instance, the number of interruptions, normally to pick up sample to monitor the progress of the reaction, should be minimized as well as milling time that should be just enough to reach the stationary state of the chemical reaction.

1.3.3. Theories and models

Mechanochemistry is a stochastic process that depends on a considerable amount of experimental parameters and its complexity is more than evident. There are a number of common aspects that have been observed in mechanochemical reactions. For instance, a fine and uniform dispersion of the resulting materials, normally on the nanometric scale, are commonly observed in mechanochemical process [137]. However, further from these aspects, how the mechanical energy is transformed to chemical energy is a question that remains unclear. Several theories and models have been developed to try to understand what is really happening during a mechanochemical process, being rather probably that more than one mechanism act together. A brief summary of some theories and models are reported below.

Thermal theory

This theory assumes that the kinetic energy is transformed into thermal energy, being this last the responsible of the induction of the chemical reactions [135, 137]. During the amorphization of the reactants increments of temperature can result in the formation of small liquid areas

which rapidly solidify by contacting the surrounding cold solid. This theory relies more on the formation of "hot-spots". During the friction process between two sliding solids, temperature peaks of over 1000 K in surfaces of about 1 μm^2 can be reached and last for 10^{-4}–10^{-3} s [135]. These high temperatures can be given near the tip of a propagating crack as well, and this may result in the induction of chemical reactions. Urakaev at al. studied the products emitted from a crack propagation through a $NaNO_3$ crystal, concluding that these products are typical of temperatures above 1000 K [139]. Hence, according to this theory, thermal spikes are the responsible of the mechanochemical reactions.

Reactions induced by shear

Plastic deformation is essential for the acceleration of a reaction in a mechanochemical process. The importance of shear was pointed out by Larsen et al. when demonstrated that $K_3Fe(CN)_6$ transformed into $K_4Fe(CN)_6$ not only by the effect of pressure in a Bridgeman anvil but also by applying shear [140]. One of the common characteristic of a mechanochemical process is that the reactants are in intimate contact with each other on the nanometer scale. It means that a large volume of atoms is in the grain boundaries which, in principle, should enhance the diffusion and increase the rate of mechanochemical reaction. Nevertheless, it has been proved that the mass transfer at the first stage of a mechanochemical process is due to rotation of crystal blocks and the formation of defects rather than conventional diffusion process [141]. Figure 1. 11 shows typical defects created during a milling process. The mass transport is accelerated for the increase of defects density during the evolution of the mechanochemical process.

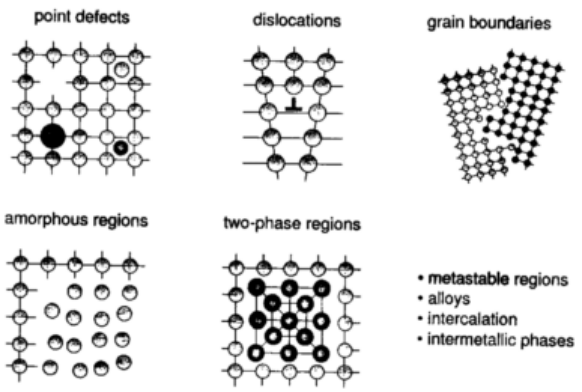

Figure 1. 11. Typical defects created during milling [135].

Magma-plasma model

This model proposes that a huge amount of energy is set free at the contact spot of colliding particles, creating a special plasmatic state [135, 142]. This causes the emission of excited fragments of solids, electrons and photons for a short period of time, as Figure 1. 12 represents. The fresh surface formed is rather disorder, electrically charged and local temperatures of more than 10000 K can be reached. According to this model all these factors may be the responsibles of the induction of chemical reactions.

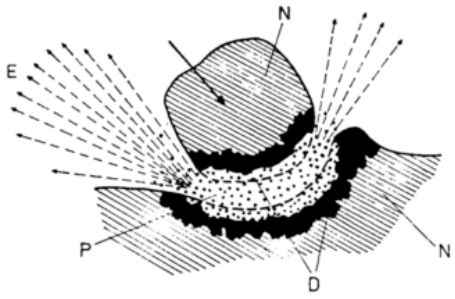

Figure 1. 12. Magma-plasma model: exo-electrons (E), undeformed solid (N), highly deformed surface layer (D), plasma (P) [142].

1.4. SINTERING

Most of the methods described in Section 1.2.6 for the synthesis of $BiFeO_3$ ceramics and related materials yield powders which must be sintered into dense and highly pure pellets. One of the aims of this thesis is to explore the newly developed flash sintering technique to sinter $BiFeO_3$ powders prepared by mechanosynthesis. Hence, a brief introduction about sintering and the existing methods of sintering, focusing on flash sintering, is provided in this section.

1.4.1. General aspects

Sintering is a processing technique used to consolidate particles, normally of metal or/and ceramic powders, with controlled porosity by applying thermal energy at around 2/3 of its melting point. This temperature is normally enough to allow significant atomic mobility and it is typically taken to establish sintering conditions [143, 144].

Sintering is an irreversible thermodynamic process associated with a lowering of the free energy of the system, where basically the main scope of the process is to decrease the surface area. The sources which provide this lowering of free energy are known as driving forces. The driving forces involved in a sintering process are the curvature of the particle surfaces, an externally applied pressure and chemical reaction. The total interfacial/surface energy can be expressed as γA, where γ is the surface energy and A is the total surface area. Hence, the reduction of the total energy is giving according to equation (1. 4):

$$\Delta(\gamma A) = \Delta\gamma A + \gamma \Delta A \quad (1.\ 4)$$

Where the term ΔγA is related to the change in interfacial energy due to densification and γΔ*A* corresponds to the variation of surface area by grain coarsening [144]. Figure 1. 13 schematically depicts densification and coarsening, the basic phenomena giving during the sintering.

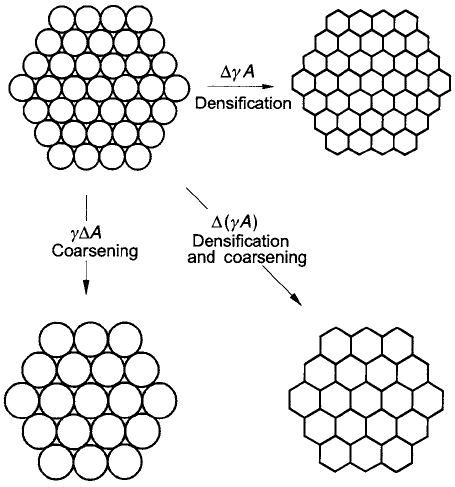

Figure 1. 13. Schematic representation of basic phenomena (densification and coarsening) during sintering [144].

Matter transport and mechanism of sintering

In the absence of an externally applied pressure and chemical reaction, the main driving force is the curvature of the particles. It is generally well accepted that the surface energy is inversely proportional to the radius of the particles. However, the excess of surface energy is a necessary but not a sufficient condition for sintering. Besides the driving forces that initiate the process, diffusional transport of matter, promoted by thermal energy, also takes place. During sintering, atoms move from their original position, areas with higher chemical potential (source), to the neck region between particles, area with lower chemical potential (sink). Matter transport along different paths determines the mechanism of

sintering. Six different mechanisms have been proposed [143, 145], as it is shown in Figure 1. 14 and Table 1. 1. In the initial stages of sintering, the necks are considered to be the sinks for atoms. Hence, according to these mechanisms matter can be transported from the surface, along the surface (1), through the lattice (2) or by vapour transport (3) to the neck regions. Matter can be also transported from grain boundaries along grain boundary (4) or through the lattice (5) to the necks. Alternatively, matter can be transported from dislocations to the necks though plastic flow (6). The contribution of each sintering mechanism to the overall process depends on the material composition, density of grain boundaries and dislocations and temperature. Moreover, densification only happens when the centres of the particles are moved closer together. This is achieved through mechanisms (4), (5) and (6), as the matter is removed from grain boundaries and bulk and it is deposited in the necks. Conversely, mechanisms (1), (2) and (3) yield to grain coarsening through neck growth without pore removal.

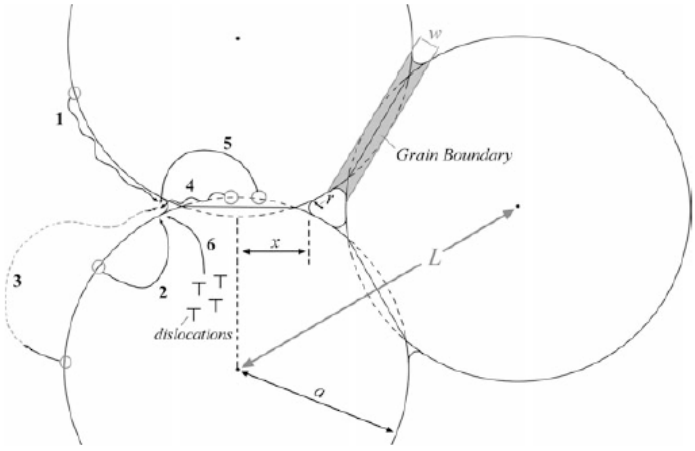

Figure 1. 14. Sintering mechanisms represented by numbers (Table 1. 1) in a three particles array [143].

Table 1. 1. Mechanism of sintering illustrated in Figure 1. 14.

Number	Mechanism	Source	Sink
1	Surface diffusion	Surface	Neck
2	Lattice Diffusion	Surface	Neck
3	Vapor transport	Surface	Neck
4	Grain boundary	Grain boundary	Neck
5	Lattice diffusion	Grain boundary	Neck
6	Plastic flow	Dislocation	Neck

Stages of sintering

A typical densification curve versus time can be observed in Figure 1. 15, where the three different stages of sintering (initial, intermediate and final) commonly categorised, are shown [146, 147]. In the initial stage of sintering, the interparticle contact starts to increase and it is typically related to neck formation and growth. It is accompanied by interparticle shrinkage of several percent (~3%) and a powder compact would experiment little increase in its relative density, from 50% to 60% of the theoretical density. The intermediate stage does not start until the neck formation is completed. The matrix is transformed into a body containing a continuous pore network but shrinks in volume. In this intermediate stage, the material experiment most of the densification from 60% to 85% of the theoretical density approximately. The final stage of sintering begins when the pores are isolated and cornered on the triple junctions from the original particles. The pores continue to shrink and eventually disappear completely or may reach equilibrium with the surrounding densified material preventing full densification. At this point densification is much slower than in the intermediate stage and normally a theoretical density greater than 90% is achieved. Grain growth has an important contribution in this stage as well.

In general terms, the sintering rate is directly proportional to time and the temperature of the sample, as more densification mechanisms are activated as the temperature increases. Additionally, it is inversely proportional to the particle size [148].

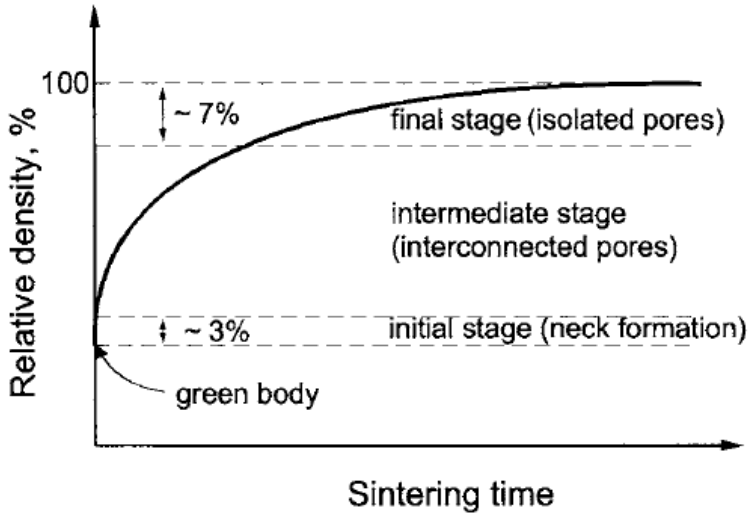

Figure 1. 15. Densification curve of a powder compact at the three sintering stages [148].

1.4.2. Sintering methods

Sintering and particularly conventional sintering has been part of human culture and development since Prehistory. Conventional sintering relies on long and high temperature treatments, which are time consuming and imply a high energy cost. Additionally, producing ceramics with the desired microstructure can be challenging as the required high temperature leads to significant grain growth and can deteriorate the stoichiometry of the material. Therefore, alternative methods of sintering, including flash sintering, have been developed to overcome these issues. As flash sintering is one of the main scopes of this thesis, Section 1.4.3 is devoted to describe its most important features.

Conventional sintering

A typical conventional sintering procedure consists in pressing powders of the starting materials with the required composition in a die, of proper shape, using uniaxial or cold-isostatic pressing. Binders, dispersants and sintering aids can be also incorporated to the powders prior to pressing. The resulting compacted body is known as green body. Then, it is fired up in a furnace for a certain period of time, employing suitable heating programs, which include dwell cycles. Thus, as it was mentioned above, conventional sintering relies just on temperature and time, which may vary significantly depending on the material, initial grain size, green body density and requirements of the final product.

Pressure assisted sintering

As it was mentioned in Section 1.4.1, an externally applied pressure is one of the driving forces in sintering. Thus, it can enhance significantly the densification rate at the expenses of grains coarsening. Dense ceramics with fine grains size can be achieved by these techniques. There are three techniques involving the use of an externally applied pressure: hot pressing (HP), hot isostatic pressing (HIP) and sinter hot forging [149-151]. Within them, hot pressing is the most widely used. It consists in applying simultaneously pressure and heat to a sample in a die, in the form of powder or green body. Graphite dies are commonly used due to their low cost, ease of machinability, high thermal conductivity and resistance to high temperature (up to 2400 °C). The major drawbacks of hot pressing are that the shape of the samples is limited to those of the graphite dies, which can chemically react with the sample.

Microwave assisted sintering

Microwaves are electromagnetic waves with wavelengths ranging from 1 m to 1 mm, which correspond to frequencies between 0.3 and 300 GHz. In microwave sintering, heat is generated internally through the interaction of the microwaves with the atoms, ions and molecules of the material, which produces an inverse heating profile. The microwave heating process is more volumetric, allowing higher heating rates which generally result in significant energy savings and shorter processing times. However, microwave assisted sintering is limited to materials that are microwave susceptors and, additionally, there are some issues that make this sintering technique a challenging process, such as the achievement of uniform heating and constant temperature profiles in the samples. The absorption of electromagnetic energy raises the temperature of the entire sample, but heat loss from the surface causes the near-surface temperature to become lower than the internal temperature. These temperature gradients are enhanced in ceramics with poor thermal conductivity, where a complicated geometry of the specimen or the microwave frequency additionally contributes to the thermal inhomogeneity of the samples. Moreover, high heating rates can lead to localized heating, which can cause non-uniform properties and even cracking of the sample as well as thermal runaway [152].

Spark Plasma Sintering (SPS)

Spark plasma sintering (SPS) is a low voltage, direct current (DC) pulsed current activated, pressure-assisted sintering technique [153-155]. This technique is similar to hot pressing. However, besides the uniaxial mechanical pressure (maximal loads typically between 50 and 250 kN), an

electric field is applied through the conductive die and the sample, which considerably enhances the densification rate at the expense of grain size. Figure 1. 16 shows a scheme of a SPS equipment.

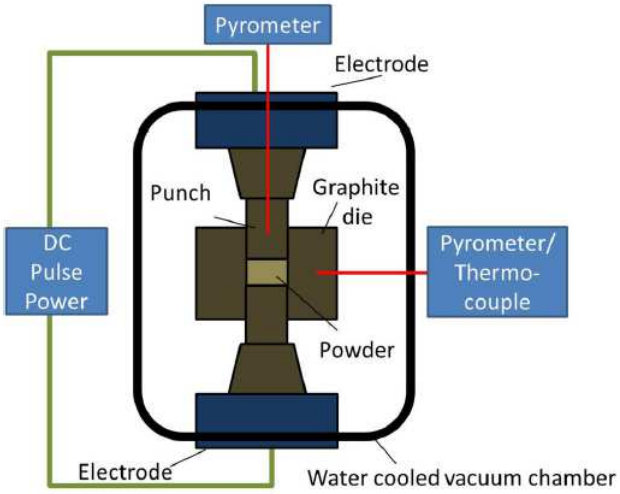

Figure 1. 16. SPS setup [155].

Due to the good electrical conductivity of graphite dies, it is possible the use of low voltages (typically below 10 V) that produce high currents (typically from 1 to 10 kA) leading to efficient joule heating of the samples (heating rates ~1000 °C min^{-1}). However, SPS presents some important drawbacks. For instance, the geometry of the specimens is limited to those of the graphite dies. The temperature of the samples, which is normally measured with an optical pyrometer focused on the graphite die walls, is difficult to determine. Another further complication is the determination of the contribution of the current to the overall sintering process as it passes through both the die and the sample. SPS setups are expensive and large. Moreover, pulse generators and an extremely careful control of working atmosphere are also required [156]. In principle, these limitations are overcome with the flash sintering technique.

1.4.3. Flash sintering

Flash sintering is a relatively new method of sintering developed by Cologna and Raj from the University of Colorado Boulder in 2010 [157]. It was first applied to 3 mol% yttria stabilized tetragonal zirconia (3YSZ), that under conventional conditions requires several hours at about 1400 ^{o}C for full densification. Under flash sintering conditions it was densified in just a few seconds by applying an electric field of 120 V cm^{-1} at a furnace temperature of 850 ^{o}C. Conversely to SPS, where part of the current unavoidably passes through the graphite die, in flash sintering the field is directly applied to the samples and any current must go through the specimen. Thus, relatively high electric fields and small currents are used in comparison to SPS [155, 158]. Figure 1. 17 shows the effect of the applied field on the sintering temperature of 3YSZ [157].

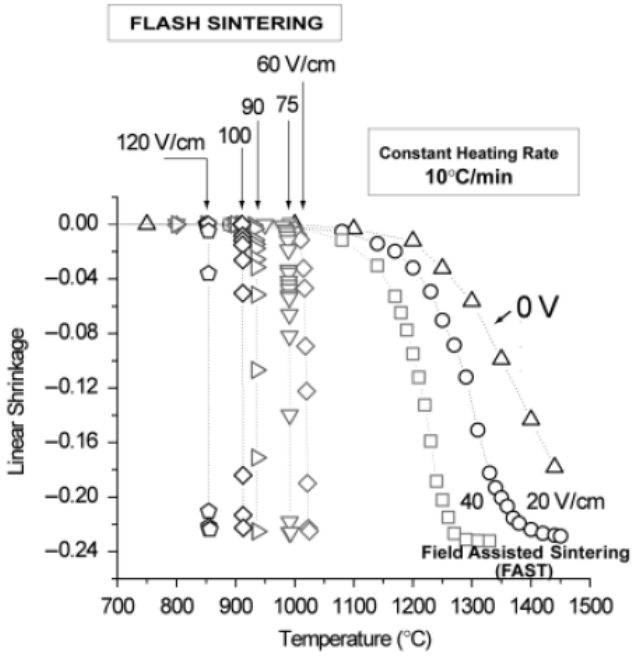

Figure 1. 17. Linear shrinkage versus sintering temperature under different applied electric fields for 3 mol% yttria stabilized zirconia (3YSZ) [157].

In Figure 1. 17, two regions can be clearly distinguished: at fields lower than 40 V cm^{-1}, densification occurs gradually, while at higher fields densification is obtained almost instantaneously. These two regions are known as field assisted sintering (FAST) and flash sintering (FS), respectively. In the flash sintering region, the onset of sintering temperature decreases with the applied electric field.

The interest of flash sintering within the scientific community is more than evident. In the last years, it has been shown that a small dc current produces sintering at low furnace temperatures in a number of materials: yttria [159], 8YSZ [160], Al_2O_3 [161], Co_2MnO_4 [162, 163], $SrTiO_3$ [164], $La_{0.6}Sr_{0.4}Co_{0.2}Fe_{0.8}O_3$ [165], TiO_2 [166], $Ca_5(PO_4)_3(OH)$ [167], $BaTiO_3$ [168], $CaCu_3Ti_4O_{12}$ [169], CeO_2 [170], ZnO [171], SiC [172, 173], $KNbO_3$ [174], Gd-$BaCeO_2$ [175], SnO_2 [176], SOFC [177]. Figure 1. 18 shows the onset of flash sintering in several ceramics in constant heating rate experiments. Interestingly, the flash event takes place in a small power density range, from 10 to 100 mW mm^{-3} [178].

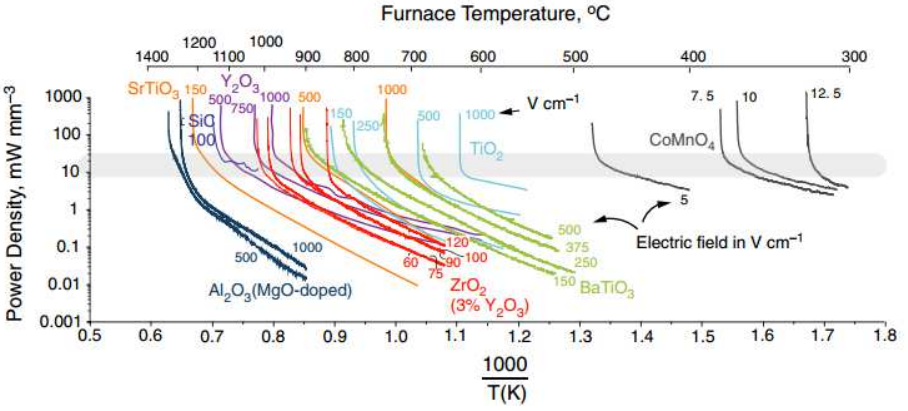

Figure 1. 18. The onset of flash in several ceramics in constant heating rate experiments [178].

Flash sintering stages

Flash sintering experiments can be carried out in two different ways: running the furnace at a constant heating rate under an applied electric field, where the flash is activated at a threshold temperature, or working the furnace under isothermal conditions and them apply the electric field. In this latter case, the flash is accompanied by an incubation time. For the sake of clarity, Figure 1. 19 shows the time dependence of the electric field, current, power dissipation and relative density under isothermal conditions for 3YSZ. Jha et al. summarized the events taking place in three stages of a flash experiment based on previous research with 3YSZ [179]:

- **Stage I**: in this region the power supply is under voltage controlled mode. The applied electric field is maintained constant, while the furnace temperature is either increasing or stable. The sample is mainly heated by joule heating.

- **Stage II**: after an incubation time (stage I), a non-linear rise of the current, due to a sharp increase in the conductivity of the sample, is produced. If the current is not limited, the sample would experiment very high joule heating and it would eventually melt. Thus, the power supply is switched from voltage to current controlled mode, in which the applied voltage, determined by the conductivity of the sample, is adjusted to maintain the current set point. As power dissipation is the product of voltage and current, a spike is observed in the power density when the power supply switches from voltage controlled to current controlled mode. Sintering occurs within 1–5 seconds. Beside the sharp increase in the conductivity of the

sample, electroluminescence and a dramatic increase of the densification rate are also observed in this region. Grain growth may be observed as well.

- **Stage III**: during this stage, power supply is still under current controlled mode. The flash state can be maintained within the sample. Grain growth occurs rapidly while electroluminescence is observed as well. The furnace can be turned off and the sample cooled during this stage.

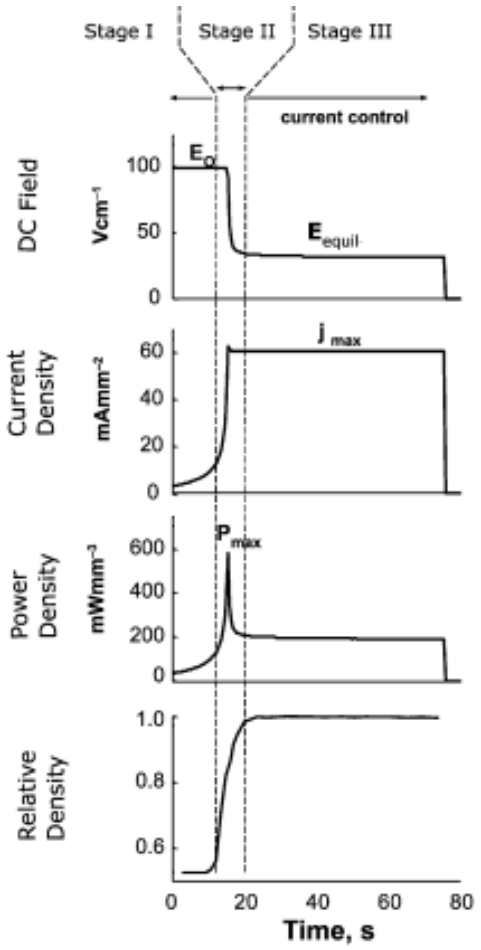

Figure 1. 19. Time dependence of electrical parameters in a flash experiment carried out at isothermal furnace temperature [179].

Mechanisms and experimental parameters

Although flash sintering mechanism is still under debate, in general terms, during flash sintering experiments there is a sharp increase in conductivity and electroluminiscence that, normally, but not necessarily, is accompanied by sintering. Joule heating, which consists in the increment of the specimen temperature from electrical energy dissipation, can be related to the dramatic increment in the densification rate [180]. Thus, much effort has been devoted to estimate the temperature of the specimen during the process, although it is particularly rough in stage II given its short duration. Good results have been obtained through the theory of black-body radiation, assuming that the effects of convention and conduction are negligible versus radiation. The temperature of the specimen can be estimated according to equation (1. 5) [180]:

$$\frac{\Delta T}{T_0} = \frac{W}{4\mathrm{A}\sigma T_0^4} \quad (1.\ 5)$$

Where ΔT is the increase in specimen temperature, W is the electrical power dissipated, A is the total surface area of the sample, σ is the Stefan Boltzmann constant ($5.67 \cdot 10^{-8}$ $Wm^2 K^{-4}$) and T_0 is the furnace temperature. Reasonable good agreement between measured temperatures by a pyrometer focused on the samples and the calculated temperatures through this theory was found, particularly in stage I, where the measured temperature was the same than that of the furnace, and in the steady part of stage III. However, no spike on the temperature measured by the pyrometer was detected [180]. The predicted temperatures obtained from the theory of the black body radiation have been further corroborated by synchrotron experiments for 3YSZ samples [181]. In those experiments, the temperature of the specimens could be indirectly calculated due to the

relationship between the thermal expansion and the lattice parameters, which were *in-situ* measured from the shift in the diffraction peaks while the flash sintering experiments were carried out. This method allows the detection of any difference in the anisotropic lattice expansion between materials sintered under conventional and flash sintering conditions. Nevertheless, the mechanism of flash sintering cannot be explained just by joule heating and recent studies have shown that the electric field has an effect that goes beyond the joule heating of the sample [180]. Another characteristic event during flash sintering is photoluminescence. It has been observed that the photoluminescence increases with the dissipated power or the electrical conductivity of the samples [181-183]. Particularly, Terauds et al. carried out an exhaustive analysis by measuring the optical spectrum of the emission during flash sintering experiment for 3YSZ and compared the results with the expected values if the emission arises from black body radiation [181]. It was found that peaks of a particular wavelength under flash conditions did not change with temperature, unlike for black body radiation, where peak shifts towards lower wavelengths, as temperature increases. This indicates that the source of optical emission cannot be just temperature [181].

Although the mechanisms of flash sintering remain unclear, it is generally well accepted the tendency of certain experimental parameters during flash sintering. It has been widely reported that flash sintering temperature decreases with the applied electric field [184, 185]. Additionally, in isothermal experiments, higher electric fields decrease the incubation time [186]. For a certain applied electric field, higher current densities lead to higher densifications [186]. Likewise conventional sintering, the initial particle size of the green body also influences the sintering kinetics. Hence, bigger particle size decreases the driving force

(curvature of the particle surface), leading to lower densification rates [187]. It has been reported that an externally applied pressure during flash (sinter-forging experiment), also contributes to higher densification rates at the expense of grains growth and it also declines the flash threshold temperature [184].

Although flash sintering is still in its initial stage of development and more research should be carried out in order to clarify certain aspects, particularly related to the mechanisms, the high interest in flash sintering is not surprising due to the advantages that it presents in comparison with other sintering methods. Besides the obvious energy saving and higher sintering rate, in contrast to conventional sintering, it enables a greater control over ceramic processing which may produce materials with tailored microstructures and novel properties. Additionally, the shape of the specimens is not limited to those of graphite dies, such as in hot pressing or SPS. Either vacuum or inert atmospheres are not essential requirements and relatively cheap experimental setups can be used in a laboratory scale. Thus, it is not surprising that industrial applications of flash sintering are being developed since 2012. It has been recently demonstrated that commercial floor tiles can be produced at furnace temperatures well below that used in conventional procedures and at higher production rate [188].

1.5. REFERENCES

[1] Glinchuk M.D., Ragulya A.V. and Stephanovich V.A., *Ferroics*, in *Nanoferroics*. **2013**, Springer Netherlands: Dordrecht. p. 1-32.

[2] Kao K.C., *4 - Ferroelectrics, Piezoelectrics, and Pyroelectrics*, in *Dielectric Phenomena in Solids*. **2004**, Academic Press: San Diego. p. 213-282.

[3] Hill N.A., *Why are there so few magnetic ferroelectrics?*. Journal of Physical Chemistry B, **2000**, 104 (29), p. 6694-6709.

[4] Abrahams S.C., *Ferroelasticity*. Materials Research Bulletin, **1971**, 6 (10), p. 881-890.

[5] Schmid H., *Multi-ferroic magnetoelectrics*. Ferroelectrics, **1994**, 162 (1), p. 317-338.

[6] Nan C.-W., Bichurin M.I., Dong S., Viehland D. and Srinivasan G., *Multiferroic magnetoelectric composites: Historical perspective, status, and future directions*. Journal of Applied Physics, **2008**, 103 (3), p. 031101.

[7] Eerenstein W., Mathur N.D. and Scott J.F., *Multiferroic and magnetoelectric materials*. Nature, **2006**, 442 (7104), p. 759-765.

[8] Spaldin N.A. and Fiebig M., *The renaissance of magnetoelectric multiferroics*. Science, **2005**, 309 (5733), p. 391-392.

[9] Cheong S.-W. and Mostovoy M., *Multiferroics: a magnetic twist for ferroelectricity*. Nature Materials, **2007**, 6 (1), p. 13-20.

[10] Wang K.F., Liu J.M. and Ren Z.F., *Multiferroicity: the coupling between magnetic and polarization orders*. Advances in Physics, **2009**, 58 (4), p. 321-448.

[11] Ascher E., Rieder H., Schmid H. and Stossel H., *Some properties of ferromagnetoelectric nickel-iodine boracite* $Ni_3B_7O_{13}I$. Journal of Applied Physics, **1966**, 37 (3), p. 1404-1405.

[12] Smolenskii G.A., Isupov V.A. and Agranovskaya A.I., *A new group of ferroelectrics - (with layered structure)*. Soviet Physics-Solid State, **1959**, 1 (1), p. 149-150.

[13] Brixel W., Rivera J.P., Steiner A. and Schmid H., *Magnetic Field-Induced Magnetoelectric Effects, (ME)H, in the Perovskites Pb_2CoWO_6 and Pb_2FeTaO_6*. Ferroelectrics, **1988**, 79, p. 495-498.

[14] Drobyshe.La, Alshin B.I., Tomashpo.Yy and Venevtse.Yn, *Growing, structure, and magnetic properties of $Pb_{1/2}Mn_{1/2}Nb_{1/2}O_3$ Single Crystals*. Soviet Physics Crystallography, Ussr, **1970**, 14 (4), p. 634.

[15] Astrov D.N., Alshin B.I., Zorin R.V. and Drobyshe.La, *Spontaneous magnetoelectric effect*. Soviet Physics Jetp-Ussr, **1969**, 28 (6), p. 3.

[16] Fiebig M., *Revival of the magnetoelectric effect*. Journal of Physics D: Applied Physics, **2005**, 38 (8), p. 123-152.

[17] Filipev V.S., Smolyninov N.P., Fesenko E.G. and I.N. B., *Synthesis of $BiFeO_3$ and determination of the unit cell*. Soviet Physics Crystallography, Ussr, **1960**, 5 (6), p. 913-914.

[18] Zaslavskii A.I. and Tutov A.G., *The structure of a new antiferromagnetic, $BiFeO_3$*. Doklady Akademii Nauk Sssr, **1960**, 135 (4), p. 815-819.

[19] Fedulov S.A., *Determinaton of Curie Temperaure for $BiFeO_3$ ferroelectric*. Doklady Akademii Nauk Sssr, **1961**, 139 (6), p. 1345-1346.

[20] Kiselev S.V., Zhdanov G.S. and Ozerov R.P., *Detection of magnetic arrangement on $BiFeO_3$ ferroelectric by means of neutron diffraction study*. Doklady Akademii Nauk Sssr, **1962**, 145 (6), p. 1255-1258.

[21] Tomashpolskii I.J., Venevtse.In and Zhdanov G.S., *Electron diffraction study of $BiFeO_3$ crystals*. Doklady Akademii Nauk Sssr, **1963**, 153 (6), p. 1313-1313.

[22] Venevcev J.N., Roginskaya J.E., Ivanova V.V., Fedulov S.A. and Zdanov G.S., *Investigation of some solid solutions based on ferrroelectric-antiferromagnetic $BiFeO_3$*. Acta Crystallographica, **1963**, 16 (13), p. 188.

[23] Smolenskii G.A. and Bokov V.A., *Coexistence of magnetic+electric ordering in crystals*. Journal of Applied Physics, **1964**, 35 (3P2), p. 915-918.

[24] Smolenskii G.A., Agranovskaia A.I., Popov S.N. and Isupov V.A., *New ferroelectrics of complex composition .2. Pb_2Fe_3+NbO_6 and Pb_2YbNbO_6*. Soviet Physics-Technical Physics, **1958**, 3 (10), p. 1981-1982.

[25] Smolenskii G.A., Isupov V.A. and Agranovskaya A.I., *New Ferroelectrics of Complex Composition of the Type $A_2^{2+}(Bi_I^{3+}Bi_{II}^{5+})O^{-6}$*. Soviet Physics-Solid State, **1959**, 1 (1), p. 150-151.

[26] Wang J., Neaton J.B., Zheng H., Nagarajan V., Ogale S.B., Liu B., Viehland D., Vaithyanathan V., Schlom D.G., Waghmare U.V., Spaldin N.A., Rabe K.M., Wuttig M. and Ramesh R., *Epitaxial $BiFeO_3$ Multiferroic Thin Film Heterostructures*. Science, **2003**, 299 (5613), p. 1719-1722.

[27] Catalan G. and Scott J.F., *Physics and Applications of Bismuth Ferrite*. Advanced Materials, **2009**, 21 (24), p. 2463-2485.

[28] Goldschmidt V.M., *Die Gesetze der Krystallochemie*. Naturwissenschaften, **1926**, 14 (21), p. 477-485.

[29] Wang W.R., Xu D.P. and Su W.H., *Raman shift of $RMnO_3$ (R = La, Pr, Nd, Sm) manganites*. Chinese Physics Letters, **2005**, 22 (3), p. 705-707.

[30] Zhang X., Sui Y., Wang X., Wang Y. and Wang Z., *Effect of Eu substitution on the crystal structure and multiferroic properties of $BiFeO_3$*. Journal of Alloys and Compounds, **2010**, 507 (1), p. 157-161.

[31] Li J.B., Rao G.H., Xiao Y., Liang J.K., Luo J., Liu G.Y. and Chen J.R., *Structural evolution and physical properties of $Bi_{1-x}Gd_xFeO_3$ ceramics*. Acta Materialia, **2010**, 58 (10), p. 3701-3708.

[32] Moreau J.M., Michel C., Gerson R. and James W.J., *Ferroelectric $BiFeO_3$ X-ray and neutron diffraction study*. Journal of Physics and Chemistry of Solids, **1971**, 32 (6), p. 1315-1320.

[33] Kubel F. and Schmid H., *Structure of a ferroelectric and ferroelastic monodomain crystal of the perovskite $BiFeO_3$*. Acta Crystallographica Section B, **1990**, 46 (6), p. 698-702.

[34] Bucci J.D., Robertson B.K. and James W.J., *The precision determination of the lattice parameters and the coefficients of thermal expansion of $BiFeO_3$*. Journal of Applied Crystallography, **1972**, 5 (3), p. 187-191.

[35] Shvartsman V.V., Kleemann W., Haumont R. and Kreisel J., *Large bulk polarization and regular domain structure in ceramic $BiFeO_3$*. Applied Physics Letters, **2007**, 90 (17), p. 172115.

[36] Khomskii D., *Trend: Classifying multiferroics: Mechanisms and effects*. Physics, **2009**, 2 (20).

[37] Sosnowska I., Neumaier T.P. and Steichele E., *Spiral magnetic ordering in bismuth ferrite*. Journal of Physics C: Solid State Physics, **1982**, 15 (23), p. 4835.

[38] Lebeugle D., Colson D., Forget A., Viret M., Bataille A.M. and Gukasov A., *Electric-Field-Induced Spin Flop in $BiFeO_3$ Single Crystals at Room Temperature*. Physical Review Letters, **2008**, 100 (22), p. 227602.

[39] Selbach S.M., Tybell T., Einarsrud M.-A. and Grande T., *The Ferroic Phase Transitions of $BiFeO_3$*. Advanced Materials, **2008**, 20 (19), p. 3692-+.

[40] Palai R., Katiyar R.S., Schmid H., Tissot P., Clark S.J., Robertson J., Redfern S.A.T., Catalan G. and Scott J.F., *β phase and $\gamma-\beta$ metal-insulator transition in multiferroic $BiFeO_3$*. Physical Review B, **2008**, 77 (1), p. 014110.

[41] Polomska M., Kaczmarek W. and Pajak Z., *Electric and Magnetic properties of $(Bi_{1-x}La_x)FeO_3$ solid-solutions.* Physica Status Solidi a-Applications and Materials Science, **1974**, 23 (2), p. 567-574.

[42] Kornev I.A., Lisenkov S., Haumont R., Dkhil B. and Bellaiche L., *Finite-Temperature Properties of Multiferroic $BiFeO_3$*. Physical Review Letters, **2007**, 99 (22), p. 227602.

[43] Arnold D.C., Knight K.S., Morrison F.D. and Lightfoot P., *Ferroelectric-Paraelectric Transition in $BiFeO_3$: Crystal Structure of the Orthorhombic beta Phase*. Physical Review Letters, **2009**, 102 (2).

[44] Megaw H.D. and Darlington C.N.W., *Geometrical and structural relations in the rhombohedral perovskites*. Acta Crystallographica Section A, **1975**, 31 (2), p. 161-173.

[45] González-Vázquez O.E. and Íñiguez J., *Pressure-induced structural, electronic, and magnetic effects in $BiFeO_3$*. Physical Review B, **2009**, 79 (6), p. 064102.

[46] Lyubutin I.S., Gavriliuk A.G. and Struzhkin V.V., *High-spin-low-spin transition and the sequence of the phase transformations in the $BiFeO_3$ crystal at high pressures*. JETP Letters, **2008**, 88 (8), p. 524-530.

[47] Lu J., Qiao L.J., Fu P.Z. and Wu Y.C., *Phase equilibrium of Bi_2O_3–Fe_2O_3 pseudo-binary system and growth of $BiFeO_3$ single crystal*. Journal of Crystal Growth, **2011**, 318 (1), p. 936-941.

[48] Selbach S.M., Tybell T., Einarsrud M.-A. and Grande T., *Phase transitions, electrical conductivity and chemical stability of $BiFeO_3$ at high temperatures*. Journal of Solid State Chemistry, **2010**, 183 (5), p. 1205-1208.

[49] Maruyama K., Kondo M., Singh S.K. and Ishiwara H., *New ferroelectric material or embedded FRAM LSIs*. Fujitsu Scientific & Technical Journal, **2007**, 43 (4), p. 502-507.

[50] Bibes M. and Barthelemy A., *Multiferroics: Towards a magnetoelectric memory*. Nat Mater, **2008**, 7 (6), p. 425-426.

[51] Prevot A.B., Baiocchi C., Brussino M.C., Pramauro E., Savarino P., Augugliaro V., Marci G. and Palmisano L., *Photocatalytic degradation of Acid Blue 80 in aqueous solutions containing TiO_2 suspensions*. Environmental Science and Technology, **2001**, 35 (5), p. 971-976.

[52] Gao F., Chen X.Y., Yin K.B., Dong S., Ren Z.F., Yuan F., Yu T., Zou Z.G. and Liu J.M., *Visible-Light Photocatalytic Properties of Weak*

Magnetic $BiFeO_3$ Nanoparticles. Advanced Materials, **2007**, 19 (19), p. 2889-2892.

[53] Wang X., Lin Y., Ding X. and Jiang J., *Enhanced visible-light-response photocatalytic activity of bismuth ferrite nanoparticles*. Journal of Alloys and Compounds, **2011**, 509 (23), p. 6585-6588.

[54] Soltani T. and Entezari M.H., *Photolysis and photocatalysis of methylene blue by ferrite bismuth nanoparticles under sunlight irradiation*. Journal of Molecular Catalysis A: Chemical, **2013**, 377, p. 197-203.

[55] Chen X.Y., Yu T., Gao F., Zhang H.T., Liu L.F., Wang Y.M., Li Z.S., Zou Z.G. and Liu J.M., *Application of weak ferromagnetic $BiFeO_3$ films as the photoelectrode material under visible-light irradiation*. Applied Physics Letters, **2007**, 91 (2).

[56] Ji W., Yao K., Lim Y.-F., Liang Y.C. and Suwardi A., *Epitaxial ferroelectric $BiFeO_3$ thin films for unassisted photocatalytic water splitting*. Applied Physics Letters, **2013**, 103 (6).

[57] Choi T., Lee S., Choi Y.J., Kiryukhin V. and Cheong S.W., *Switchable Ferroelectric Diode and Photovoltaic Effect in $BiFeO_3$*. Science, **2009**, 324 (5923), p. 63-66.

[58] Ji W., Yao K. and Liang Y.C., *Bulk Photovoltaic Effect at Visible Wavelength in Epitaxial Ferroelectric $BiFeO_3$ Thin Films*. Advanced Materials, **2010**, 22 (15), p. 1763-+.

[59] Yang S.Y., Martin L.W., Byrnes S.J., Conry T.E., Basu S.R., Paran D., Reichertz L., Ihlefeld J., Adamo C., Melville A., Chu Y.H., Yang C.H., Musfeldt J.L., Schlom D.G., Ager J.W., III and Ramesh R., *Photovoltaic effects in $BiFeO_3$*. Applied Physics Letters, **2009**, 95 (6).

[60] Yi H.T., Choi T., Choi S.G., Oh Y.S. and Cheong S.W., *Mechanism of the Switchable Photovoltaic Effect in Ferroelectric $BiFeO_3$*. Advanced Materials, **2011**, 23 (30), p. 3403-+.

[61] Yang S.Y., Seidel J., Byrnes S.J., Shafer P., Yang C.H., Rossell M.D., Yu P., Chu Y.H., Scott J.F., Ager J.W., III, Martin L.W. and Ramesh R., *Above-bandgap voltages from ferroelectric photovoltaic devices*. Nature Nanotechnology, **2010**, 5 (2), p. 143-147.

[62] Ruehle S., Anderson A.Y., Barad H.-N., Kupfer B., Bouhadana Y., Rosh-Hodesh E. and Zaban A., *All-Oxide Photovoltaics*. Journal of Physical Chemistry Letters, **2012**, 3 (24), p. 3755-3764.

[63] Yu X.L., Wang Y., Hu Y.M., Cao C.B. and Chan H.L.W., *Gas-Sensing Properties of Perovskite $BiFeO_3$ Nanoparticles*. Journal of the American Ceramic Society, **2009**, 92 (12), p. 3105-3107.

[64] Dziubaniuk M., Bujakiewicz-Korońska R., Suchanicz J., Wyrwa J. and Rękas M., *Application of bismuth ferrite protonic conductor for ammonia gas detection*. Sensors and Actuators B: Chemical, **2013**, 188, p. 957-964.

[65] Das S., Rana S., Mursalin S.M., Rana P. and Sen A., *Sonochemically prepared nanosized $BiFeO_3$ as novel SO_2 sensor*. Sensors and Actuators B-Chemical, **2015**, 218, p. 122-127.

[66] Mushtaq S., Qiang X., Akash K., Franklin A., Sang Sub K. and Ping W., *O_2 sensing dynamics of $BiFeO_3$ nanofibers: effect of minor carrier compensation*. Nanotechnology, **2015**, 26 (17), p. 175501.

[67] Valant M., Axelsson A.-K. and Alford N., *Peculiarities of a Solid-State Synthesis of Multiferroic Polycrystalline $BiFeO_3$*. Chemistry of Materials, **2007**, 19 (22), p. 5431-5436.

[68] Carvalho T.T. and Tavares P.B., *Synthesis and thermodynamic stability of multiferroic $BiFeO_3$*. Materials Letters, **2008**, 62 (24), p. 3984-3986.

[69] Selbach S.M., Einarsrud M.-A. and Grande T., *On the Thermodynamic Stability of $BiFeO_3$*. Chemistry of Materials, **2009**, 21 (1), p. 169-173.

[70] Maître A., François M. and Gachon J.C., *Experimental study of the Bi_2O_3-Fe_2O_3 pseudo-binary system*. Journal of Phase Equilibria and Diffusion, **2004**, 25 (1), p. 59-67.

[71] Morozov M.I., Lomanova N.A. and Gusarov V.V., *Specific Features of $BiFeO_3$ Formation in a Mixture of Bismuth(III) and Iron(III) Oxides*. Russian Journal of General Chemistry, **2003**, 73 (11), p. 1676-1680.

[72] Hideo K., Nobukazu N. and Takuro I., *An X-Ray Study on Bi_2O_3 - Fe_2O_3 System*. Japanese Journal of Applied Physics, **1964**, 3 (8), p. 495.

[73] Speranskaya E.I., Skorikov V.M., Rode E.Y. and Terekhova V.A., *The phase diagram of the system bismuth oxide-ferric oxide*. Bulletin of the Academy of Sciences of the USSR, Division of chemical science, **1965**, 14 (5), p. 873-874.

[74] Zhang S.X., Wang L., Chen Y., Wang D.L., Yao Y.B. and Ma Y.W., *Observation of room temperature saturated ferroelectric polarization in Dy substituted $BiFeO_3$ ceramics*. Journal of Applied Physics, **2012**, 111 (7).

[75] Yuan G.L., Or S.W., Wang Y.P., Liu Z.G. and Liu J.M., *Preparation and multi-properties of insulated single-phase $BiFeO_3$ ceramics*. Solid State Communications, **2006**, 138 (2), p. 76-81.

[76] Wang Y.P., Zhou L., Zhang M.F., Chen X.Y., Liu J.-M. and Liu Z.G., *Room-temperature saturated ferroelectric polarization in $BiFeO_3$ ceramics synthesized by rapid liquid phase sintering*. Applied Physics Letters, **2004**, 84 (10), p. 1731-1733.

[77] Khodabakhsh M., Sen C., Khassaf H., Gulgun M.A. and Misirlioglu I.B., *Strong smearing and disappearance of phase transitions into polar phases due to inhomogeneous lattice strains induced by A-site doping in $Bi_{1-x}A_xFeO_3$ (A: La, Sm, Gd)*. Journal of Alloys and Compounds, **2014**, 604, p. 117-129.

[78] Kadomtseva A.M., Zvezdin A.K., Popov Y.F., Pyatakov A.P. and Vorob'ev G.P., *Space-time parity violation and magnetoelectric interactions in antiferromagnets*. JETP Letters, **2004**, 79 (11), p. 571-581.

[79] Mazumder R., Sujatha Devi P., Bhattacharya D., Choudhury P., Sen A. and Raja M., *Ferromagnetism in nanoscale $BiFeO_3$*. Applied Physics Letters, **2007**, 91 (6), p. 062510.

[80] Mazumder R., Ghosh S., Mondal P., Bhattacharya D., Dasgupta S., Das N., Sen A., Tyagi A.K., Sivakumar M., Takami T. and Ikuta H., *Particle size dependence of magnetization and phase transition near T_N in multiferroic $BiFeO_3$*. Journal of Applied Physics, **2006**, 100 (3).

[81] Jaiswal A., Das R., Vivekanand K., Abraham P.M., Adyanthaya S. and Poddar P., *Effect of Reduced Particle Size on the Magnetic Properties of Chemically Synthesized $BiFeO_3$ Nanocrystals*. Journal of Physical Chemistry C, **2010**, 114 (5), p. 2108-2115.

[82] Park T.-J., Papaefthymiou G.C., Viescas A.J., Moodenbaugh A.R. and Wong S.S., *Size-dependent magnetic properties of single-crystalline*

multiferroic $BiFeO_3$ nanoparticles. Nano Letters, **2007**, 7 (3), p. 766-772.

[83] Selbach S.M., Tybell T., Einarsrud M.-A. and Grande T., *Size-dependent properties of multiferroic $BiFeO_3$ nanoparticles*. Chemistry of Materials, **2007**, 19 (26), p. 6478-6484.

[84] Shetty S., Palkar V.R. and Pinto R., *Size effect study in magnetoelectric $BiFeO_3$ system*. Pramana-Journal of Physics, **2002**, 58 (5-6), p. 1027-1030.

[85] Masó N. and West A.R., *Electrical Properties of Ca-Doped $BiFeO_3$ Ceramics: From p-Type Semiconduction to Oxide-Ion Conduction*. Chemistry of Materials, **2012**, 24 (11), p. 2127-2132.

[86] Gu Y.H., Wang Y., Chen F., Chan H.L.W. and Chen W.P., *Nonstoichiometric $BiFe_{0.9}Ti_{0.05}O_3$ multiferroic ceramics with ultrahigh electrical resistivity*. Journal of Applied Physics, **2010**, 108 (9), p. 094112.

[87] Ahmmad B., Kanomata K., Koike K., Kubota S., Kato H., Hirose F., Billah A., Jalil M.A. and Basith M.A., *Large difference between the magnetic properties of Ba and Ti co-doped $BiFeO_3$ bulk materials and their corresponding nanoparticles prepared by ultrasonication*. Journal of Physics D-Applied Physics, **2016**, 49 (26).

[88] Biswal M.R., Nanda J., Mishra N.C. and Anwar S., *Electrical and Magnetoelectric Properties of Ni-Co Doped $BiFeO_3$ Ceramics*. Advanced Science Letters, **2016**, 22 (2), p. 363-366.

[89] Woodward D.I., Reaney I.M., Eitel R.E. and Randall C.A., *Crystal and domain structure of the $BiFeO_3$-$PbTiO_3$ solid solution*. Journal of Applied Physics, **2003**, 94 (5), p. 3313-3318.

[90] Khomchenko V.A., Kiselev D.A., Vieira J.M., Jian L., Kholkin A.L., Lopes A.M.L., Pogorelov Y.G., Araujo J.P. and Maglione M., *Effect of diamagnetic Ca, Sr, Pb, and Ba substitution on the crystal structure and multiferroic properties of the $BiFeO_3$ perovskite*. Journal of Applied Physics, **2008**, 103 (2).

[91] Arnold D.C., *Composition-Driven Structural Phase Transitions in Rare-Earth-Doped $BiFeO_3$ Ceramics: A Review*. Ieee Transactions on Ultrasonics Ferroelectrics and Frequency Control, **2015**, 62 (1), p. 62-82.

[92] Bielecki J., Svedlindh P., Tibebu D.T., Cai S., Eriksson S.-G., Börjesson L. and Knee C.S., *Structural and magnetic properties of isovalently substituted multiferroic $BiFeO_3$: Insights from Raman spectroscopy*. Physical Review B, **2012**, 86 (18), p. 184422.

[93] Khomchenko V.A., Troyanchuk I.O., Bushinsky M.V., Mantytskaya O.S., Sikolenko V. and Paixão J.A., *Structural phase evolution in $Bi_{7/8}Ln_{1/8}FeO_3$ (Ln = La–Dy) series*. Materials Letters, **2011**, 65 (12), p. 1970-1972.

[94] Karimi S., Reaney I.M., Han Y., Pokorny J. and Sterianou I., *Crystal chemistry and domain structure of rare-earth doped $BiFeO_3$ ceramics*. Journal of Materials Science, **2009**, 44 (19), p. 5102-5112.

[95] Bernardo M.S., Jardiel T., Peiteado M., Caballero A.C. and Villegas M., *Reaction pathways in the solid state synthesis of multiferroic $BiFeO_3$*. Journal of the European Ceramic Society, **2011**, 31 (16), p. 3047-3053.

[96] Mukherjee J.L. and Wang F.F.Y., *Kinetics of solid-state reaction of Bi_2O_3 and Fe_2O_3*. Journal of the American Ceramic Society, **1971**, 54 (1), p. 31-34.

[97] Pradhan A.K., Zhang K., Hunter D., Dadson J.B., Loiutts G.B., Bhattacharya P., Katiyar R., Zhang J., Sellmyer D.J., Roy U.N., Cui Y. and Burger A., *Magnetic and electrical properties of single-phase multiferroic $BiFeO_3$*. Journal of Applied Physics, **2005**, 97 (9), p. 093903.

[98] Singh H. and Yadav K.L., *Structural, dielectric, vibrational and magnetic properties of Sm doped $BiFeO_3$ multiferroic ceramics prepared by a rapid liquid phase sintering method*. Ceramics International, **2015**, 41 (8), p. 9285-9295.

[99] Wei J. and Xue D., *Low-temperature synthesis of $BiFeO_3$ nanoparticles by ethylenediaminetetraacetic acid complexing sol–gel process*. Materials Research Bulletin, **2008**, 43 (12), p. 3368-3373.

[100] Hasan M., Islam M.F., Mahbub R., Hossain M.S. and Hakim M.A., *A soft chemical route to the synthesis of $BiFeO_3$ nanoparticles with enhanced magnetization*. Materials Research Bulletin, **2016**, 73, p. 179-186.

[101] Selbach S.M., Einarsrud M.-A., Tybell T. and Grande T., *Synthesis of $BiFeO_3$ by wet chemical methods*. Journal of the American Ceramic Society, **2007**, 90 (11), p. 3430-3434.

[102] Masoudpanah S.M., Mirkazemi S.M., Shabani S. and Dolat Abadi P.T., *The effect of the ethylene glycol to metal nitrate molar ratio on the phase evolution, morphology and magnetic properties of single phase $BiFeO_3$ nanoparticles*. Ceramics International, **2015**, 41 (8), p. 9642-9646.

[103] Kumar M., Yadav K.L. and Varma G.D., *Large magnetization and weak polarization in sol–gel derived $BiFeO_3$ ceramics*. Materials Letters, **2008**, 62 (8–9), p. 1159-1161.

[104] Mukherjee A., Basu S., Chakraborty G. and Pal M., *Effect of Y-doping on the electrical transport properties of nanocrystalline $BiFeO_3$*. Journal of Applied Physics, **2012**, 112 (1).

[105] Schiemer J., Withers R.L., Carpenter M.A., Liu Y., Wang J.L., Norén L., Li Q. and Hutchison W., *Temperature-dependent electrical, elastic and magnetic properties of sol–gel synthesized $Bi_{0.9}Ln_{0.1}FeO_3$ (Ln = Nd, Sm)*. Journal of Physics: Condensed Matter, **2012**, 24 (12), p. 125901.

[106] Vijayanand S., Potdar H.S. and Joy P.A., *Origin of high room temperature ferromagnetic moment of nanocrystalline multiferroic $BiFeO_3$*. Applied Physics Letters, **2009**, 94 (18), p. 182507.

[107] Paraschiv C., Jurca B., Ianculescu A. and Carp O., *Synthesis of nanosized bismuth ferrite ($BiFeO_3$) by a combustion method starting from $Fe(NO_3)_3 \cdot 9H_2O$-$Bi(NO_3)_3 \cdot 9H_2O$-glycine or urea systems*. Journal of Thermal Analysis and Calorimetry, **2008**, 94 (2), p. 411-416.

[108] Iorgu A.I., Maxim F., Matei C., Ferreira L.P., Ferreira P., Cruz M.M. and Berger D., *Fast synthesis of rare-earth (Pr^{3+}, Sm^{3+}, Eu^{3+} and Gd^{3+}) doped bismuth ferrite powders with enhanced magnetic properties*. Journal of Alloys and Compounds, **2015**, 629, p. 62-68.

[109] Ke H., Wang W., Wang Y., Xu J., Jia D., Lu Z. and Zhou Y., *Factors controlling pure-phase multiferroic $BiFeO_3$ powders synthesized by chemical co-precipitation*. Journal of Alloys and Compounds, **2011**, 509 (5), p. 2192-2197.

[110] Kothai V. and Ranjan R., *Synthesis of $BiFeO_3$ by carbonate precipitation*. Bulletin of Materials Science, **2012**, 35 (2), p. 157-161.

[111] Hu Z.-T., Lua S.K., Yan X. and Lim T.-T., *Nanostructured hexahedron of bismuth ferrite clusters: delicate synthesis processes and an efficient multiplex catalyst for organic pollutant degradation*. RSC Advances, **2015**, 5 (106), p. 86891-86900.

[112] Liu Z., Qi Y. and Lu C., *High efficient ultraviolet photocatalytic activity of $BiFeO_3$ nanoparticles synthesized by a chemical coprecipitation process*. Journal of Materials Science: Materials in Electronics, **2010**, 21 (4), p. 380-384.

[113] Shami M.Y., Awan M.S. and Anis-ur-Rehman M., *Phase pure synthesis of $BiFeO_3$ nanopowders using diverse precursor via co-precipitation method*. Journal of Alloys and Compounds, **2011**, 509 (41), p. 10139-10144.

[114] Medina L.M.S., Jorge G.A. and Martín Negri R., *Structural, dielectric and magnetic properties of $Bi_{1-x}Y_xFeO3$ ($0 < x < 0.2$) obtained by acid–base co-precipitation*. Journal of Alloys and Compounds, **2014**, 592, p. 306-312.

[115] Yoshimura M. and Byrappa K., *Hydrothermal processing of materials: past, present and future*. Journal of Materials Science, **2008**, 43 (7), p. 2085-2103.

[116] Han J.T., Huang Y.H., Wu X.J., Wu C.L., Wei W., Peng B., Huang W. and Goodenough J.B., *Tunable Synthesis of Bismuth Ferrites with Various Morphologies*. Advanced Materials, **2006**, 18 (16), p. 2145-2148.

[117] Reddy Vanga P., Mangalaraja R.V., Giridharan N.V. and Ashok M., *PTCR behavior of $BiFeO_3$ synthesized by the solvothermal method*. Materials Letters, **2015**, 143, p. 230-232.

[118] Chen C., Cheng J., Yu S., Che L. and Meng Z., *Hydrothermal synthesis of perovskite bismuth ferrite crystallites*. Journal of Crystal Growth, **2006**, 291 (1), p. 135-139.

[119] Han S.H., Kim K.S., Kim H.G., Lee H.-G., Kang H.-W., Kim J.S. and Cheon C.I., *Synthesis and characterization of multiferroic $BiFeO_3$ powders fabricated by hydrothermal method*. Ceramics International, **2010**, 36 (4), p. 1365-1372.

[120] Wu C.F., Wei J. and Kong F.S., *Effect of rare earth dopants on the morphologies and photocatalytic activities of $BiFeO_3$ microcrystallites*. Journal of Materials Science-Materials in Electronics, **2013**, 24 (5), p. 1530-1535.

[121] Gajović A., Šturm S., Jančar B., Šantić A., Žagar K. and Čeh M., *The Synthesis of Pure-Phase Bismuth Ferrite in the Bi–Fe–O System Under Hydrothermal Conditions without a Mineralizer*. Journal of the American Ceramic Society, **2010**, 93 (10), p. 3173-3179.

[122] Chen X.-Z., Qiu Z.-C., Zhou J.-P., Zhu G., Bian X.-B. and Liu P., *Large-scale growth and shape evolution of bismuth ferrite particles with a hydrothermal method*. Materials Chemistry and Physics, **2011**, 126 (3), p. 560-567.

[123] Prado-Gonjal J., Villafuerte-Castrejón M.E., Fuentes L. and Morán E., *Microwave–hydrothermal synthesis of the multiferroic $BiFeO_3$*. Materials Research Bulletin, **2009**, 44 (8), p. 1734-1737.

[124] Li S., Nechache R., Davalos I.A.V., Goupil G., Nikolova L., Nicklaus M., Laverdiere J., Ruediger A. and Rosei F., *Ultrafast Microwave Hydrothermal Synthesis of $BiFeO_3$ Nanoplates*. Journal of the American Ceramic Society, **2013**, 96 (10), p. 3155-3162.

[125] Dutta D.P., Jayakumar O.D., Tyagi A.K., Girija K.G., Pillai C.G.S. and Sharma G., *Effect of doping on the morphology and multiferroic properties of $BiFeO_3$ nanorods*. Nanoscale, **2010**, 2 (7), p. 1149-1154.

[126] Szafraniak I., Połomska M., Hilczer B., Pietraszko A. and Kępiński L., *Characterization of $BiFeO_3$ nanopowder obtained by mechanochemical synthesis*. Journal of the European Ceramic Society, **2007**, 27 (13–15), p. 4399-4402.

[127] Da Silva K.L., Menzel D., Feldhoff A., Kübel C., Bruns M., Paesano A., Düvel A., Wilkening M., Ghafari M., Hahn H., Litterst F.J., Heitjans P., Becker K.D. and Šepelák V., *Mechanosynthesized $BiFeO_3$ Nanoparticles with Highly Reactive Surface and Enhanced Magnetization*. The Journal of Physical Chemistry C, **2011**, 115 (15), p. 7209-7217.

[128] Perejon A., Murafa N., Sanchez-Jimenez P.E., Criado J.M., Subrt J., Dianez M.J. and Perez-Maqueda L.A., *Direct mechanosynthesis of pure $BiFeO_3$ perovskite nanoparticles: reaction mechanism*. Journal of Materials Chemistry C, **2013**, 1 (22), p. 3551-3562.

[129] Perejon A., Sanchez-Jimenez P.E., Perez-Maqueda L.A., Criado J.M., Romero de Paz J., Saez-Puche R., Maso N. and West A.R., *Single phase, electrically insulating, multiferroic La-substituted $BiFeO_3$ prepared by mechanosynthesis*. Journal of Materials Chemistry C, **2014**, 2 (39), p. 8398-8411.

[130] Perejon A., Gil-Gonzalez E., Sanchez-Jimenez P.E., Criado J.M. and Perez-Maqueda L.A., *Structural, Optical, and Electrical Characterization of Yttrium-Substituted $BiFeO_3$ Ceramics Prepared by Mechanical Activation*. Inorganic Chemistry, **2015**, 54 (20), p. 9876-9884.

[131] Pattanayak S., Parida B.N., Das P.R. and Choudhary R.N.P., *Impedance spectroscopy of Gd-doped $BiFeO_3$ multiferroics*. Applied Physics A, **2013**, 112 (2), p. 387-395.

[132] Layek S. and Verma H., *Magnetic and dielectric properties of multiferroic $BiFeO_3$ nanoparticles synthesized by a novel citrate combustion method*. Advanced Materials Letters, **2012**, 3 (6), p. 6.

[133] Heinicke G., *Tribochemistry*. **1984**, Berlin: Akademie Verlag.

[134] James M. *Grinding Chemicals Together in an Effort to be Greener*. http://www.nytimes.com/2016/07/19/science/green-chemistry-mechanochemistry.html?_r=0 **2016**.

[135] Balaz P., Achimovicova M., Balaz M., Billik P., Cherkezova-Zheleva Z., Criado J.M., Delogu F., Dutkova E., Gaffet E., Gotor F.J., Kumar R., Mitov I., Rojac T., Senna M., Streletskii A. and Wieczorek-Ciurowa K., *Hallmarks of mechanochemistry: from nanoparticles to technology*. Chemical Society Reviews, **2013**, 42 (18), p. 7571-7637.

[136] Boldyrev V.V., *Mechanochemistry and mechanical activation of solids*. Solid State Ionics, **1993**, 63, p. 537-543.

[137] Suryanarayana C., *Mechanical Alloying and Milling*, ed. Dekker Marcel. **2004**, New York.

[138] Humphry-Baker S.A., Garroni S., Delogu F. and Schuh C.A., *Melt-driven mechanochemical phase transformations in moderately exothermic powder mixtures*. Nature Materials, **2016**, 15 (12), p. 1280-1286.

[139] Urakaev F.K., Boldyrev V.V., Pozdnyakov O.F. and Regel V.R., *Study of mechanism of mechanochemical decomposition of solid inorganic-compounds*. Kinetics and Catalysis, **1977**, 18 (2), p. 292-299.

[140] Larsen H.A. and Drickamer H.G., *Chemical Effects of Plastic Deformation at High Pressure*. The Journal of Physical Chemistry, **1957**, 61 (9), p. 1249-1252.

[141] Bokhonov B., Konstanchuk I., Ivanov E. and Boldyrev V., *Stage formation of quasi-crystals during mechanical treatment of the cubic Frank-Kaspes phase* $Mg_{32}(Zn, Al)_{49}$. Journal of Alloys and Compounds, **1992**, 187 (1), p. 207-214.

[142] Thiessen P.A., Meyer K. and Heinicke G., *Grundlagen der Tribochemie*. **1967**, Berlin: Akademie Verlag.

[143] Castro R. and van Bentherm K., eds. *Sintering: Mechanisms of Convention Nanodensification and Field Assisted Processes*. Vol. 35. **2013**, Springer: Heidelberg, New York, Dordrecht, London.

[144] Kang S.-J.L., *Sintering process*, in *Sintering: densification, grain growth and microstructure*. **2005**, Butterworth-Heinemann: Oxford. p. 3-8.

[145] Swinkels F.B. and Ashby M.F., *A second report on sintering diagrams*. Acta Metallurgica, **1981**, 29 (2), p. 259-281.

[146] Coble R.L., *Sintering Crystalline Solids. I. Intermediate and Final State Diffusion Models*. Journal of Applied Physics, **1961**, 32 (5), p. 787-792.

[147] Coble R.L., *Sintering Crystalline Solids. II. Experimental Test of Diffusion Models in Powder Compacts*. Journal of Applied Physics, **1961**, 32 (5), p. 793-799.

[148] Kang S.-J.L., *4 Initial stage sintering*, in *Sintering: Densification, Grain Growth, and Microstructure*. **2005**, Butterworth-Heinemann: Oxford. p. 39-55.

[149] Kingery W.D., Uhlmann D.R. and Bowen H.K., eds. *Introduction to ceramic*. 2nd ed. **1976**, John Wiley & Sons: New York

[150] Venkatachari K.R. and Raj R., *Enhancement of Strength through Sinter Forging*. Journal of the American Ceramic Society, **1987**, 70 (7), p. 514-520.

[151] Rahaman M.N. and De Jonghe L.C., *Sintering of CdO Under Low Applied Stress*. Journal of the American Ceramic Society, **1984**, 67 (10), p. 205-207.

[152] Lakshmanan A., ed. *Sintering of Ceramics – New Emerging Techniques*. **2012**, InTech: Rijeka.

[153] Munir Z.A., Anselmi-Tamburini U. and Ohyanagi M., *The effect of electric field and pressure on the synthesis and consolidation of materials: A review of the spark plasma sintering method*. Journal of Materials Science, **2006**, 41 (3), p. 763-777.

[154] Garay J.E., *Current-Activated, Pressure-Assisted Densification of Materials*. Annual Review of Materials Research, **2010**, 40, p. 445-468.

[155] Guillon O., Gonzalez-Julian J., Dargatz B., Kessel T., Schierning G., Raethel J. and Herrmann M., *Field-Assisted Sintering Technology/Spark Plasma Sintering: Mechanisms, Materials, and*

Technology Developments. Advanced Engineering Materials, **2014**, 16 (7), p. 830-849.

[156] Tokita M., *Industrial applications of advanced spark plasma sintering*. American Ceramic Society Bulletin, **2006**, 85 (2), p. 32-34.

[157] Cologna M., Rashkova B. and Raj R., *Flash Sintering of Nanograin Zirconia in < 5 s at 850 °C*. Journal of the American Ceramic Society, **2010**, 93 (11), p. 3556-3559.

[158] Dancer C.E.J., *Flash sintering of ceramic materials*. Materials Research Express, **2016**, 3 (10).

[159] Yoshida H., Sakka Y., Yamamoto T., Lebrun J.-M. and Raj R., *Densification behaviour and microstructural development in undoped yttria prepared by flash-sintering*. Journal of the European Ceramic Society, **2014**, 34 (4), p. 991-1000.

[160] Cologna M., Prette A.L.G. and Raj R., *Flash-Sintering of Cubic Yttria-Stabilized Zirconia at 750 °C for Possible Use in SOFC Manufacturing*. Journal of the American Ceramic Society, **2011**, 94 (2), p. 316-319.

[161] Cologna M., Francis J.S.C. and Raj R., *Field assisted and flash sintering of alumina and its relationship to conductivity and MgO-doping*. Journal of the European Ceramic Society, **2011**, 31 (15), p. 2827-2837.

[162] Prette A.L.G., Cologna M., Sglavo V. and Raj R., *Flash-sintering of Co_2MnO_4 spinet for solid oxide fuel cell applications*. Journal of Power Sources, **2011**, 196 (4), p. 2061-2065.

[163] Gaur A. and Sglavo V.M., *Flash-sintering of $MnCo_2O_4$ and its relation to phase stability*. Journal of the European Ceramic Society, **2014**, 34 (10), p. 2391-2400.

[164] Karakuscu A., Cologna M., Yarotski D., Won J., Francis J.S.C., Raj R. and Uberuaga B.P., *Defect Structure of Flash-Sintered Strontium Titanate*. Journal of the American Ceramic Society, **2012**, 95 (8), p. 2531-2536.

[165] Gaur A. and Sglavo V.M., *Densification of $La_{0.6}Sr_{0.4}Co_{0.2}Fe_{0.8}O_3$ ceramic by flash sintering at temperature less than 100 °C*. Journal of Materials Science, **2014**, 49 (18), p. 6321-6332.

[166] Jha S.K. and Raj R., *The Effect of Electric Field on Sintering and Electrical Conductivity of Titania*. Journal of the American Ceramic Society, **2014**, 97 (2), p. 527-534.

[167] Bajpai I., Han Y.-H., Yun J., Francis J., Kim S. and Raj R., *Preliminary investigation of hydroxyapatite microstructures prepared by flash sintering*. Advances in Applied Ceramics, **2016**, 115 (5), p. 276-281.

[168] M'Peko J.-C., Francis J.S.C. and Raj R., *Field-assisted sintering of undoped $BaTiO_3$: Microstructure evolution and dielectric permittivity*. Journal of the European Ceramic Society, **2014**, 34 (15), p. 3655-3660.

[169] Jesus L.M., Silva R.S., Raj R. and M'Peko J.-C., *Electric field-assisted flash sintering of $CaCu_3Ti_4O_{12}$: Microstructure characteristics and dielectric properties*. Journal of Alloys and Compounds, **2016**, 682, p. 753-758.

[170] Gaur A. and Sglavo V.M., *Flash Sintering of (La, Sr)(Co, Fe)O_3-Gd-Doped CeO_2 Composite*. Journal of the American Ceramic Society, **2015**, 98 (6), p. 1747-1752.

[171] Zhang Y. and Luo J., *Promoting the flash sintering of ZnO in reduced atmospheres to achieve nearly full densities at furnace temperatures of <120°C*. Scripta Materialia, **2015**, 106, p. 26-29.

[172] Zapata-Solvas E., Bonilla S., Wilshaw P.R. and Todd R.I., *Preliminary investigation of flash sintering of SiC*. Journal of the European Ceramic Society, **2013**, 33 (13-14), p. 2811-2816.

[173] Candelario V.M., Moreno R., Todd R.I. and Ortiz A.L., *Liquid-phase assisted flash sintering of SiC from powder mixtures prepared by aqueous colloidal processing*. Journal of the European Ceramic Society, **2017**, 37 (2), p. 485-498.

[174] Shomrat N., Baltianski S., Randall C.A. and Tsur Y., *Flash sintering of potassium-niobate*. Journal of the European Ceramic Society, **2015**, 35 (7), p. 2209-2213.

[175] Muccillo R., Muccillo E.N.S. and Kleitz M., *Densification and enhancement of the grain boundary conductivity of gadolinium-doped barium cerate by ultra fast flash grain welding*. Journal of the European Ceramic Society, **2012**, 32 (10), p. 2311-2316.

[176] Muccillo R. and Muccillo E.N.S., *Electric field-assisted flash sintering of tin dioxide*. Journal of the European Ceramic Society, **2014**, 34 (4), p. 915-923.

[177] Francis J.S.C., Cologna M., Montinaro D. and Raj R., *Flash Sintering of Anode-Electrolyte Multilayers for SOFC Applications*. Journal of the American Ceramic Society, **2013**, 96 (5), p. 1352-1354.

[178] Raj R., *Analysis of the Power Density at the Onset of Flash Sintering*. Journal of the American Ceramic Society, **2016**, 99 (10), p. 3226-3232.

[179] Jha S.K., Terauds K., Lebrun J.-M. and Raj R., *Beyond flash sintering in 3 mol % yttria stabilized zirconia*. Journal of the Ceramic Society of Japan, **2016**, 124 (4), p. 283-288.

[180] Raj R., *Joule heating during flash-sintering*. Journal of the European Ceramic Society, **2012**, 32 (10), p. 2293-2301.

[181] Terauds K., Lebrun J.-M., Lee H.-H., Jeon T.-Y., Lee S.-H., Je J.H. and Raj R., *Electroluminescence and the measurement of temperature during Stage III of flash sintering experiments*. Journal of the European Ceramic Society, **2015**, 35 (11), p. 3195-3199.

[182] Lebrun J.-M. and Raj R., *A First Report of Photoemission in Experiments Related to Flash Sintering*. Journal of the American Ceramic Society, **2014**, 97 (8), p. 2427-2430.

[183] Naik K., Jha S.K. and Raj R., *Correlations between conductivity, electroluminescence and flash sintering*. Scripta Materialia, **2016**, 118, p. 1-4.

[184] Francis J.S.C. and Raj R., *Flash-Sinterforging of Nanograin Zirconia: Field Assisted Sintering and Superplasticity*. Journal of the American Ceramic Society, **2012**, 95 (1), p. 138-146.

[185] Biesuz M. and Sglavo V.M., *Flash sintering of alumina: Effect of different operating conditions on densification*. Journal of the European Ceramic Society, **2016**, 36 (10), p. 2535-2542.

[186] Francis J.S.C. and Raj R., *Influence of the Field and the Current Limit on Flash Sintering at Isothermal Furnace Temperatures*. Journal of the American Ceramic Society, **2013**, 96 (9), p. 2754-2758.

[187] Francis J.S.C., Cologna M. and Raj R., *Particle size effects in flash sintering*. Journal of the European Ceramic Society, **2012**, 32 (12), p. 3129-3136.

[188] Yu M., Grasso S., McKinnon R., Saunders T. and Reece M.J., *Review of flash sintering: materials, mechanisms and modelling*. Advances in Applied Ceramics, **2017**, 116 (1), p. 24-60.

2. OBJECTIVES AND OUTLINE

2.1. OBJECTIVES

As stated in Chapter 1, $BiFeO_3$ is one of the most studied and promising magnetoelectric materials due to its multiferroic behaviour at room temperature. This makes of $BiFeO_3$ an interesting and versatile material to be used in many different practical applications. However, there are several issues that are slowing down its implementation in devices, such as its poor magnetoelectric coupling and its difficult preparation. Particularly, its synthesis by conventional solid-state reaction is extremely tricky, normally yielding impurities and secondary phases that produce a notorious deterioration of its physical properties. Hence, looking for alternative procedures for the preparation and sintering of $BiFeO_3$, as well as exploring approaches in order to enhance its physical properties, such as the partial substitution of Bi^{3+} for rare-earth isovalent cations (RE^{3+}), are of the most interest.

The initial scope of this thesis is to employ mechanochemistry for the preparation of rare-earth partially-substituted $BiFeO_3$ systems ($Bi_{1-x}RE_xFeO_3$), as well as to explore flash sintering as an alternative method to obtain highly dense and pure $BiFeO_3$ specimens. Specifically, the main objectives of this thesis are:

- Preparation of the ytterbium partially-substituted $BiFeO_3$ system ($Bi_{1-x}Yb_xFeO_3$) by direct mechanochemistry as well as its characterization in terms of the crystal structure, temperature

dependent behaviour, microstructure and the study of its optical, electrical and magnetic properties.

- Synthesis by direct mechanochemistry of the samarium partially-substituted $BiFeO_3$ system ($Bi_{1-x}Sm_xFeO_3$) in a wide range of composition and its characterization by an exhaustive analysis of their crystal structure, microstructure, temperature dependant behaviour and the evaluation of their optical, electrical and magnetic properties.

- Employment of the novel flash sintering approach for the densification of mechanosynthesized $BiFeO_3$ powders as well as the evaluation of the effects of the experimental parameters on the purity, microstructure and electrical properties of the densified specimens.

- Inspired by the flash sintering procedure, exploring an alternative synthetic method based on the electric field-assisted solid-state reaction of the pristine oxides, Fe_2O_3 and Bi_2O_3, to prepare $BiFeO_3$. Additionally, the optimization of the synthesis conditions and the study of the reaction mechanism.

- Finally, the study of the thermal crystallization event in nanocrystalline $BiFeO_3$ powders by the combination of the information obtained from different characterization techniques. The crystallization is one key aspect in the resulting properties of functional materials, but to the best of our knowledge, studies of the thermal crystallization kinetics in $BiFeO_3$ are scarce and

none of them have properly addressed its study by a combination of several characterization techniques.

2.2. OUTLINE

This thesis is structured in 9 chapters, where the most relevant results are presented in chapters, 4, 5, 6, 7 and 8. These chapters include a brief introduction and specific conclusions to the topic addressed. The outline of this thesis is described as follows:

- Chapter 1 includes a literature review, which aim is to provide a general overview about $BiFeO_3$ and related materials, mechanochemistry and flash sintering.

- Chapter 2 addresses the motivation, objectives and outline of this thesis.

- Chapter 3 describes the materials, experimental setups and characterization techniques employed in this research.

- Chapter 4 is devoted to the preparation by direct mechanosynthesis of the $Bi_{1-x}Yb_xFeO_3$ system. This chapter also includes the characterization carried out to the mechanosynthesised system in terms of the crystal structure, microstructure, temperature dependant behaviour and the evaluation of its optical, electrical and magnetic properties.

- Chapter 5 addresses the preparation by direct mechanosynthesis of the $Bi_{1-x}Sm_xFeO_3$ system. The characterization of the crystal

structure, microstructure, temperature dependent behaviour and physical properties are also presented and discussed.

- Chapter 6 reports the densification of mechanosynthesised $BiFeO_3$ powders by the flash sintering technique. The effects of the applied electric field and current density on the purity, microstructure and electrical properties of the sintered materials are evaluated.

- Chapter 7 presents the preparation of $BiFeO_3$ by electric field-assisted solid-state reaction, also denominated flash synthesis, for the first time in literature. The reaction mechanism is also discussed and the quality of the prepared samples is tested by Rietveld refinement and impedance spectroscopy.

- Chapter 8 studies the thermal crystallization event in nanocrystalline $BiFeO_3$ powders by the combination of the information obtained from: X-ray thermodiffraction, transmission electron microscopy and differential scanning calorimetry.

- Chapter 9 summarizes the conclusions derived from this thesis.

3. MATERIALS AND METHODS

3.1. MATERIALS

The high purity commercially available oxides, listed in Table 3. 1, were used for the preparation of the multiferroic materials, without any further purification treatment.

Table 3. 1. Commercially available oxides employed for the preparation of the multiferroic materials.

Oxide	Catalogue Number	CAS Number	Purity (%)	Company
Bi_2O_3	223891	1304-76-3	≥99%	Sigma-Aldrich
Fe_2O_3	310050	1309-37-1	≥99%	Sigma-Aldrich
Yb_2O_3	246999	1314-37-0	≥99%	Sigma-Aldrich
Sm_2O_3	AB255271	12060-58-1	99.9%	ABCR GmbH

3.2. SAMPLE PREPARATION

3.2.1. Mechanochemical process

The different materials studied in this thesis were prepared by mechanosynthesis in a high-energy planetary ball mill. A planetary ball mill consists of at least one grinding jar which is arranged eccentrically on a rotating support disk. Figure 3. 1 illustrates the scheme of a planetary ball mill. A special drive mechanism causes the jars to rotate around their own axes (ω_v) while the supporting disk is rotating at the same time (ω_p), similarly to a planet-like movement. The jars and the supporting disk rotate in opposite directions and, therefore, the balls in the grinding jars

are subjected to superimposed rotational movements (Coriolis forces), that alternately act in like and opposite directions. This causes the grinding balls to run down the inside wall of the jar producing friction effect, followed by impact effect due to the collisions of the balls between them and with the opposite inside wall of the jars [1]. This allows the transmission of a high amount of energy to the reactants causing different physical and chemical phenomenon, such as particle size reduction, defects and the induction of chemical reactions, within others.

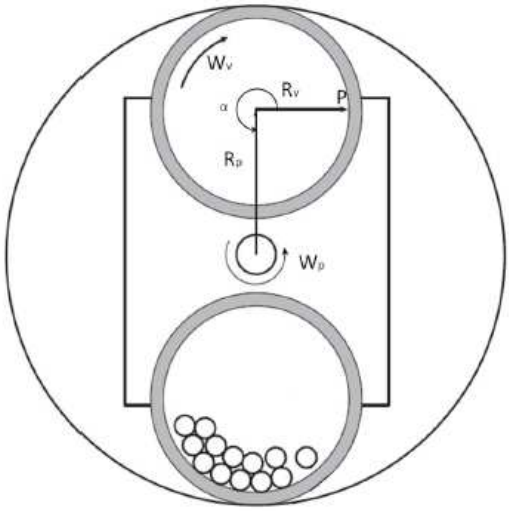

Figure 3. 1. Scheme of a planetary ball mill (modified from [2]).

A mechanochemical process is quite simple. It basically consists in mixing the stoichiometric amounts of the staring materials with the grinding media (balls) inside the jars, under a proper atmosphere and grinding for a certain period of time to induce the chemical reactions. However, as it was pointed out in Section 1.3, it is a stochastic process that depends on a considerable amount of experimental parameters.

Two different models of the planetary Micro Mills PULVERISETTE 7 (Fritsch, Idar-Oberstein, Germany) were used for the preparation of the samples in this thesis: the Premium Line (Figures 3.2 a) and b)) and the Classic Line (Figures 3.2 c) and d)).

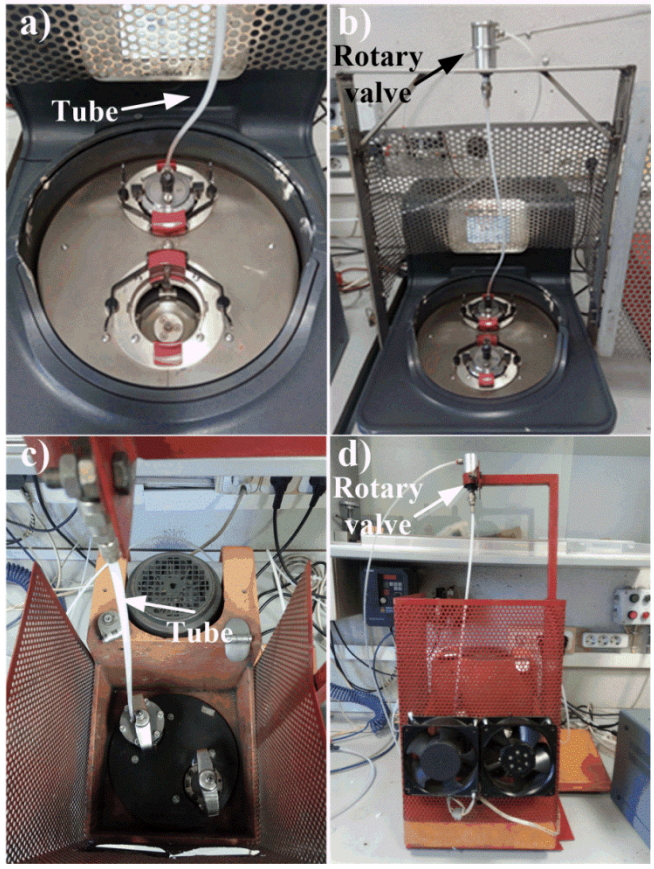

Figure 3. 2. Planetary Micro Mills PULVERISETTE 7: a), b) Premium Line model and c), d) Classic Line model.

Both mills have been modified to work under controlled atmosphere of gases. For this purpose, a rotary valve that allows the connection of the gas cylinder with the stainless steel jar during the whole milling experiment by means of a 5 mm diameter polyamide tube, has been incorporated to the mills (Figure 3. 2) [3]. These rotary valves are able to

work up to a maximum pressure of 70000 bar and a rotation speed of 25000 rpm. In order to maintain the pressure constant inside the jar, even if the gas is consumed during the reaction, the jars are equipped with a male taper straight adaptor and are sealed with a Viton O-ring. In all experiments, the jars were purged several times with the selected gas before starting the milling and then the desired pressure was selected and maintained during the whole milling treatment [3-5].

The experimental conditions for the mechanosynthesis of the $BiFeO_3$ related samples were optimized in previous research carried out by the group [6]. The most relevant parameters used in both mills are detailed as follows.

a) Planetary Micro Mill PULVERISETTE 7 Premium Line:

This mill was used for the preparation of samples in Chapters 4, 5 and 6.

- Type of jar and volume: due to the high resistance to abrasion, jars of tempered steel were used for the mechanosynthesis of all the samples. The jars have a diameter of 23.2 mm and a volume of 80 cm^3.
- Milling speed: the spinning rate of the supporting disk and the superimposed rotation in the opposite direction of the jars was set at 700 rpm.
- Grinding medium: 9 hardened stainless steel balls with a diameter of 15 mm (total mass of ~120 g).

- Extent of filling the jar: 1/5 approximately of the total volume of the jar.
- Ball-to-powder weight ratio (BPR): 1:20, which means that ~6 g of sample per jar can be obtained in each mechanosynthesis process.
- Atmosphere: 7 bar of oxygen in order to avoid bismuth reduction with the iron from the grinding media [3].
- Time: the milling time depends on the type of sample and its composition. All the mechanosynthesis reactions were monitored by powder X-ray diffraction, taking small amounts of the samples at different reaction times.

b) Planetary Micro Mill PULVERISETTE 7 Classic Line:

This mill was used for the preparation of samples in Chapter 8 (nanocrystalline $BiFeO_3$) [3, 6].

- Type of jar and volume: jars of tempered steel with a diameter of 19.8 mm and a volume of 45 cm^3 were used.
- Milling speed: the spinning rate of the supporting disk and the superimposed rotation in the opposite direction of the jars was also set at 700 rpm.
- Grinding medium: 6 hardened stainless steel balls with a diameter of 15 mm (total mass of ~81 g).

- Extent of filling the jar: 1/5 approximately of the total volume of the jar.
- Ball-to-powder weight ratio (BPR): 1:20. Approximately 4 g of sample per jar can be obtained in each mechanosynthesis process.
- Atmosphere: 7 bar of oxygen in order to avoid bismuth reduction with the iron from the grinding media.
- Time: 25 h of milling were required for the preparation of pure nanocrystalline $BiFeO_3$ powders.

3.2.2. Sintering

The densification of the powders obtained by mechanosynthesis was achieved by conformation using uniaxial pressing and sintering. As it has been introduced in Section 1.4, sintering is a complex process where solid-state mass transport occurs, reducing the particle interface/surface energy in order to form a dense body [7]. In this thesis, conventional sintering and flash sintering has been used in order to obtain dense specimens, particularly for the study of their electrical properties.

In conventional sintering, for the preparation of the green pellets, the collected mechanosynthesized powders were pressed into cylindrical pellets, by applying an uniaxial pressure of 0.93 GPa for 5 minutes in a stainless steel die 6.35 mm of diameter. The mass of the pellets was 400 mg approximately with a thickness of ~2 mm. The density of the green pellets, which was estimated geometrically, was above 75% of the theoretical density in every sample. Subsequently, the pellets were sintered in air in a Carbolite MTF 12/25 tube furnace (Carbolite, Bamford, England) at

temperatures ranging from 825 ^{o}C to 900 ^{o}C, and using different dwell steps, depending on the type of sample and its composition. In every case, the cooling and heating rates were both set at 10 ^{o}C min^{-1}.

As described in Section 1.4.3, flash sintering is a relatively new electric field-assisted sintering procedure developed in 2010 by Cologna et al. [8]. It basically consists in applying an electric field directly to the specimen, allowing the current to flow through the sample [8, 9]. The mechanosynthesized powders were pressed into dog-bone shaped specimens, using the die depicted in Figures 3.3 a) and b) and by applying a uniaxial pressure of 250 MPa [10]. Details about the dog-bone sample dimensions are shown in Figure 3. 3 c), which thickness was of 1 mm approximately, when 800 mg of powders were used. Platinum paste was applied in the holes of the green-body samples, in order to improve the electrical contact with the electrodes.

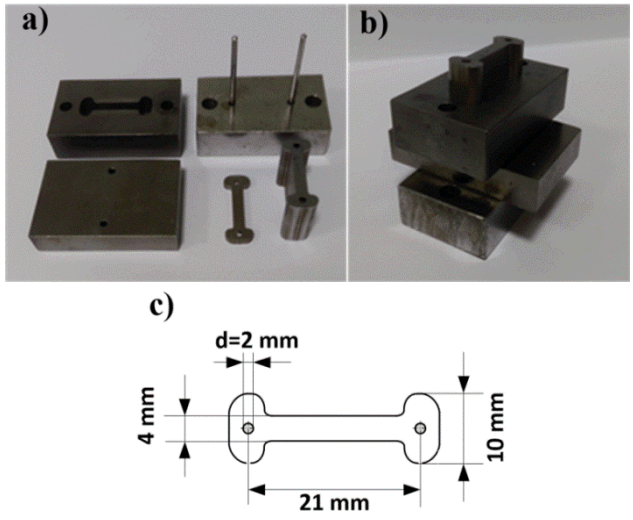

Figure 3. 3. a), b) Dog-bone die and c) Dog-bone sample dimensions.

Due to the lack of commercially available instruments to carry out flash sintering experiments, we designed and assembled our own experimental setup. Figure 3. 4 shows the experimental equipment and scheme used for flash sintering experiments. It consists in a homemade assembled tubular furnace with a quartz tube of 4 cm diameter was used. The furnace temperature was controlled by an Eurotherm 3216 PID controller with a K-type thermocouple (Chromel/Alumel), placed in the vicinity of the sample. This thermocouple was used simultaneously for controlling the furnace temperature and measuring the sample temperature. The samples were held inside the furnace, by two platinum wires (electrodes), which were connected to a EA-PS 8720-15 DC power supply, 3000 W (EA Elektro Automatik, Helmholtzstraße, Germany). Current and voltage measurements were taken by means of a two channels Keithly 2110 5 ½ digital multimeter (Keithley Instruments, Cleveland, USA), connected in series and parallel, respectively, with the electrical circuit. Current and voltage data were acquired by the KI-Tool software. The shrinkage of the samples was monitored by a 1/3 inch Sony CCD sensor camera (Imaging Source DMK 23U445) with a resolution of 1290x960 and 30 fps. A 6X (18–108 mm FL) C-Mount, close focus zoom lens protected with a heat absorber glass KG-3 50x50 mm (Edmund Optics) was used in order to magnify the images. At the left end of the furnace a 37 mm ultraviolet filter was used as optical window. An auxiliary external light was also employed to enhance the images contrast.

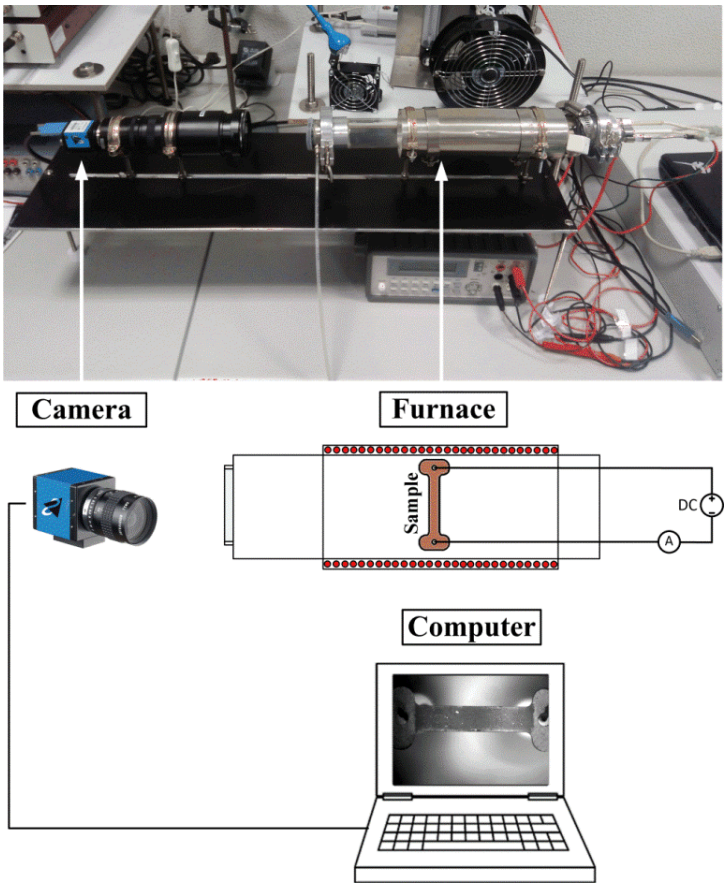

Figure 3. 4. Flash sintering and synthesis setup and scheme.

All the experiments were performed at a constant heating rate of 10 $^{o}C\ min^{-1}$ until the flash event took place, in an airflow of 100 $cm^3\ min^{-1}$. Images were acquired by the IC-Capture software (Imaging Source) at a rate of one image per second in the vicinity of the flash.

3.2.3. Flash synthesis

Inspired by the flash sintering procedure, and as one step further, the effect of the electric field on the solid-state reaction synthesis of $BiFeO_3$ from the pristine oxides, Fe_2O_3 and Bi_2O_3, was explored. It is addressed in

Chapter 7. For this purpose, stoichiometric amounts of Bi_2O_3 and Fe_2O_3 were ball milled for 15 minutes, in order to obtain a homogenous mixture of the starting oxides, using the planetary Micro mill Pulverisette 7 Premium Line, as described in Section 3.2.1. Subsequently, the powders were uniaxially pressed into dog-bone-shaped green bodies, employing the die depicted in Figure 3. 3. The green bodies were flashed according to the protocol detailed in Section 3.2.2, using the homemade assembled experimental setup (Figure 3. 4).

3.2.4. Density measurements

The density of the resulting sintered pellets was determined by the Archimedes' method. This method is particularly useful for irregular shaped specimens. The operational procedure consists in weighting the sample at room temperature (m_{sample}). Subsequently, it is submerged in distilled water, in order to measure the displaced volume of liquid ($m_{water\ displaced} \cdot \rho_{water}^{-1}$). Thus, the density is calculated by equation (3. 1):

$$\rho_{sample} = \frac{m_{sample}}{m_{water\ (displaced)}} \rho_{water} \qquad (3.\ 1)$$

In this work, a Density Determination Kit mounted on an AB2014-S analytical balance (Mettler Toledo) was used.

3.3. SAMPLE CHARACTERIZATION

Several characterization techniques were used to study the samples in terms of crystal structure, chemical composition, microstructure, multiferroic behaviour and the optical, electrical and magnetic properties.

3.3.1. Powder X-ray diffraction and Rietveld refinement

X-ray diffraction (XRD) is probably the most used characterization technique in Material Science. It allows the qualitative identification of the crystalline phases presented in a material. Each crystalline phase has its own characteristic XRD pattern which may be used as a "finger print" for its identification. Moreover, high quality XRD patterns can provide quantitative information about the different phases in a sample, being also possible the refinement of the unit cell size and atom positions [11].

For all the mechanosynthesized samples prepared in this thesis, powder X-ray diffraction was used in order to study the obtained crystalline phases and identify the possible presence of impurities or secondary phases. Routine XRD data were collected in a Rigaku Miniflex diffractometer working at 45 kV and 40 mA, using CuK_α radiation, which generates the X-ray beam at a wavelength of 1.540530 Å. The working conditions were typically 2θ scanning between 5º–90º, with a 0.02º step and a scan speed of 0.24 seconds per step. Longer measurements and, therefore, higher quality patterns were collected in order to obtain enough resolution to refine the structures. For this purpose, a PANalytical X'Pert PRO diffractometer was used, working at 45 kV and 40 mA, using CuK_α radiation (λ = 1.540530 Å) and equipped with an X'Celerator detector and a graphite diffracted beam monochromator. In this case, the patterns were taken in a wider range of 2θ, from 15º to 140º, with a 0.005º step and a scan speed of 1.5 seconds per step.

Powder X-ray thermodiffraction patterns were collected in two different instruments:

- A Philips X'Pert Pro diffractometer equipped with a high temperature Anton Paar camera working at 45 kV and 40 mA, using CuK_α radiation (λ = 1.5405 Å) and equipped with an X'Celerator detector and a graphite diffracted beam monochromator, at Instituto de Ciencia de Materiales de Sevilla (ICMSE-CSIC). The patterns were collected in different 2θ ranges depending on the samples, a step of 0.022° and a speed scan of 0.2 seconds per step and under airflow of 100 $cm^3\,min^{-1}$.
- A Bruker D8 Advance diffractometer working at 40 kV and 40 mA and equipped with an Anton Paar XRK 900 high temperature chamber, a Bruker Vantec 1 position-sensitive detector with radial Soller slits, and Göbel mirrors (Bruker, Germany) with parallel Johansson geometry in the incident beam for CuK_α radiation (λ = 1.5405 Å), at Centro de Investigación Tecnología e Innovación de la Universidad de Sevilla (CITIUS). Measurements were taken within a 2θ range from 20° to 60°, a step of 0.022°, a scan speed of 0.2 seconds per step and a continuous 100 $cm^3\,min^{-1}$ flow of N_2 by means of a GM50A MKS mass flow controller calibrated for N_2 as received.

All the diffractometers used in this thesis were calibrated according to the manufacturer specifications. Lanthanum hexaboride, LaB_6, and silicon, Si, standards were used to check the resolution in a wide range of angles.

Rietveld refinements were carried out in order to obtain structural and quantitative information about the phases presented in the mechanosynthesized samples. This method allows obtaining lattice parameters, atomic positions and the quantification of the crystalline

phases presented in a sample with more accuracy [12]. Rietveld refinement uses a non-lineal least squares algorithm to adjust a theoretical and an experimental pattern taking into account structural, microstructural and instrumental data. The FullProf [13] and Topas software were used for this purpose. A six order polynomial function was employed for the background refinement, whereas a Thompson-Cox-Hastings pseudo-Voigt with convoluted axial divergence asymmetry profile function was used to refine peak shapes. Background, scale factors, lattice parameters, peak widths and asymmetry were refined simultaneously. Atomic positions and isotropic temperature factors were subsequently included in the refinement after convergence. The values of the goodness of fit (χ^2) were checked to obtain values close to the unit, while values of residual factors (weighted profile R-factor (R_{wp}), expected R-factor (Rexp) and R_{Bragg}) were obtained, as small as possible, reaching coherent values [14].

3.3.2. Raman spectroscopy

Raman spectroscopy is widely used for the characterization of compounds, as it is able to provide information about the chemical structure and the different phases present in a sample. Raman spectroscopy relies on the inelastic scattering of monochromatic light, usually from a laser source, and its iteration with a sample, giving place to the so-called Raman effect. In other words, photons of the laser light are absorbed by the sample and then reemitted but with a frequency that is shifted up or down with respect the monochromatic frequency. The analysis of the spectra provides information about vibrational and rotational energies of molecular bonds [15].

In this thesis, Raman spectra of the samples were recorded at room temperature by a dispersive Horiva Jobin Yvon LabRam HR800 microscope equipped with a 20 mW green laser (532.14 nm) and a 100X objective with a confocal pinhole of 10 µm.

3.3.3. Differential scanning calorimetry (DSC)

Differential scanning calorimetry (DSC) is a thermoanalytic technique that measures the difference of heat flow between a sample and an inert reference as a function of temperature. The heat flow should be the same until some thermal event such as melting, phase transitions or decomposition takes place. It is translated to extra heat input to the sample or reference depending on whether the process is endothermic or exothermic, respectively [16]. This themoanalytic characterization technique is particularly useful for the study of the multiferroic behaviour of $BiFeO_3$ and related materials.

In this thesis, the DSC curves were measured in a wide range of temperatures, from -50 ^oC to 850 ^oC. Two different equipments were used depending on the temperature range. From -50 ^oC to 400 ^oC a DSC Instrument (Q200, TA Instruments, Crawley, UK) was used, whereas from 400 ^oC to 850 ^oC a simultaneous TG/DSC Instrument (Q600 SDT, TA Instruments, Crawley, UK) was employed. Approximately 40 mg of the samples were placed in open alumina pans. The experiments were registered at the heating rate of 10 ^oC min^{-1} and under airflow of 100 cm^3 min^{-1}. The Néel and Curie transition temperatures where considered at the minimum of the endothermic peak.

3.3.4. Scanning electron microscopy (SEM)

The scanning electron microscope (SEM) uses a focused beam of high-energy electrons to generate a variety of signals at the surface of solid specimens. These signals, derived from electron-sample interactions, reveal information about the sample, including chemical composition, external surface features, texture and topography. This is due to the depth of focus of SEM instruments that allow generating pictures of three-dimensional quality. SEM instruments cover a wide range of magnification normally from 10^{-2} to 10^{2} μm, approximately [11]. Samples require specific preparation before measuring in SEM, as they should be totally dried, due to the vacuum conditions required for the electrons to form the images and, in addition, it is normally necessary to coat the electrically insulating samples with a thin layer of conductive material, such as gold or graphite, to prevent the build-up of charge in the surface of the solid.

Within the signals generated by the interaction between the bean of high-energy electrons and the sample, secondary electrons (SE), backscattered electrons (BSE) and X-ray are of particular relevance in scanning electron microscopy. In this thesis just SE and X-ray have been used for the characterization of the samples by SEM. SE are electrons of low energy coming from the atoms in the sample which provide topographic information of the surface of the sample in grayscale. Additionally, the X-ray generation is characteristic of each element presented in the sample, hence, qualitative and semiquantitative compositional information of the sample can be provided as well, by either scanning the wavelength dispersed (WD) or energy dispersed (ED) [17].

In this thesis, the microstructure, morphologic and chemical composition of the samples was studied using a Hitachi S-4800 SEM-FEG, equipped with an energy dispersive X-ray spectrometer (EDX), Quantax Bruker. The field-emission gun operated at 2 kV for obtaining the micrographs, while for EDX analysis, it operated at 20 kV. The samples in the shape of pellets required previous surface preparation including polishing and thermal etching for 30 minutes at temperatures of 90% of those used for their sintering, in order to reveal grain boundaries. Moreover, some of the samples were Au sputter-coated due to its insulating nature at room temperature, using an Emitech K550 Sputter Telstar (Barcelona, Spain).

3.3.5. Transmission electron microscopy (TEM)

In transmission electron microscopy (TEM), a beam of high energy electrons (100-800 kV) is transmitted through an ultra-thin specimen, generating an image from the interaction of the transmitted electrons with the sample, which is magnified and focused onto an imaging device, such as a fluorescent screen or a charge-coupled device (CCD camera) [18]. Particularly, high-resolution electron microscopy (HR-TEM) is a powerful tool in imaging defects, as it is capable of giving information on an atomic scale, by direct lattice imaging.

TEM can be operated in several modes. Bright field image is the most common mode of operation, where the image is directly formed from the direct beam by its interaction with the sample. The contrast depends on mass-thickness, crystallinity and the atomic mass of the atoms in the sample. Thicker and heavy atoms enriched areas appear dark, while no sample regions appear bright. Dark field image is another mode of

operation, where the direct beam is blocked by the aperture and only the beams diffracted from the particles of interest are allowed to recombine to form the image. Hence, only regions of the samples that are diffracting the beams to the selected area appear bright, whereas no sample regions or regions that transmit the beam appear dark. This mode is particularly useful to distinguish between different crystalline features and regions [19].

Electron diffraction patterns can be also generated by TEM. This technique is known as selected aperture electron diffraction (SAED), as electrons are dispersed elastically, satisfying diffraction condition of the sample's crystal structure and indicating a crystallographic direction. Generally, SAED patterns are formed by a number of well-defined spots that depends on the orientation of the specimen for monocrystalline samples, or a serial of rings for polycrystalline and amorphous samples. SAED is a powerful tool that allows a detailed study of the symmetry, orientation and crystallographic planes of the selected area [18, 19].

The instruments employed for the TEM characterization of the samples were:

- A 200 kV TEM Philips CM 200 microscope with B_6La filament, located in the Instituto de Ciencia de Materiales de Sevilla (ICMSE-CSIC).
- A high resolution TEM with field mission gun (FEG-HRTEM) from FEI Company, USA, (Model TECNAI G2 F30 S-twin), with a Fischione high angle annular dark-field detector (HAADF) Instruments, USA (0.16 nm point resolution) to work in STEM mode and one INBCA ZX-max 80 silicon drift detector for EDS analysis. The experiments were performed at 300 kV with a

resolution of 0.2 nm. This instrument is located in the Instituto de Ciencia de Materiales de Sevilla (ICMSE-CSIC).

- A 300 kV JEOL JEM 3010 UHR electron microscope with a LaB_6 electron source and equipped with a Semi STEM, located in the Institute of Inorganic Chemistry of the Czech Academy of Science in Řež, Czech Republic.

The samples for TEM measurements were prepared by dispersing the powders in isopropanol for 1 hour, picking up a drop of the diluted supernatant and the subsequent deposition in a glass sample holder. Immediately, the carbon coated grids were smoothly rubbed in the deposited drops. Then, the grids were dried slowly at room temperature for the solvent evaporation. The analysis of high resolution micrographs and the first Fourier transform for phase interpretation were performed with Digital Micrograph software (Gatan Inc., USA) and the Java version of JEM Software.

3.3.6. UV-Visible spectroscopy

The optical properties of the samples were determined by ultraviolet-visible spectroscopy (UV-Visible spectroscopy). This characterization technique relies on the principle that under certain conditions, materials absorb or emit energy. Particularly, this technique uses light in the visible, near-UV and near-infrared region, which translated to an energy scale correspond approximately from 102 to 104 kJ mol^{-1}, and are often associated with colour. Moreover, this is typically the same range of the energy required for transitions of electrons between the outermost energy levels. Thus, various types of electronic transitions can occur, providing valuable information about the studied materials and

specifically local structure, as the positions of the absorption bands are sensitive to coordination environment and bond character [11]. In this thesis, UV-Visible spectroscopy was used to determine the energy band gap of the mechanosynthesized materials, as the promotion of electrons from the valence band to the conduction band in semiconductors lies between the visible and UV-region.

UV-Vis measurements were recorded in a UV-Vis spectrophotometer (Perkin-Elmer Lambda 35, Massachusetts, USA) equipped with an integrating sphere and were taken over a wavelength range from 400 nm to 800 nm. Barium sulphate was used as coated standard pattern. The energy band gap (E_g) values were calculated by means of Tauc's plot:

$$\alpha(h\upsilon) = A(h\upsilon - E_g)^{n/2} \quad (3.2)$$

Where α is the absorption coefficient, $h\upsilon$ is the photon energy, A is a constant and n depends on the type of optical transition [20]. For $BiFeO_3$ and related materials the band gap is direct and, therefore, n equals 1 [21, 22]. Thus, the band gap energy, E_g, can be estimated from the plot of $(\alpha h\upsilon)^2$ versus photon energy ($h\upsilon$), through the extrapolation of a tangent line from the point of inflection to $(\alpha h\upsilon)^2 = 0$.

3.3.7. Dielectric thermal analysis (DEA)

Dielectric thermal analysis (DEA) is commonly used to characterize the response of materials by analysing separately the dielectric and resistive contribution, normally in terms of dielectric constant (also known as relative permittivity), ε_r, and dielectric loss, $tan\delta$. An electric field at fixed frequency is applied to a sample as a function of temperature [23].

Besides the dielectric response, DEA allows the identification of phase transition temperatures. Particularly, in ferroelectric materials, the dielectric constant experiment a dramatic increment in the vicinity of the Curie temperature.

In this thesis, DEA was used to study the nature of the phase transitions of the prepared samples. Relative permittivity, ε_r, and $tan\,\delta$ measurements were carried out on sintered pellets from 50 ºC to 450 ºC, using a 4263B LCR meter (Agilent Technologies, California, USA) at a fixed frequency of 10^5 Hz. All the data were corrected taking into account the geometry of the pellets, whose opposite faces were previously Au sputter-coated using an Emitech K550 Sputter Telstar (Barcelona, Spain).

3.3.8. Impedance spectroscopy

Impedance spectroscopy is a powerful technique for the analysis of the electrical properties of electroceramics, because it enables characterizing separately the resistive (R) and reactive (C) contribution of the different electro-active region in the sample. In other words, the macroscopic dielectric constant in polycrystalline materials commonly consists in several contributions, such as interfacial phenomena (sample-electrode), grains and grain boundaries. The deconvolution of these different contributions is totally essential for a proper understating of the functionality of the material [24-27]. Additionally, and besides the electrical microstructure characterization to the different electro-active regions presented in the sample, additional information can be provided, such as the assessment of the electrical homogeneity as well as information related to the charge transport mechanism, by performing experiments in

different oxygen partial pressure atmospheres, variable temperature and dc bias [27].

Impedance measurements are carried out over a wide range of frequencies, commonly from 10^{-2} to 10^{7} Hz. Impedance, Z, can be defined as the ratio of voltage, V, and current, I:

$$Z = \frac{V}{I} \quad (3.\ 3)$$

Experimentally, it is measured using a low voltage applied across a sample, which can be expressed according to equation (3. 4) as a function of time, t:

$$V = V_0 \sin(\omega t) \quad (3.\ 4)$$

Where V_0 is the amplitude and ω is the angular frequency:

$$\omega = 2\pi \mathrm{f} \quad (3.\ 5)$$

Being f the frequency. The resulting current, I, can be determined as:

$$I = I_0 \sin(\omega t + \varphi) \quad (3.\ 6)$$

Where I_0 is the amplitude and φ is the phase difference between the applied voltage, V, and the resulting current, I. This phase difference, φ, is directly related to the reactive component, C, of the system due to the different dielectric relaxations that take place in the sample, whereas the total magnitude of impedance is related to the resistive component, R [25]. The data are normally expressed in the complex impedance notation:

$$Z^* = (Z' + iZ'') \quad (3.\ 7)$$

Where the real part, Z', and the imaginary part, Z'', are measured separately, being i the imaginary number. The different electro-active regions of a sample are characterized according to their dielectric relaxation times or time constants. These regions are described by a resistance and a capacitance, usually placed in parallel, commonly known as RC elements [24, 25]. The characteristic relaxation time or time constant, τ, of each RC element is given by the product of R and C:

$$\tau = RC \quad (3.8)$$

In the frequency domain, each RC element can be separated due to the following relationship:

$$2\pi f_{max} RC = 1 \quad (3.9)$$

Where f_{max} is the frequency of maximum loss in the impedance spectrum [25]. The separation of different dielectric relaxations depends on the resolution of their associated time constants.

Impedance data are typically represented in the form of imaginary (Z'') versus real (Z') impedances, which is known as the complex impedance plot. The parallel RC elements normally give different semicircles in the complex impedance plot, from which the R and C values can be obtained. The values of R for each electro-active regions can be directly obtained from the intercept of each semicircle on the real impedance axis, Z', of the complex impedance plot (Figure 3. 6 a)). Ideally, the values of C can be obtained by applying equation (3. 9) [24]. The origin of each dielectric relaxation can be identified by means of the capacitance value of its associated RC element, according to the classification proposed by Irvine et al., as shown in Table 3. 2. [24].

Table 3. 2. Capacitance value and their possible interpretation [24].

Capacitance (F)	Phenomenon Responsible
10^{-12}	Bulk
10^{-11}	Minor, secondary phase
10^{-11}-10^{-8}	Grain boundary
10^{-10}-10^{-9}	Bulk ferroelectric
10^{-9}-10^{-7}	Surface layer
10^{-7}-10^{-5}	Sample-electro interface
10^{-4}	Electrochemical reacions

Besides complex impedance, Z^*, and in order to help with the data interpretation, other formalisms are used, such as admittance, Y^*, electric modulus, M^*, and complex permittivity, ε^* [25]. They are defined by the following equations:

$$Y^* = \frac{1}{Z^*} \qquad (3.\ 10)$$

$$M^* = i\omega C_0 Z^* \qquad (3.\ 11)$$

$$\varepsilon^* = \frac{1}{M^*} = \frac{Y^*}{i\omega C_0} \qquad (3.\ 12)$$

Being C_0 the vacuum capacitance of the empty measuring cell, which is defined as:

$$C_0 = \varepsilon_0 \frac{A}{l} \qquad (3.\ 13)$$

Where ε_0 is the permittivity of free space ($8.854 \cdot 10^{-14}$ F cm^{-1}) and A and l are the electrode area and separation, respectively. In order to carry out a detailed electrical characterization, these formalisms are useful because they highlight different characteristics of a sample. Due to their

mathematical interrelation, these formalisms can be subdivided in two different sets: Z^*-$M^*$and Z^*-ε^*, where just one of them is often used for data interpretation. For instance, taking into account the Z^*-M^* set, the complex impedance, Z^*, is dominated by elements with the highest resistivity and, therefore, it is particularly useful to analyse the grain boundary response, whereas the complex modulus, M^*, is dominated by elements with low capacitances such as grain or bulk responses [24-26]. The complex admittance, Y^*, and permittivity, ε^*, provide information about the conductivity and permittivity of the sample, respectively.

The brickwork model is the most widely used model for impedance spectroscopy data interpretation in polycrystalline ceramics. It assumes that, with appropriate electrodes, the ceramics are composed by conductive grains, surrounded by thin resistive grain boundary layers, which can be modelled by an equivalent circuit of two RC elements connected in series [28]. A scheme of the brickwork model is illustrated in Figure 3.5, for a ceramic composed of cube-shaped grains of dimensions l_1 separated from each other by a boundary of thickness l_2 and l_3 from the electrodes [24].

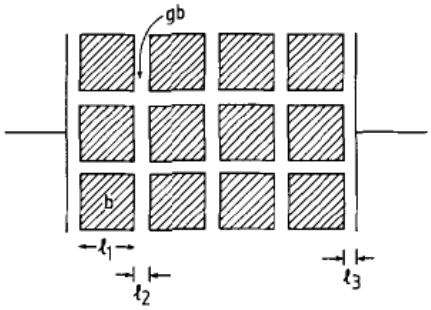

Figure 3.5. Brickwork model of grain and grain boundary regions in a ceramic between metal electrodes [24].

As an example to illustrate the brickwork model, two RC elements in parallel associated with bulk (R_b, C_b) and grain boundaries (R_{gb}, C_{gb}) responses are simulated, whose values R_b, C_b, R_{gb} and C_{gb} are 1 MΩ cm, 10 pF cm^{-1}, 100 MΩ cm and 1 nF cm^{-1}, respectively. Figure 3. 6 a) shows the impedance complex plane plot for the simulated data, where a perfect semicircular arc associated with the highly resistive grain boundary component dominates the impedance. The inset in Figure 3. 6 a) shows the impedance of the most conductive component, associated with the bulk response. Each R value can be obtained from the intercept of each semicircular arc on the Z' axis, whereas the C values are determined from equation (3. 9), as it is indicated in both, Figures 3.6 a) and b). Figure 3. 6 b) shows the Z''/M'' spectroscopy plots, where Z'' and M'' are plotted versus frequency. It can be clearly observed that the Z'' peak is dominated by the grain boundary response at low frequency, while M'' is dominated by the bulk response, which has lower C value, at high frequency.

In summary, for a proper data interpretation, ideally different electro-active elements should show different properties with respect to each other, so that they can be modelled as a single equivalent circuit component, RC, which enables to account for their individual contribution in the resistive (R) and reactive (C) responses. The associated phenomenon for each contribution can be assigned according to its capacitance value, C, taking into account the values of Table 3. 2. Additionally, temperature-dependent measurements can help to discriminate between similar electrical responses with overlapping capacitance values.

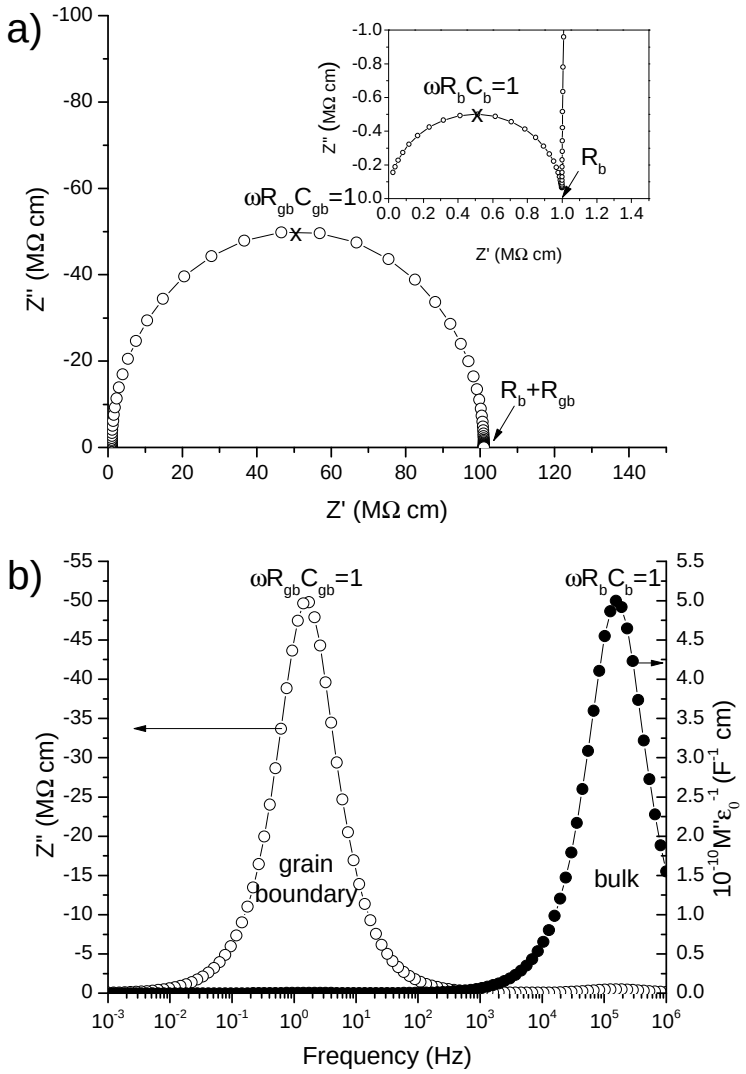

Figure 3. 6. a) Complex impedance plane plot, b) Z''/M'' spectroscopic plots for the simulated impedance data.

The activation energy for conduction for each electro-active region in a sample can be calculated from temperature-dependent impedance measurements. The conductivity values for each electro-active region at different temperatures (calculated from the resistivity values, R_T, obtained

from Figure 3. 6 a) can be plotted in conventional Arrhenius format according to equation (3. 14):

$$\sigma = \sigma_0 exp\left[-\frac{E_a}{kT}\right] \quad (3.\ 14)$$

Where σ is the conductivity at each temperature, σ_0 is the pre-exponential factor, E_a is the activation energy, k is the Boltzman constant ($8.617343 \cdot 10^{-5}$ eV K^{-1}) and T is the temperature expressed in Kelvins. Taking logarithms and rearranging equation (3. 14):

$$ln\sigma = ln\sigma_0 - \frac{E_a}{kT} \quad (3.\ 15)$$

Expressing equation (3. 15) in base-10 logarithms:

$$log\sigma = \left[-\frac{E_a}{1000k} loge\right]\frac{1000}{T} + log\sigma_0 \quad (3.\ 16)$$

The activation energy for conduction for each electro-active region of the samples, E_a, can be calculated according to equation (3. 16), by the slope of the plot of the logarithm of the conductivity ($log\sigma$) versus $1000/T$.

The impedance measurements in this thesis were carried out on sintered pellets with a PMS 1735 Newtons4th Ltd Impedance Analyser (IA) (Loughborough, UK), over a frequency range from 1 Hz to 5 MHz, using an ac measuring voltage of 0.1 V and a temperature range from 300 ^{o}C to 380 ^{o}C. Measurements were carried out taking into account the blank capacitance of the conductivity jig and the overall pellets geometry, whose opposite faces were previously Au sputter-coated using an Emitech K550 Sputter Telstar (Barcelona, Spain). Figure 3. 7 shows the furnace and the sample holder employed to carry out the measurements.

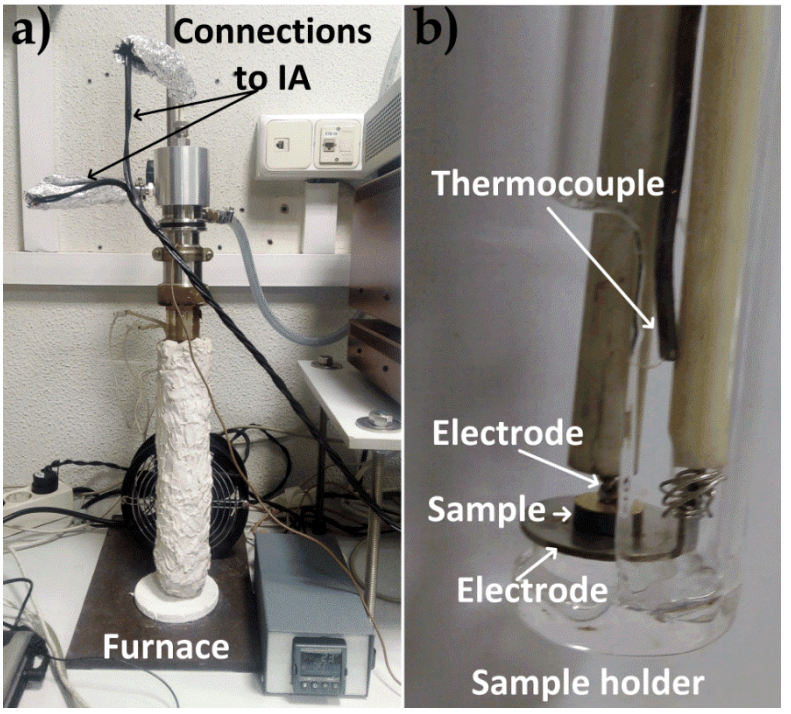

Figure 3. 7. a) Furnace with impedance analyser (IA) connections and b) Sample holder employed to carry out the impedance measurements.

3.3.9. Magnetic properties

Magnetic properties were measured in a Quantum Design MPMS-SQUID magnetometer (magnetic properties measurement system-superconducting quantum interference device). This instrument is extremely sensitive to magnetic flux and it is based on the tunnelling of superconducting electrons across a narrow insulating gap, between two superconductors (Josephson junction) [29, 30]. The magnetization versus magnetic field data (hysteresis loops) was recorded at 5 K and 350 K in magnetic field strength up to ±5 Tesla for ytterbium and samarium substituted $BiFeO_3$ samples (Chapters 4 and 5).

3.4. REFERENCES

[1] Suryanarayana C., *Mechanical Alloying and Milling*, ed. Dekker Marcel. **2004**, New York.

[2] Sopicka-Lizer M., ed. *High-energy ball milling. Mechanochemical processing of nanopowders*. **2010**, Woodhead Publishing Limited: Oxford, Cambridge, New Delhi.

[3] Perejon A., Murafa N., Sanchez-Jimenez P.E., Criado J.M., Subrt J., Dianez M.J. and Perez-Maqueda L.A., *Direct mechanosynthesis of pure $BiFeO_3$ perovskite nanoparticles: reaction mechanism*. Journal of Materials Chemistry C, **2013**, 1 (22), p. 3551-3562.

[4] Gotor F.J., Alcala M.D., Real C. and Criado J.M., *Combustion synthesis of TiN induced by high-energy ball milling of Ti under nitrogen atmosphere*. Journal of Materials Research, **2002**, 17 (7), p. 1655-1663.

[5] Criado J.M., Alcala M.D. and Real C., *Influence of the atmosphere control during the grinding of titanium powder on its reactivity towards the conversion into titanium nitride*. Solid State Ionics, **1997**, 101, p. 1387-1391.

[6] Perejon A., *Mecanosíntesis y caracterización de los materiales multiferroicos nanoestructurados $Bi_{1-x}R_xFeO_3$ (R = La, Y)*, in *ICMSE-CSIC*. **2012**, Universidad de Sevilla: Sevilla. p. 240.

[7] Kang S.-J.L., *Sintering: Densification, Grain Growth and Microstructure*. **2004**, Oxford: Butterworth-Heinemann.

[8] Cologna M., Rashkova B. and Raj R., *Flash Sintering of Nanograin Zirconia in <5 s at 850°C*. Journal of the American Ceramic Society, **2010**, 93 (11), p. 3556-3559.

[9] Yu M., Grasso S., McKinnon R., Saunders T. and Reece M.J., *Review of flash sintering: materials, mechanisms and modelling*. Advances in Applied Ceramics, **2017**, 116 (1), p. 24-60.

[10] Francis J.S.C., *A study on the phenomena of flash-sintering with tetragonal zirconia* in *Department of Mechanical Engineering*. **2013**, University of Boulder: Boulder. p. 189.

[11] West A.R., ed. *Basic Solid State Chemistry*. 2nd ed. **1999**, John Wiley & Sons, LTD: Chichester, New York.

[12] Rietveld H., *A profile refinement method for nuclear and magnetic structures*. Journal of Applied Crystallography, **1969**, 2 (2), p. 65-71.

[13] Rodriguez-Carvajal J., *In Fullprof: A Program for Rietveld Refinement and Pattern Matching Analysis* in *Satellite Meeting on Powder diffraction of the XV Congress of the IUCr*. **1990**.

[14] Toby B.H., *R factors in Rietveld analysis: How good is good enough?*. Powder Diffraction, **2006**, 21 (1), p. 67-70.

[15] Ferraro J.R., Nakamoto K. and Brown C.W., *Introductory Raman Spectroscopy*. 2nd ed. **2003**, San Diego: Academic Press.

[16] *Interpretating DSC curves. Part 1: Dynamic measurements*. UserCom, **2000**, 11.

[17] Vernon-Parry K.D., *Scanning electron microscopy: an introduction*. III-Vs Review, **2000**, 13 (4), p. 40-44.

[18] Williams D.B. and Carter C.B., *Transmission Electron Microscopy: A Textbook for Materials Science*. **2009**: Springer.

[19] Egerton R.F., *Physical Principles of Electron Microscopy. An Introduction to TEM, SEM, and AEM*. **2005**: Springer.

[20] Tauc J., Grigorov R. and Vancu A., *Optical properties and electronic structure of amorphous germanium*. Phys. Status Solidi, **1966**, 15 (2), p. 627-637.

[21] Hauser A.J., Zhang J., Mier L., Ricciardo R.A., Woodward P.M., Gustafson T.L., Brillson L.J. and Yang F.Y., *Characterization of electronic structure and defect states of thin epitaxial $BiFeO_3$ films by UV-visible absorption and cathodoluminescence spectroscopies*. Applied Physics Letters, **2008**, 92 (22), p. 222901.

[22] Kim Y.I., Atherton S.J., Brigham E.S. and Mallouk T.E., *Sensitized layered metal-oxide semiconductor particles for photochemical hydrogen evolution from nonsacrifical electron-donors*. Journal of Physical Chemistry, **1993**, 97 (45), p. 11802-11810.

[23] Wu Y.-J., Chen X.-K., Zhang J., Liu J., Xiao W.-S., Wu Z. and Chen X.-J., *Pressure effect on structural and vibrational properties of Sm-substituted $BiFeO_3$*. Journal of Applied Physics, **2013**, 114 (15).

[24] Irvine J.T.S., Sinclair D.C. and West A.R., *Electroceramics: Characterization by Impedance Spectroscopy*. Advanced Materials, **1990**, 2 (3), p. 132-138.

[25] Sinclair D.C., *Characterization of electro-materials using ac impedance spectroscopy*. Boletín de la Sociedad Española de Cerámica y Vidrio, **1995**, 34 (2), p. 10.

[26] West A.R., Sinclair D.C. and Hirose N., *Characterization of Electrical Materials, Especially Ferroelectrics, by Impedance Spectroscopy*. Journal of Electroceramics, **1997**, 1 (1), p. 65-71.

[27] Barsoukov E. and Macdonald J.R., *Impedance Spectroscopy: Theory, Experiment, and Applications*, ed. Sons John Wiley &. **2005**.

[28] Fleig J. and Maier J., *The impedance of ceramics with highly resistive grain boundaries: Validity and limits of the brick layer model*. Journal of the European Ceramic Society, **1999**, 19 (6-7), p. 693-696.

[29] Clarke J., *Squids*. Scientific American, **1994**, 271 (2), p. 46-53.

[30] Kleiner R., Koelle D., Ludwig F. and Clarke J., *Superconducting quantum interference devices: State of the art and applications*. Proceedings of the IEEE, **2004**, 92 (10), p. 1534-1548.

4. MECHANOCHEMISTRY OF THE $Bi_{1-x}Yb_xFeO_3$ SYSTEM

4.1. INTRODUCTION

As stated in Section 1.2.5, the partial substitution of Bi^{3+} for isovalent cations has been widely employed, not only for obtaining phase-pure $BiFeO_3$ related materials but also for improving the ferroelectric properties, reduction of leakage currents and enhancement of the magnetoelectric coupling. The partial substitution of Bi^{3+} with small rare earth cations, such as Yb^{3+}, is attractive because it may lead to an enhanced lattice distortion and consequently an increase in the ferroelectric polarization of the materials [1]. Nevertheless, the existing literature about the $Bi_{1-x}Yb_xFeO_3$ system is quite limited and significant discrepancies can be found [1-4]. For instance, there is no clear consensus about the Yb content that induces phase transitions and the crystal structures that the system adopts. In addition, a full characterization in terms of structural analysis, electrical and magnetic properties has not been reported [1-4].

The mechanochemical synthesis of $BiFeO_3$ and related materials has been shown to be an effective preparation method, from which truly phase-pure and highly insulating compounds can be obtained [5-7]. To the best of our knowledge, the preparation of the $Bi_{1-x}Yb_xFeO_3$ system has just been addressed by hydrothermal synthesis, rapid liquid phase sintering, a modified sol-gel method and conventional solid-state reaction [1-4]. Thus,

exploring the preparation of the partial substitution of $BiFeO_3$ with ytterbium by mechanochemistry is of the most interest.

4.2. OBJECTIVES

The objective of this chapter is the preparation of the $Bi_{1-x}Yb_xFeO_3$ system by mechanosynthesis, as an alternative route for the synthesis of these materials, as well as to carry out a complete characterization of the samples by means of XRD, DSC, SEM, UV-Vis spectroscopy, impedance spectroscopy and magnetic measurements.

4.3. EXPERIMENTAL

Samples of the $Bi_{1-x}Yb_xFeO_3$ system in the nominal compositional range x = 0.02, 0.05 and 0.07, were prepared by mechanochemistry followed by sintering, according to the procedure detailed in Section 3.2.1 (Chapter 3). All the pellets were conventionally sintered at 825 ^oC for 6 min in air.

4.4. RESULTS AND DISCCUSION

4.4.1. Mechanosynthesis and sintering

Samples of the $Bi_{1-x}Yb_xFeO_3$ system in the nominal compositional range x = 0.02, 0.05 and 0.07, were prepared by mechanosynthesis followed by sintering. Figure 4. 1 shows the XRD patterns of the powders obtained for each composition after different milling times.

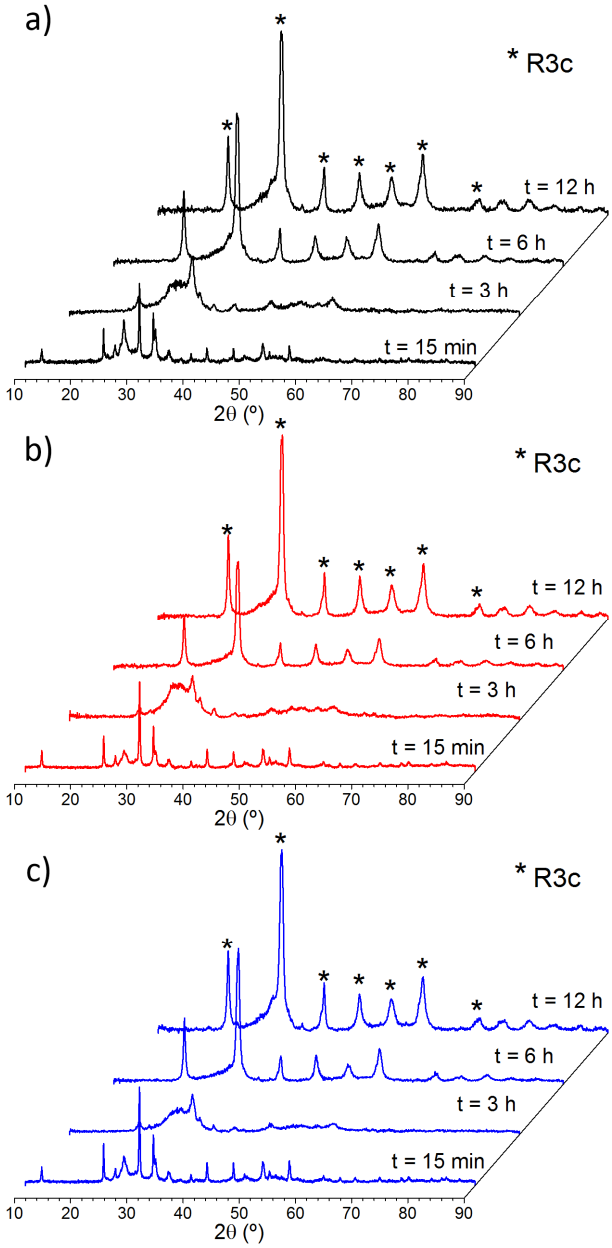

Figure 4. 1. XRD patterns of powders obtained after milling 15 min, 3 h, 6 h and 12 h stoichiometric amounts of the single oxides in oxygen (7 bar) for different nominal compositions: a) x = 0.02, b) x = 0.05, c) x = 0.07.

The starting oxides suffer an initial amorphization during the milling treatment, as inferred from the comparison of the XRD patterns registered after 15 min and 3 h of milling of Figure 4. 1. The amorphization is followed by the crystallization of the new phases as grinding proceeds up to 6 h. In terms of milling time, the same behaviour was observed for each composition prepared. Further mechanical treatments did not produce modifications in the powders, as it is observed from XRD measurements after 12 h of milling (Figure 4. 1). In order to avoid contamination from the grinding media, the optimum milling time was taken at 6 h for every composition.

The evolution of the microstructure of the milled powders as a function of time was followed by SEM. SEM micrographs for nominal x = 0.02, x = 0.05 and x = 0.07 compositions after different milling times are shown in Figure 4. 2. Similar features are observed for every nominal composition as milling proceeds. After short milling times (15 min, Figures 4. 2 a), d) and g)), the morphology of the powders is plate-like, due to delamination of bismuth oxide, mixed with ytterbium oxide and iron oxide particles. As milling continues up to 3 h (Figures 4. 2 b), e) and h)), the morphology changes to highly aggregated powders. Finally, after 6 h of mechanical treatment the obtained powders are composed of aggregated nanometric subunits, as it can be observed in Figures 4. 2 c), f) and i).

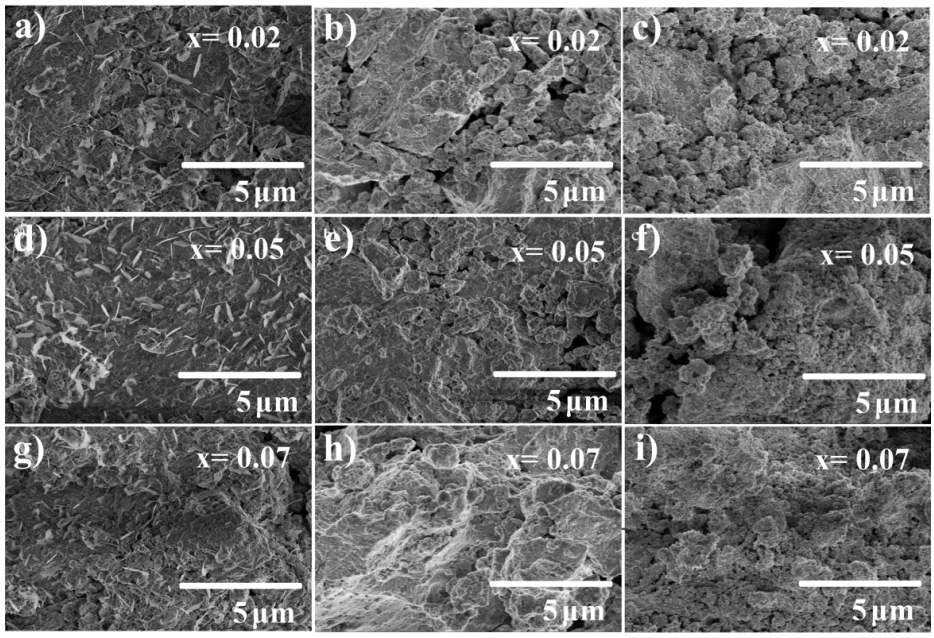

Figure 4. 2. SEM micrographs of powders of the $Bi_{1-x}Yb_xFeO_3$ samples with nominal x = 0.02, x = 0.05 and x = 0.07 compositions, at different milling times, 15 min (a, d, g), 3 h (b, e, h) and 6 h (c, f, i).

Due to the nanometric size of the crystallites obtained after milling, the XRD peaks are quite broad (Figure 4. 1), which made difficult to obtain detailed crystallographic information. In order to increase the crystallinity, the milled powders of each nominal composition were pressed into pellets and conventionally sintered at 825 ^oC for 6 min. These sintering conditions were considered optimal after studying their influence on the purity and density of the ceramics. The resulting pellets density was 7.3 g cm^{-3} (89%), 6.9 g cm^{-3} (83%) and 6.8 g cm^{-3} (82%) for the samples with nominal x = 0.02, 0.05 and 0.07 compositions, respectively. Figure 4. 3 shows the XRD patterns of the sintered samples. Although the main phase can be indexed in the R3c space group, typical from the parent $BiFeO_3$ compound, small reflections corresponding to other phases are observed in the samples with nominal x = 0.05 and x = 0.07 compositions. Moreover, the intensity of

these reflections increases with the ytterbium content of the samples, which suggests that the solubility limit of ytterbium in the $BiFeO_3$ lattice has been reached.

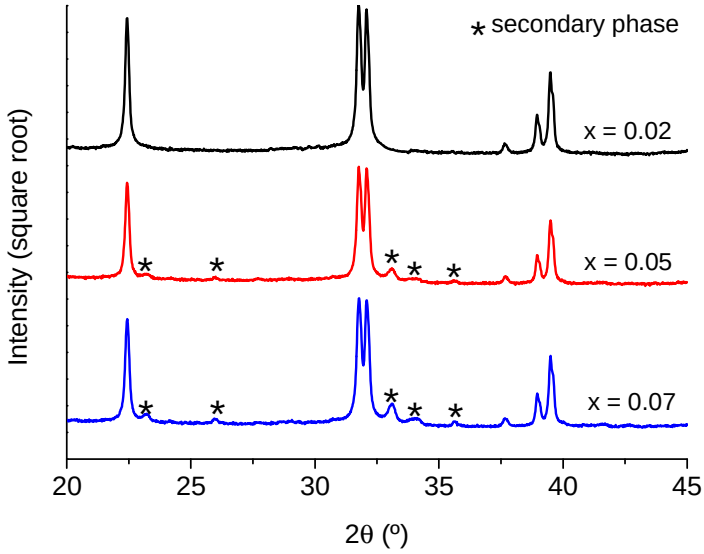

Figure 4. 3. XRD patterns of the samples obtained after milling for 6 h and sintering $Bi_{1-x}Yb_xFeO_3$ powders of nominal compositions: a) x = 0.02, b) x = 0.05 and c) x = 0.07. The intensity is represented in square root in order to make the secondary phase more noticeable.

4.4.2. Solubility limit determination

DSC resulted an useful characterization technique for the estimation of the solubility limit of ytterbium in $BiFeO_3$ (and, therefore, the stoichiometry of the main phase for the nominal x = 0.05 and x = 0.07 compositions) since a linear relationship between the Curie temperature (T_C) and the real composition (x) of bismuth substituted samples has been reported [8]. Figure 4. 4 depicts the DSC curves registered from 300 ºC to 850 ºC for the nominal x = 0.02, 0.05 and 0.07 compositions.

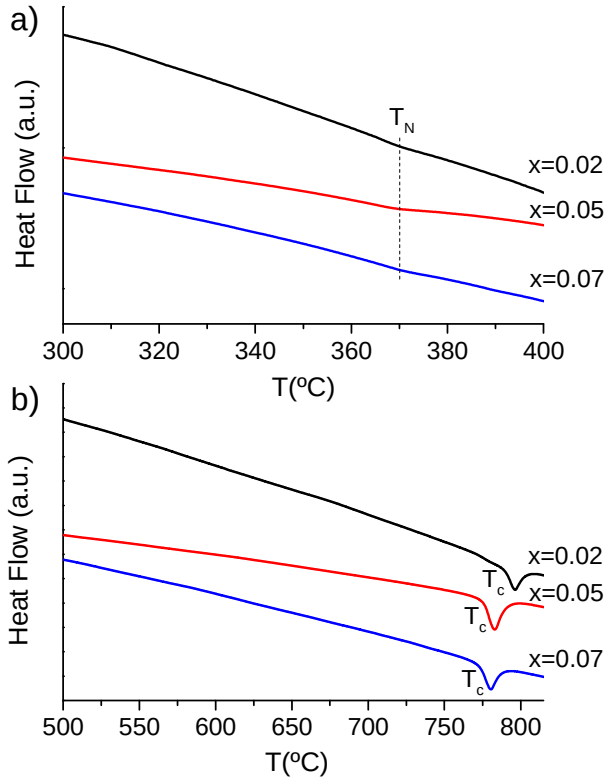

Figure 4. 4. DSC traces for the $Bi_{1-x}Yb_xFeO_3$ samples with x = 0.02 and nominal 0.05 and 0.07 compositions, obtained after milling for 6 h and sintering at 825 ºC: a) temperature range from 300 ºC to 400 ºC, b) temperature range from 500 ºC to 825 ºC. The dashed line in a) is a guide to the eye.

Two endothermic peaks are observed in the DSC traces for all samples. The first one appears at approximately 370 ºC and corresponds to the Néel temperature (T_N), (Figure 4. 4 a)), associated with the second order phase transition (antiferromagnetic-paramagnetic) and remaining constant for all compositions. The second peak (Figure 4b) is more intense and corresponds to the T_C (ferroelectric-paraelectric transition) [9, 10]. The sample with composition x = 0.02 presents the T_C at 796 ºC while for

nominal x = 0.05 and x = 0.07 compositions the T_C appears at 783 °C and 780 °C, respectively. These two last values are very close to each other. The similarity of T_C for the samples with nominal x = 0.05 and x = 0.07 compositions suggests that the Yb solubility limit has been reached somewhere between x = 0.02 and 0.05. For pure $BiFeO_3$ prepared by mechanochemistry, the T_C is observed at 828 °C [6]. Considering the linear relationship between T_C and composition, the solubility limit of ytterbium in the system $Bi_{1-x}Yb_xFeO_3$ can be determined by extrapolation from Figure 4. 5. Thus, it can be estimated that the solubility limit of ytterbium in the $Bi_{1-x}Yb_xFeO_3$ system is reached at approximately x = 0.03. Therefore, the secondary phases observed in Figure 4. 3 may correspond to ytterbium rich compounds, whose concentration increases with the ytterbium content of the system.

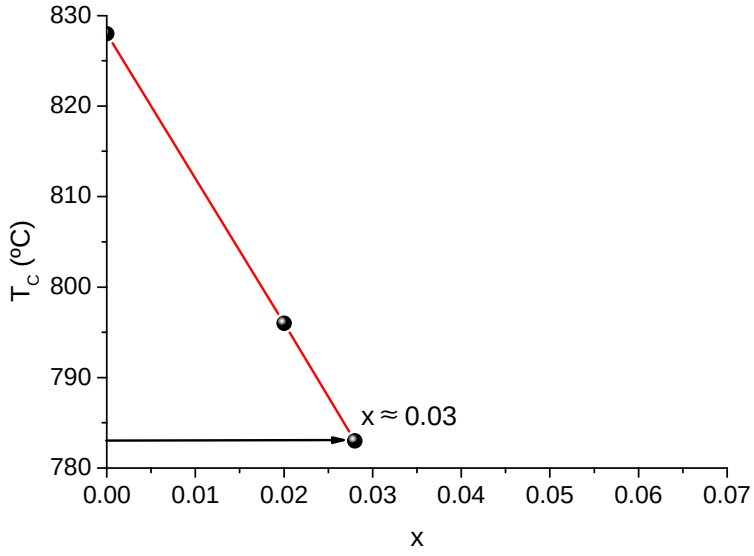

Figure 4. 5. T_c versus composition for the $Bi_{1-x}Yb_xFeO_3$ samples.

4.4.3. Structural characterization

Rietveld analyses were carried out to obtain detailed crystallographic information of the phases existing in each sample depending on its nominal composition. Figure 4. 6 shows the refinement of the X-ray diffraction data for the sample of composition x = 0.02. It can be successfully fitted in a rhombohedral R3c structure with good reliability factors, which indicates that this compound is essentially phase pure (See Table 4. 1).

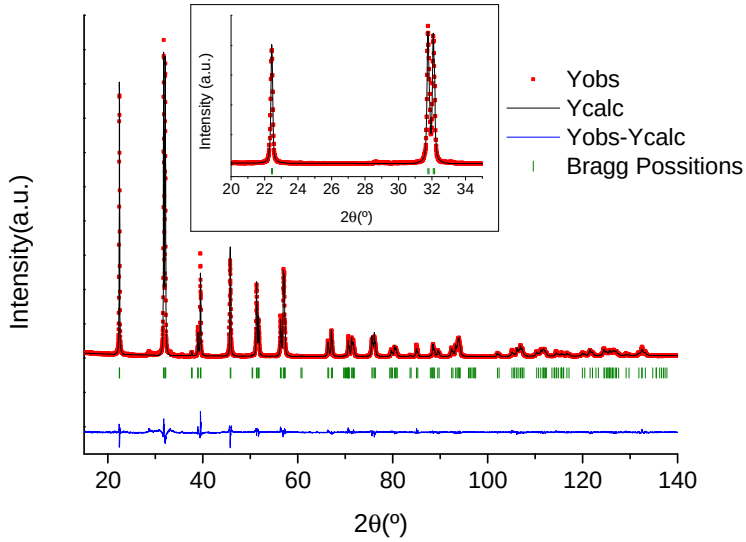

Figure 4. 6. XRD pattern obtained for the sample with x = 0.02 composition obtained after milling for 6 h and sintering at 825 ºC (dots). The solid lines are the fit from the Rietveld refinement. Bragg reflections for R3c space group are indicated by sticks. The inset shows an enlarged part of the diffraction data in the 2θ region from 20º to 35º.

On the other hand, analogous data from nominal x = 0.05 and x = 0.07 compositions exhibit the main R3c phase together with small reflections, that increase with ytterbium content, at the 2θ values of 23.2º,

26º, 33º, 34º and 35.6º. Figure 4. 7 shows the Rietveld refinement for the nominal x = 0.05 composition. The diffraction pattern was refined considering a real composition of x = 0.03, as estimated from the T_C data obtained by DSC (Figure 4. 5) and a rhombohedral R3c structure. The small peaks of the secondary phase were not considered in the refinement. As it may be seen, rhombohedral R3c phase accounts for all the main peaks and the diffraction pattern can be refined with good confidence factors (Table 4. 1). Unfortunately, the secondary phase, which would correspond to an ytterbium enriched phase, cannot be identified due to the low intensity of the diffraction peaks contributed by this phase.

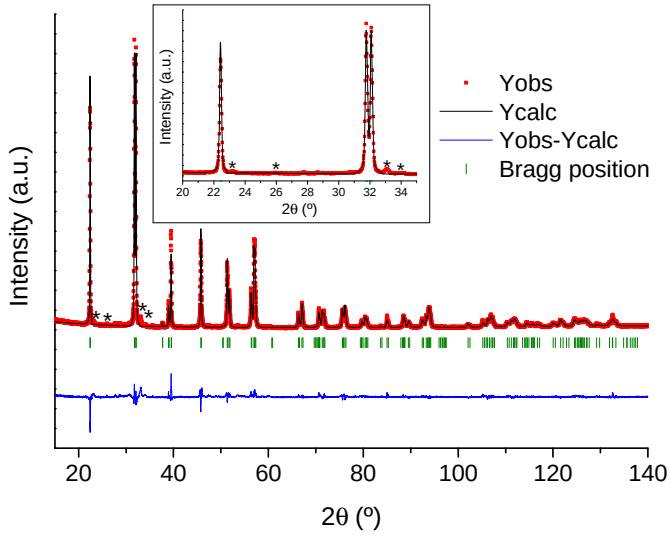

Figure 4. 7. XRD pattern obtained for the sample with nominal x = 0.05 composition obtained after milling for 6 h and sintering at 825 ºC (dots). The solid lines are the fit from the Rietveld refinement. Bragg reflections for R3c space group are indicated by sticks. The inset shows an enlarged part of the diffraction data in the 2θ region from 20º to 35º.

As it can be observed in Figure 4. 8, a very similar refinement is obtained for the nominal x = 0.07 composition, considering again that the

main phase corresponds to a rhombohedral R3c structure with x = 0.03 composition. Moreover, the values of the structural parameters extracted from the Rietveld analysis are comparable with those obtained for nominal x = 0.05 composition.

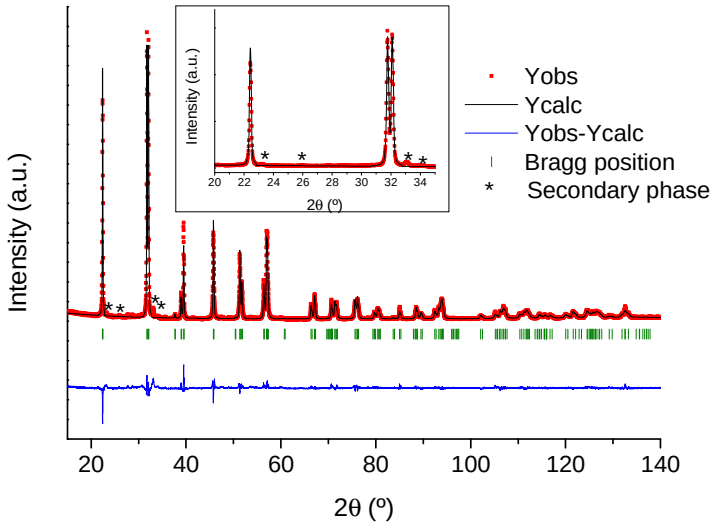

Figure 4. 8. XRD pattern obtained for the sample with nominal x = 0.07 composition obtained after milling for 6 h and sintering at 825 ºC (dots). The solid lines are the fit from the Rietveld refinement. Bragg reflections for R3c space group are indicated by sticks. The inset shows an enlarged part of the diffraction data in the 2θ region from 20º to 35º.

Therefore, it can be concluded from the X-ray diffraction data that while composition x = 0.02 forms a single $Bi_{0.98}Yb_{0.02}FeO_3$ phase, the compositions x = 0.05 and x = 0.07 form two-phase mixtures of a majority rhombohedral phase of approximate composition $Bi_{0.97}Yb_{0.03}FeO_3$ and an unidentified ytterbium rich phase. This result is in agreement with the DSC data analysis shown in Section 4.4.2.

Table 4. 1. Rietveld refinement structural parameters obtained from the XRD patterns for the $Bi_{1-x}Yb_xFeO_3$ samples with x = 0.02 composition and nominal x = 0.05 and 0.07 compositions obtained after milling for 6 h and sintering at 825 °C.

Nominal composition	x = 0.02	x = 0.05	x = 0.07
Real composition	$Bi_{0.98}Yb_{0.02}FeO_3$	$Bi_{0.97}Yb_{0.03}FeO_3$	$Bi_{0.97}Yb_{0.03}FeO_3$
Space group	R3c	R3c	R3c
a (Å)	5.5771(1)	5.5759(2)	5.5759(1)
b (Å)	-	-	-
c (Å)	13.8648(1)	13.8603(2)	13.8597(2)
Volume (Å3)	373.48	373.20	373.20
Atomic positions			
Bi	0.00, 0.00, 0.00	0.00, 0.00, 0.00	0.00, 0.00, 0.00
Yb	0.00, 0.00, 0.00	0.00, 0.00, 0.00	0.00, 0.00, 0.00
Fe	0.00, 0.00, 0.22131(3)	0.00, 0.00, 0.22120(2)	0.00, 0.00, 0.22179(7)
O (1)	0.44481(2), 0.01524(4), 0.95134(3)	0.44520(5), 0.02460(5), 0.94920(6)	0.43758(3), 0.02510(5), 0.94949(6)
Confidence factors			
R_{Bragg}	7.7	7.6	8.4
R_{exp}	5.7	5.3	5.1
R_{wp}	11.7	10.4	11.5
χ^2	4.2	3.8	4.9

Table 4. 1 lists the structural parameters extracted from the Rietveld analysis of all three samples. Additionally, a slight tendency of volume decrease with x is observed up to the solubility limit x = 0.03, which can be attributed to the difference in ionic radii of bismuth and ytterbium. The tolerance factor (t), proposed by Goldschmidt, accounts for the structural distortions from the ideal cubic perovskite (t = 1) due to the ionic radii of the atoms in the A and B positions [11], according to equation (1.1) (Section 1.2.1). When the tolerance factor is smaller than one, the B-O

bonds are compressed whereas the A-O bonds are under tension, causing the BO_6 octahedra to tilt co-operatively to relieve the lattice stress [12, 13]. For Yb-substituted $BiFeO_3$, the average ionic radii of Bi^{3+} and Yb^{3+} (A site atoms) are considered in eightfold coordination (values not reported for twelvefold coordination) and the ionic radii of Fe^{3+} (B-site atom) in sixfold coordination and high spin. According to Shannon, the ionic radii of Bi^{3+} and Yb^{3+} are 1.17 Å and 0.985 Å, respectively [14]. Consequently, the calculated tolerance factors for the sample of x = 0.02 composition is 0.8873 and for the samples of nominal x = 0.05 and x = 0.07 compositions is 0.8867. Thus, in Yb-substituted $BiFeO_3$, Yb^{3+} does not fill the A-site space fully and the FeO_6 octahedra tilts to shrink the space, which induce more buckling in the Fe-O-Fe bond angle [9, 15]. As an example, the perovskite crystal structure of the sample of composition x = 0.02 is shown in Figure 4. 9.

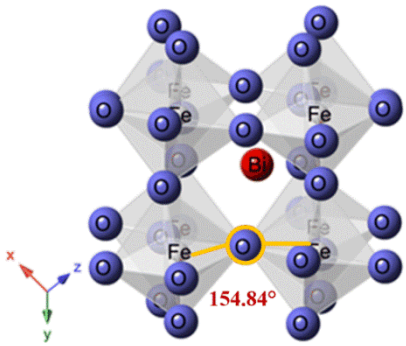

Figure 4. 9. Perovskite crystal structure of the sample of composition x = 0.02.

The Raman spectra of the sintered samples are shown in Figure 4. 10. It can be observed that all samples exhibit a Raman spectra very similar to that of $BiFeO_3$ (space group R3c), which has 13 active Raman modes: $4A_1+9E$ [16]. The sample of x = 0.02 composition (Figure 4. 10 a)) exhibits

12 bands: four of them correspond to A_1 vibrational modes (at 157, 173, 222 and 411 cm^{-1}), whereas the others can be attributed to E vibrational modes (at 263, 279, 290, 347, 370, 470, 522, 615 cm^{-1}). Additionally, some differences are observed between the samples. As the amount of ytterbium increases, there is a small shift of the bands to higher wavelengths and two of them disappear (279 and 347 cm^{-1}). Moreover, the bands associated with the A_1 vibrational modes bellow 200 cm^{-1} (159 and 170 cm^{-1}), decrease their relative intensity. It may be attributed to the partial substitution of bismuth by ytterbium in the structure, as this behaviour is similar to that observed for the introduction of other substituents in the A position of the $BiFeO_3$ perovskite [7, 17-19].

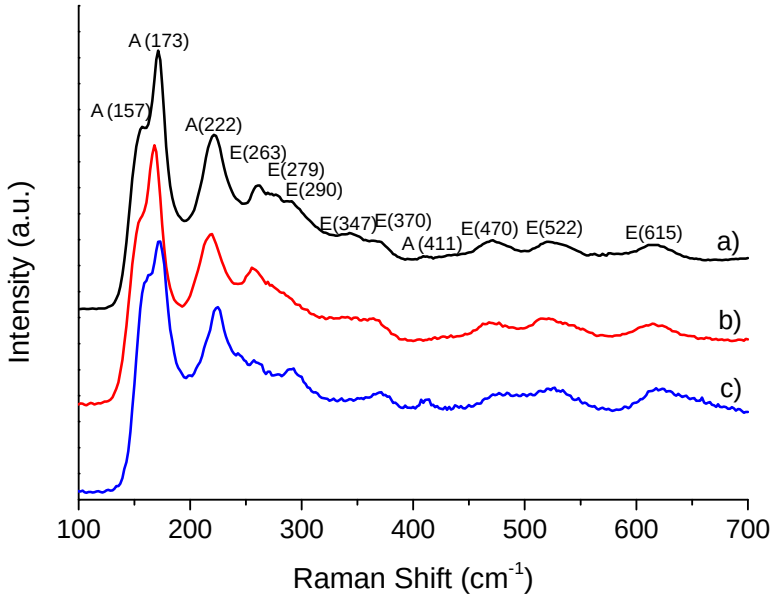

Figure 4. 10. Raman spectra of the samples obtained after milling for 6 h and sintering at 825 °C: a) x = 0.02 composition, b) nominal x = 0.05 and c) nominal x = 0.07 compositions.

4.4.4. Temperature-dependent behaviour

The temperature dependant behaviour of the $Bi_{1-x}Yb_xFeO_3$ system was also studied by means X-ray thermodiffraction. Figure 4. 11 presents the temperature-dependent XRD patterns, recorded from 766 ºC to 800 ºC in the 2θ range from 30º to 34º, for the samples obtained after milling for 6 h and sintering at 825 ºC. As temperature increases the samples suffer a phase transformation from R3c to Pnma (ferroelectric-paraelectric transition), which is reflected in the double peak, at approximately 31.5º-32º, that becomes to three overlapping peaks very close together. Additionally, the temperature ranges at which the phase transformations take place are consistent with the obtained transitions in the DSC data (Figure 4. 4 b)), confirming the decrease of T_C as the concentration of ytterbium increases. A similar behaviour has been observed for other substituents [7, 8]. It is worth noting that the T_C of the nominal x = 0.05 and x = 0.07 compositions, observed in the diffraction data, are very close to each other, in agreement with the DSC data, suggesting that these samples are two-phase mixtures of an x = 0.03 phase and an ytterbium rich phase.

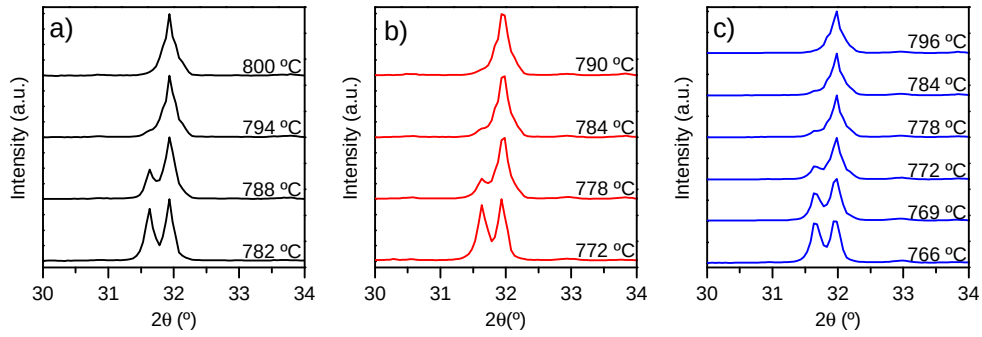

Figure 4. 11. Temperature-dependent XRD patterns of the $Bi_{1-x}Yb_xFeO_3$ samples obtained after milling for 6 h and sintering at 825 ºC: a) x = 0.02, b) nominal x = 0.05 composition, c) nominal x = 0.07 composition.

4.4.5. Microstructural and chemical characterization

SEM micrographs of the different samples, milled for 6 h and then sintered at 825 °C, are shown in Figures 4. 12 a), c) and e). Pellets were thermally etched for 30 min at 90% of the sintering temperature to reveal the grain boundaries. The microstructure is granular in all the samples. The grain size distribution is more homogenous in the sample of x = 0.02 composition (Figure 4. 12 a)), with typical values between approximately 1 and 3 μm. When the amount of ytterbium increases the grain size decreases to values smaller than 2 μm. Moreover, the porosity also increases with the amount of substituent, in agreement with the calculated densities (reported in Section 4.4.1). The EDX spectrums of the samples are shown in Figures 4. 12 b), d) and f) for x = 0.02 composition and nominal x = 0.05 and x = 0.07 compositions, respectively. The elemental composition has been determined by a semiquantitative analysis of the EDX spectra, as it is presented in Table 4. 2. The experimental results are mostly coincident with the expected values, being an indication that the initial stoichiometry has not been modified during the preparation of the samples. However, slight differences, which can be attributed to the intrinsic errors of the EDX, are observed.

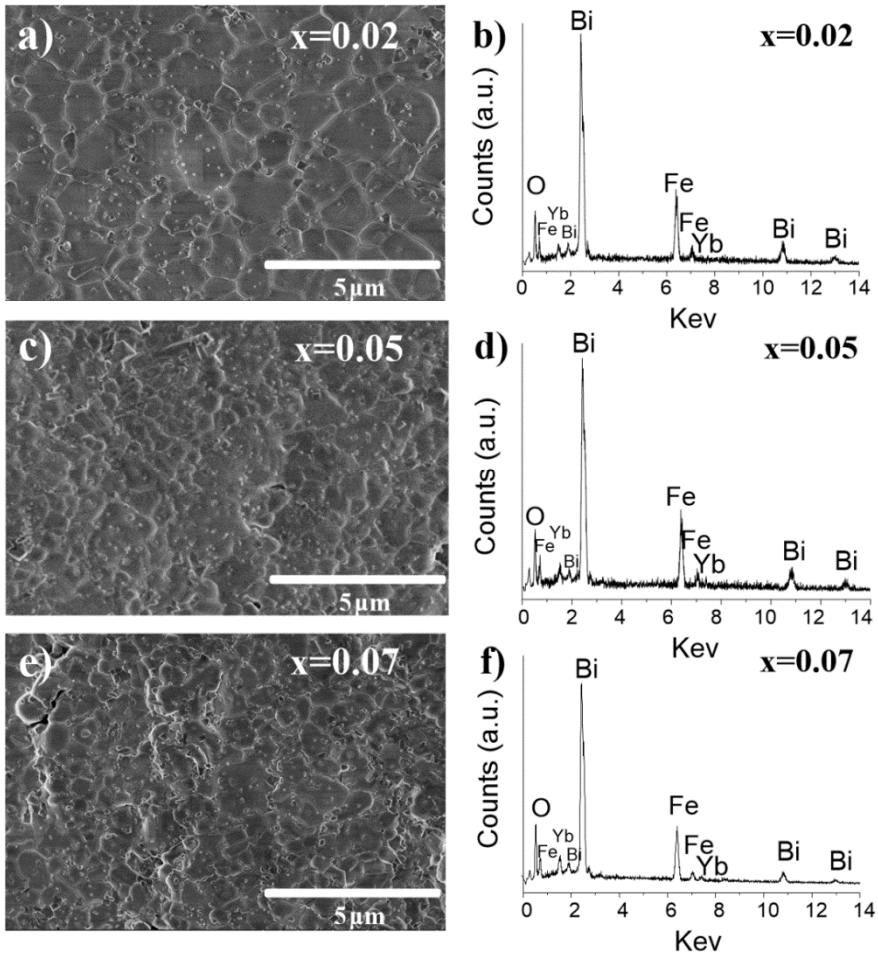

Figure 4. 12. SEM micrographs and EDX spectrum of the $Bi_{1-x}Yb_xFeO_3$ samples obtained after milling for 6 h and sintering at 825 °C.

Table 4. 2. Elemental atomic composition of the $Bi_{1-x}Yb_xFeO_3$ samples obtained after milling for 6 h and sintering at 825 °C, determined by a semiquantitative analysis of EDX spectra.

		Experimental atomic composition (%)		
Sample (Nominal compositions)	Theoretical atomic composition Fe/Yb/Bi (%)	Fe	Yb	Bi
$Bi_{0.98}Yb_{0.02}FeO_3$	50/1/49	53.62±3.04	1.02±0.28	45.36±3.52
$Bi_{0.95}Yb_{0.05}FeO_3$	50/2.5/47.5	53.94±3.07	2.45±0.34	43.61±3.73
$Bi_{0.93}Yb_{0.07}FeO_3$	50/3.5/46.5	53.56±3.01	2.78±0.77	43.66±1.41

4.4.6.Optical properties

The optical properties of the samples were studied by measuring their UV-Vis diffuse reflectance absorption spectra. Figure 4. 13 shows the absorption spectra of the samples of the different compositions obtained after milling for 6 h and sintering at 825 ^oC. It can be clearly observed that the samples absorb considerable amount of light in the visible region, which suggests their potential use as visible-light photocatalysts. As $BiFeO_3$ and related materials are considered direct band gap semiconductors, n is equal to 1 in Tauc's plot (equation (3.2), Chapter 3). Thus, the band gap energy can be estimated from the plot of $(\alpha h\nu)^2$ versus photon energy $(h\nu)$, through the extrapolation of a tangent line from the point of inflection to $(\alpha h\nu)^2 = 0$ [20, 21], as it is shown in the insets of Figure 4. 13. The band gap energy values are 2.06 eV for the sample of x = 0.02 composition and 2.04 eV for both samples with nominal x = 0.05 and 0.07 compositions. This is again another indication that these two last samples contain the same $Bi_{1-x}Yb_xFeO_3$ phase. These values of band gap energy are smaller than those previously reported for pure $BiFeO_3$ [9, 22, 23], or those reported for ytterbium substituted $BiFeO_3$ [2]. Hence, this suggests that ytterbium substituted samples prepared by mechanosynthesis may be good photocatalytic materials.

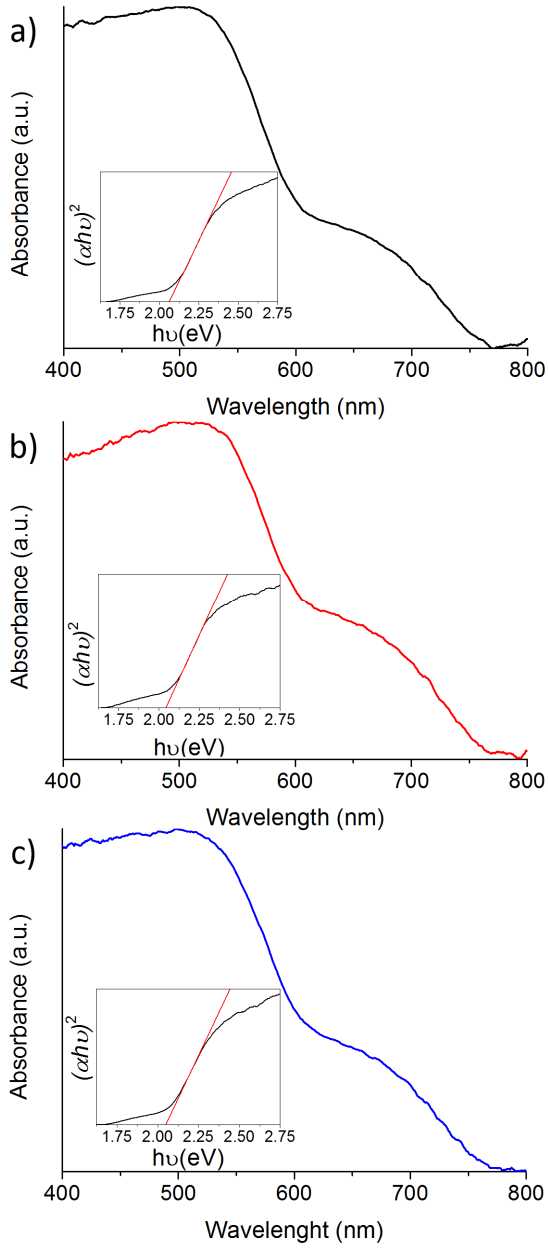

Figure 4. 13. UV-Vis diffuse reflectance spectra of the $Bi_{1-x}Yb_xFeO_3$ samples obtained after milling for 6 h and sintering at 825 °C: a) x = 0.02 composition, b) nominal x = 0.05 and c) nominal x = 0.07 compositions. The insets represent $(\alpha h\upsilon)^2$ versus photon energy for the calculation of the corresponding band gap energy.

4.4.7. Electrical properties

The electrical properties of the samples were studied by impedance spectroscopy. Similar results were obtained from all the samples. Thus, they resulted to be highly insulating at room temperature, presenting modest levels of conductivity from 300 ºC. For this reason, the impedance measurements were carried out from this temperature. The impedance complex plane plots of the samples at different temperatures are constituted by single slightly distorted arcs, as shown in Figures 4. 14 a), 4. 15 a) and 4. 16 a) for x = 0.02, nominal x = 0.05 and x = 0.07 compositions, respectively. For every sample, the associated Z''/M'' spectroscopic plots at 380 ºC show single peaks with small displacements between them for the maxima frequencies (Figures 4. 14 b), 4. 15 b) and 4. 16 b)). These results suggest that the samples are electrically homogenous due to the absence of any additional peaks at lower frequencies in the Z'' spectrum, despite the presence of the small amount of ytterbium enriched secondary phase for the samples with nominal x = 0.05 and 0.07 compositions. The capacitance values are presented in Figures 4.14 c), 4. 15 c) and 4. 16 c). The capacitance remains approximately constant in the entire frequency range for the three samples. Hence, the electrical homogeneity of the samples is again evidenced.

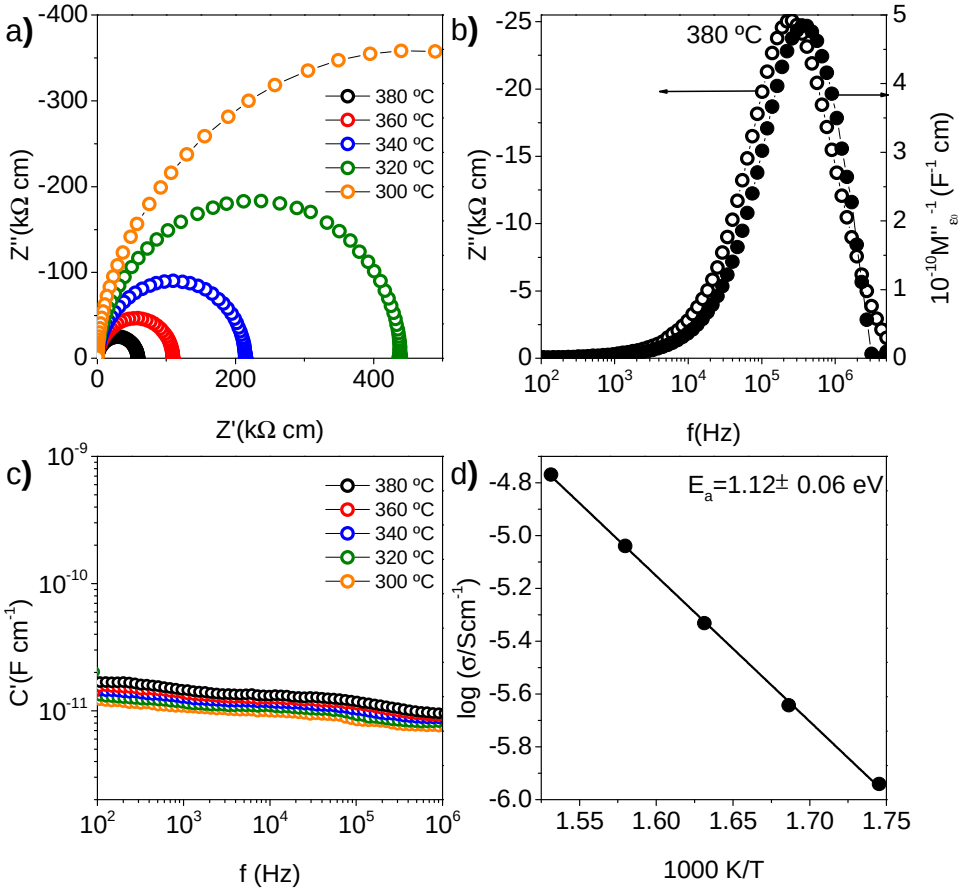

Figure 4. 14. a) Impedance complex plane plots, b) Z″/M″ spectroscopic plots at 380 ºC, c) C′ versus frequency and d) bulk Arrhenius plot for the sample with x = 0.02 composition obtained after milling for 6 h and sintering at 825 ºC.

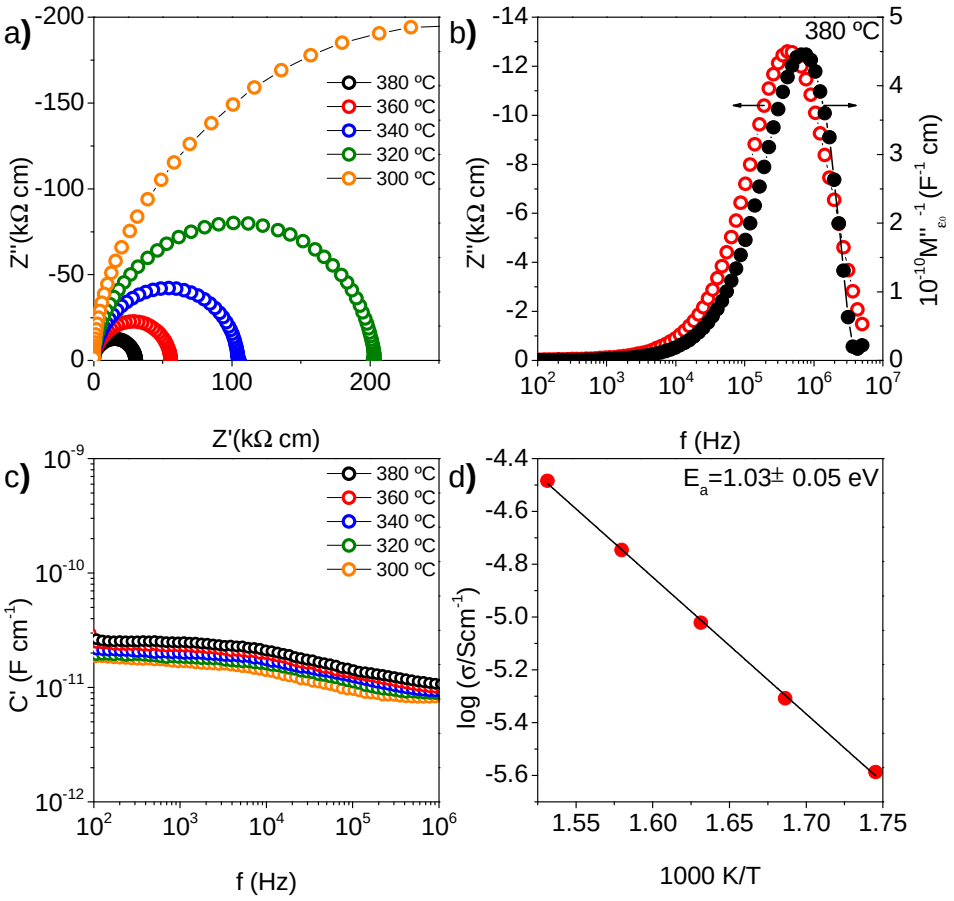

Figure 4. 15. a) Impedance complex plane plots, b) Z″/M″ spectroscopic plots at 380 ºC, c) C′ versus frequency and d) bulk Arrhenius plot for the sample with nominal x = 0.05 composition obtained after milling for 6 h and sintering at 825 ºC.

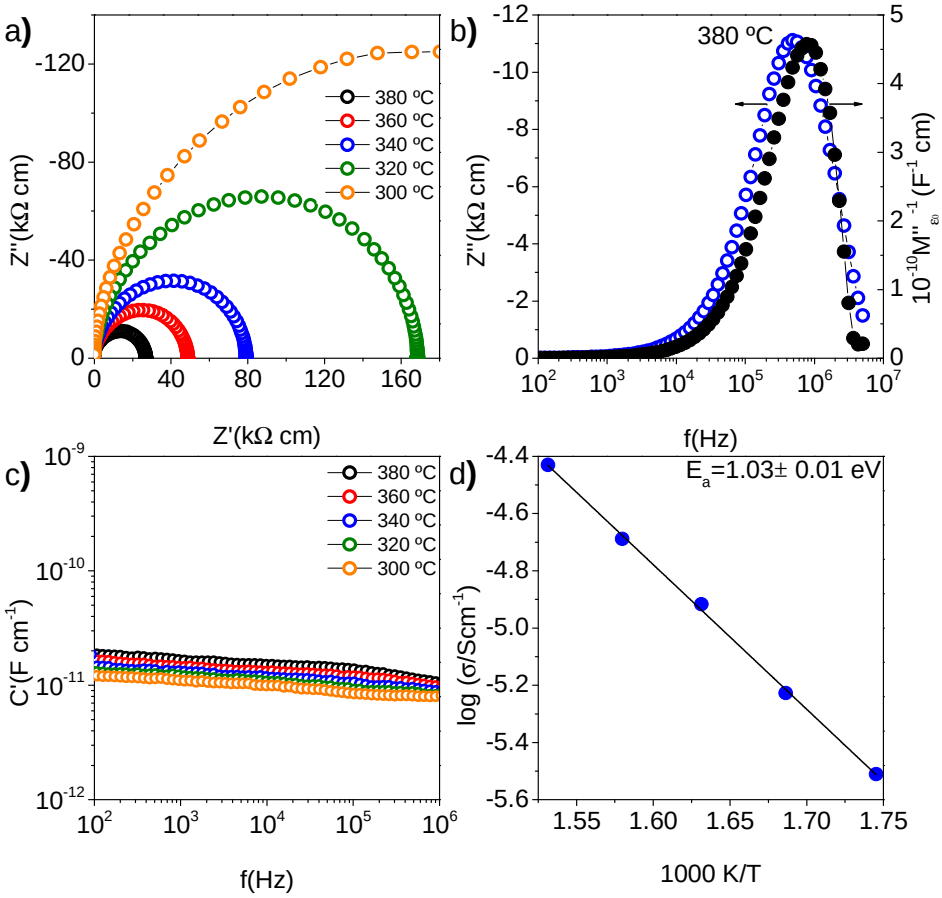

Figure 4. 16. a) Impedance complex plane plots, b) Z″/M″ spectroscopic plots at 380 ºC, c) C′ versus frequency and d) bulk Arrhenius plot for the sample with nominal x = 0.07 composition obtained after milling for 6 h and sintering at 825 ºC.

The resistivity values of the samples, obtained from the intercept on the real Z′ axes of the complex plane plots at different temperatures, in conventional Arrhenius format (equation (3.16)) are presented individually in Figures 4. 14 d), 4. 15 d) and 4. 16 d) for the three samples. A linear relationship between the conductivity and the inverse of

temperature is evidenced in every case. For comparison purposes, Figure 4. 17 shows the bulk conductivity data for the three samples of the $Bi_{1-x}Yb_xFeO_3$ system in conventional Arrhenius format. The activation energy for conduction for the sample x = 0.02 is 1.12 eV, and 1.03 eV for the samples with nominal x = 0.05 and x = 0.07 compositions. Although the activation energies are identical for these two last samples, a small increase in the conductivity for the sample with nominal x = 0.07 composition is observed. It may be attributed to the presence of a slightly higher amount of secondary phase as compared with the sample with nominal x = 0.05 composition. It is worth pointing out that the conductivity values for all the samples are small and in good agreement with the results previously reported for stoichiometric $BiFeO_3$ and $Bi_{1-x}La_xFeO_3$ samples prepared by mechanosynthesis [5, 7, 24]. This is an indication that there are no other significant sources of conductivity, such as mixed valence of Fe/Fe^{2+} associated with possible oxygen non-stoichiometry, overcoming one of the major issues related to the synthesis of $BiFeO_3$ and that are slowing down its implementation in devices.

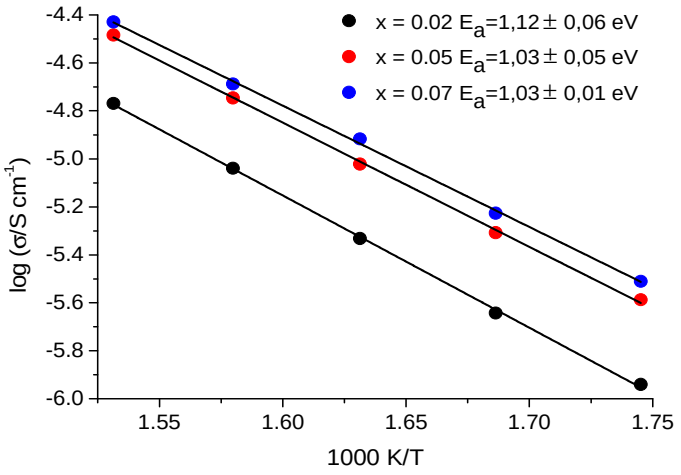

Figure 4. 17. Bulk conductivity data for $Bi_{1-x}Yb_xFeO_3$.

Impedance measurements under different oxygen partial pressures were performed in order to study the conduction mechanism. Figure 4. 18 shows the impedance complex-plane plots at 380 °C in nitrogen, air and oxygen for the $Bi_{1-x}Yb_xFeO_3$ samples of different compositions.

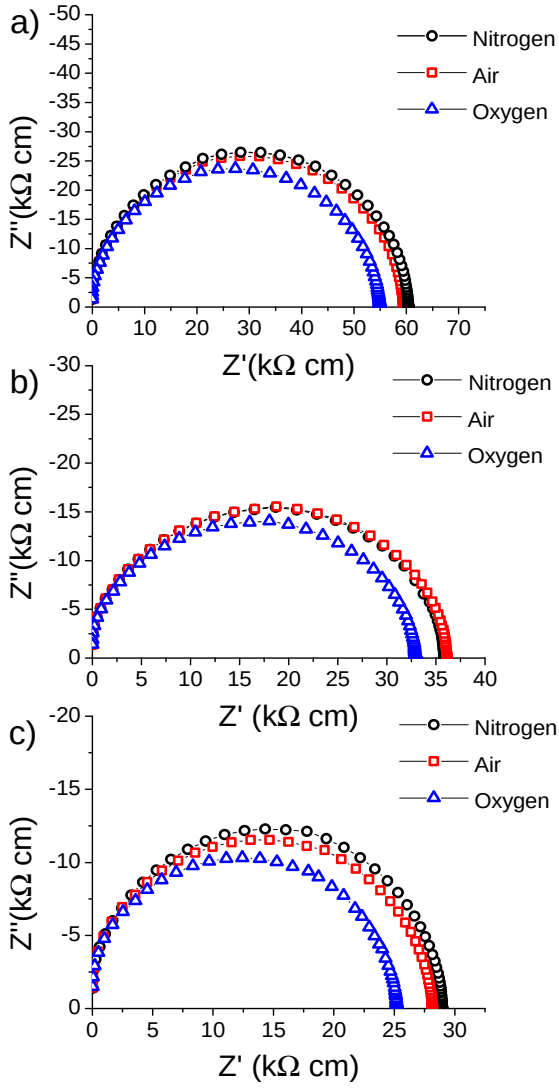

Figure 4. 18. Impedance complex-plane plots at 380 °C in nitrogen, air and oxygen for the $Bi_{1-x}Yb_xFeO_3$ samples: a) x = 0.02 composition, b) nominal x =0.05 and c) nominal x = 0.07 compositions.

Although the changes in conductivity with the oxygen content are small, specifically for the samples x = 0.02 and nominal x = 0.05 compositions, a tendency is observed about a possible p-type conduction mechanism. It may indicate that conduction is almost intrinsic but slightly dominated by holes. This means that samples can pick up O_2 by the nominal mechanism:

$$2V_O^{\bullet\bullet} + O_2 \rightarrow 2O_O^x + 4h^{\bullet} \quad (4.1)$$

And, therefore, the conductivity increases with increasing the oxygen partial pressure. It has been proposed that the holes can be associated with Fe as Fe^{4+} ions in the sample surface [7, 25]:

$$2V_O^{\bullet\bullet} + O_2 + 4Fe_{Fe}^x \rightarrow 2O_O^x + 4Fe_{Fe}^{\bullet} \quad (4.2)$$

Another possibility is that underbonded surface oxide ions may ionise, resulting in O^- ions that become the source of holes [7, 26, 27]. Nevertheless, further investigations are needed to clarify the origin of the holes.

4.4.8. Magnetic properties

Detailed magnetic characterisation of the $Bi_{1-x}Yb_xFeO_3$ samples is hampered by the presence of the ytterbium-rich impurity phase, which adds an unknown contribution to the data collected from the samples with nominal x = 0.05 and x = 0.07 compositions. Magnetisation-field data collected at 300 K (Figure 4. 19 a) and Table 4. 3) show a nearly linear field-dependent magnetization and do not saturate at this temperature at the maximum field applied, as it has been also observed for bulk $BiFeO_3$ and related compounds [7, 28, 29], and confirm the antiferromagnetic nature of the samples. Moreover, the samples show only a modest change to the weak ferromagnetic behaviour on ytterbium substitution. The

magnetisation-field data collected at 5 K (Figure 4. 19 b) and Table 4. 3) show increased remnant magnetizations (M_r) compared to their behaviour at 300 K, and that there is a significant increase in value with increasing ytterbium content of samples. Given the presence of the secondary ytterbium rich phases in the x = 0.05 and x = 0.07 samples, the increase in low temperature of the M_r values cannot be definitively attributed to the majority phases.

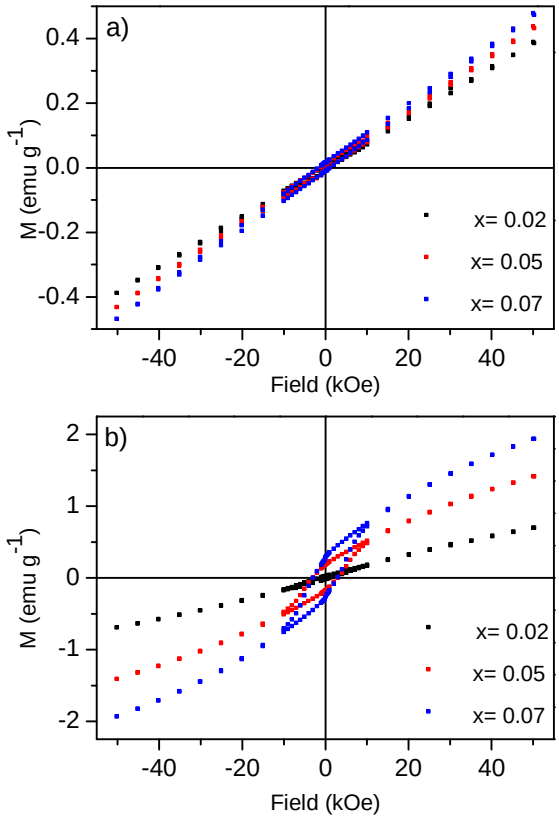

Figure 4. 19. Magnetisation data collected at a) 300 K and b) 5 K as a function of the applied field for the samples of $Bi_{1-x}Yb_xFeO_3$ obtained after milling for 6 h and sintered at 825 °C.

Table 4. 3. Coercive field (H_C), remnant magnetization (M_r) and 5 Tesla magnetization (M_{5T}) extracted from magnetisation data collected at 300 K and 5 K as a function of the applied field from samples of $Bi_{1-x}Yb_xFeO_3$ obtained after milling for 6 h and sintering at 825 ºC.

Temperature	300 K			5 K		
Nominal composition	x = 0.02	x = 0.05	x = 0.07	x = 0.02	x = 0.05	x = 0.07
H_c (Oe)	916	1091	1375	1277	3036	2917
M_r (emu g^{-1})	0.022	0.0028	0.0059	0.113	0.465	0.736
M_{5T} (emu g^{-1})	0.3892	0.4381	0.4789	0.701	1.415	1.936

4.5. CONCLUSIONS

Ytterbium-substituted $BiFeO_3$ samples have been prepared for the first time by mechanosynthesis followed by sintering and have been deeply characterized. In contrast to previous studies [1-3], XRD patterns and DSC data show that the ytterbium solubility in the rhombohedral R3c $Bi_{1-x}Yb_xFeO_3$ system is limited to approximately x = 0.03. This suggests that the reports of high Yb solubility are due to loss of Bi under alternative synthesis methods. DSC data confirm the multiferroic behaviour of the samples, showing two phase transition temperatures, related to T_N (ferromagnetic-paramagnetic transition) and T_C (ferroelectric-paraelectric transition). The crystal structures of the samples were analysed by the Rietveld method. The sample with x = 0.02 composition was observed to be essentially phase-pure, maintaining the R3c space group of the parent compound $BiFeO_3$. On the other hand, the samples with nominal x = 0.05 and x = 0.07 compositions present the main R3c phase together with ytterbium enriched secondary phases, which cannot be indexed or quantified due to their small amount. Raman spectroscopy also confirms the R3c main phase of all the samples. Temperature-dependent XRD patterns confirmed the Curie temperatures observed by DSC, showing that all samples exhibit rhombohedral R3c to orthorrombic Pnma phase

transitions. Moreover, EDX analysis indicated that the initial nominal stoichiometry has not been modified during the preparation of the samples. The UV-Vis measurements suggested their potential use in photocatalytic applications. Finally, impedance and magnetic measurements showed that samples present low conductivity values with a possible p-type conduction mechanism and an antiferromagnetic behaviour at room temperature with an unknown contribution of the secondary ytterbium-rich phases.

4.6. REFERENCES

[1] Yan Z., Wang K.F., Qu J.F., Wang Y., Song Z.T. and Feng S.L., *Processing and properties of Yb-doped $BiFeO_3$ ceramics*. Applied Physics Letters, **2007**, 91 (8).

[2] Wu C.F., Wei J. and Kong F.S., *Effect of rare earth dopants on the morphologies and photocatalytic activities of $BiFeO_3$ microcrystallites*. Journal of Materials Science-Materials in Electronics, **2013**, 24 (5), p. 1530-1535.

[3] Thakuria P. and Joy P.A., *High room temperature ferromagnetic moment of Ho substituted nanocrystalline $BiFeO_3$*. Applied Physics Letters, **2010**, 97 (16).

[4] Kuz O., Prots Y. and Vasylechko L., *Phase and Crystal Structure Behaviour of $Bi_{1-x}R_xFeO_3$ (R = Er, Tm, Yb)*. Oxide Materials for Electronic Engineering - Fabrication, Properties and Applications, **2013**, 200, p. 100-107.

[5] Perejon A., Maso N., West A.R., Sanchez-Jimenez P.E., Poyato R., Criado J.M. and Perez-Maqueda L.A., *Electrical Properties of*

Stoichiometric $BiFeO_3$ Prepared by Mechanosynthesis with Either Conventional or Spark Plasma Sintering. Journal of the American Ceramic Society, **2013**, 96 (4), p. 1220-1227.

[6] Perejon A., Murafa N., Sanchez-Jimenez P.E., Criado J.M., Subrt J., Dianez M.J. and Perez-Maqueda L.A., *Direct mechanosynthesis of pure $BiFeO_3$ perovskite nanoparticles: reaction mechanism*. Journal of Materials Chemistry C, **2013**, 1 (22), p. 3551-3562.

[7] Perejon A., Sanchez-Jimenez P.E., Perez-Maqueda L.A., Criado J.M., de Paz J.R., Saez-Puche R., Maso N. and West A.R., *Single phase, electrically insulating, multiferroic La-substituted $BiFeO_3$ prepared by mechanosynthesis*. Journal of Materials Chemistry C, **2014**, 2 (39), p. 8398-8411.

[8] Karimi S., Reaney I.M., Han Y., Pokorny J. and Sterianou I., *Crystal chemistry and domain structure of rare-earth doped $BiFeO_3$ ceramics*. Journal of Materials Science, **2009**, 44 (19), p. 5102-5112.

[9] Catalan G. and Scott J.F., *Physics and Applications of Bismuth Ferrite*. Advanced Materials, **2009**, 21 (24), p. 2463-2485.

[10] Catalan G., Sardar K., Church N.S., Scott J.F., Harrison R.J. and Redfern S.A.T., *Effect of chemical substitution on the Néel temperature of multiferroic $Bi_{1-x}Ca_xFeO_3$*. Physical Review B, **2009**, 79 (21), p. 212415.

[11] Goldschmidt V.M., *Die Gesetze der Krystallochemie*. Naturwissenschaften, **1926**, 14 (21), p. 477-485.

[12] Zhang X., Sui Y., Wang X., Wang Y. and Wang Z., *Effect of Eu substitution on the crystal structure and multiferroic properties of*

$BiFeO_3$. Journal of Alloys and Compounds, **2010**, 507 (1), p. 157-161.

[13] Li J.B., Rao G.H., Xiao Y., Liang J.K., Luo J., Liu G.Y. and Chen J.R., *Structural evolution and physical properties of $Bi_{1-x}Gd_xFeO_3$ ceramics*. Acta Materialia, **2010**, 58 (10), p. 3701-3708.

[14] Shannon R.D., *Revised effective ionic radii and systematic studies of interatomic distances in halides and chalcogenides*. Acta Crystallographica, Section A (Crystal Physics, Diffraction, Theoretical and General Crystallography), **1976**, A32, p. 751-767.

[15] Chen X.M., Wang Y.P., Yang Y., Yuan G.L., Yin J. and Liu Z.G., *Structure, ferroelectricity and piezoelectricity evolutions of $Bi_{1-x}Sm_xFeO_3$ at various temperatures*. Solid State Communications, **2012**, 152 (6), p. 497-500.

[16] Palai R., Katiyar R., Schmid H., Tissot P., Clark S., Robertson J., Redfern S., Catalan G. and Scott J., *β phase and γ-β metal-insulator transition in multiferroic $BiFeO_3$*. Physical Review B, **2008**, 77 (1), p. 014110.

[17] Yang Y., Yu-Long L., Ke Z., Li-Yan Z., Shu-Yuan M., Jie L. and Yi-Jian J., *Structural properties of $Bi_{1-x}La_xFeO_3$ studied by micro-Raman scattering*. Chinese Physics B, **2010**, 19 (3), p. 037802.

[18] Hu W., Chen Y., Yuan H., Li G., Qiao Y., Qin Y. and Feng S., *Structure, Magnetic, and Ferroelectric Properties of $Bi_{1-x}Gd_xFeO_3$ Nanoparticles*. Journal of Physical Chemistry C, **2011**, 115 (18), p. 8869-8875.

[19] Dai H.Y., Chen Z.P., Li T. and Li Y., *Microstructure and properties of Sm-substituted $BiFeO_3$ ceramics*. Journal of Rare Earths, **2012**, 30 (11), p. 1123-1128.

[20] Kim Y.I., Atherton S.J., Brigham E.S. and Mallouk T.E., *Sensitized layered metal-oxide semiconductor particles for photochemical hydrogen evolution from nonsacrifical electron-donors*. Journal of Physical Chemistry, **1993**, 97 (45), p. 11802-11810.

[21] Hauser A.J., Zhang J., Mier L., Ricciardo R.A., Woodward P.M., Gustafson T.L., Brillson L.J. and Yang F.Y., *Characterization of electronic structure and defect states of thin epitaxial $BiFeO_3$ films by UV-visible absorption and cathodoluminescence spectroscopies*. Applied Physics Letters, **2008**, 92 (22), p. 222901.

[22] Gao F., Chen X.Y., Yin K.B., Dong S., Ren Z.F., Yuan F., Yu T., Zou Z. and Liu J.M., *Visible-light photocatalytic properties of weak magnetic $BiFeO_3$ nanoparticles*. Advanced Materials, **2007**, 19 (19), p. 2889-2892.

[23] Li S., Lin Y.H., Zhang B.P., Nan C.W. and Wang Y., *Photocatalytic and magnetic behaviors observed in nanostructured $BiFeO_3$ particles*. Journal of Applied Physics, **2009**, 105 (5), p. 056105.

[24] Perejon A., Sanchez-Jimenez P.E., Poyato R., Maso N., West A.R., Criado J.M. and Perez-Maqueda L.A., *Preparation of phase pure, dense fine grained ceramics by conventional and spark plasma sintering of La-substituted $BiFeO_3$ nanoparticles*. Journal of the European Ceramic Society, **2015**, 35 (8), p. 2283-2293.

[25] Masó N. and West A.R., *Electrical Properties of Ca-Doped $BiFeO_3$ Ceramics: From p-Type Semiconduction to Oxide-Ion Conduction*. Chemistry of Materials, **2012**, 24 (11), p. 2127-2132.

[26] Ren P., Maso N., Liu Y., Ma L., Fan H. and West A.R., *Mixed oxide ion and proton conduction and p-type semiconduction in $BaTi_{0.98}Ca_{0.02}O_{2.98}$ ceramics*. Journal of Materials Chemistry C, **2013**, 1 (13), p. 2426-2432.

[27] Gil Escrig L., Prades M., Beltrán H., Cordoncillo E., Masó N. and West A.R., *Voltage-Dependent Bulk Resistivity of $SrTiO_3$:Mg Ceramics*. Journal of the American Ceramic Society, **2014**, 97 (9), p. 2815-2824.

[28] Da Silva K.L., Menzel D., Feldhoff A., Kübel C., Bruns M., Paesano A., Düvel A., Wilkening M., Ghafari M., Hahn H., Litterst F.J., Heitjans P., Becker K.D. and Šepelák V., *Mechanosynthesized $BiFeO_3$ nanoparticles with highly reactive surface and enhanced magnetization*. Journal of Physical Chemistry C, **2011**, 115 (15), p. 7209-7217.

[29] Freitas V.F., Grande H.L.C., de Medeiros S.N., Santos I.A., Cótica L.F. and Coelho A.A., *Structural, microstructural and magnetic investigations in high-energy ball milled $BiFeO_3$ and $Bi_{0.95}Eu_{0.05}FeO_3$ powders*. Journal of Alloys and Compounds, **2008**, 461 (1–2), p. 48-52.

5. MECHANOCHEMISTRY OF THE $Bi_{1-x}Sm_xFeO_3$ SYSTEM

5.1. INTRODUCTION

Bismuth substitution by samarium, $Bi_{1-x}Sm_xFeO_3$, remarkably enhances the physical properties of bulk $BiFeO_3$ ceramics prepared by several different synthesis methods, as reported by several authors [1-5]. For instance, the synthesis by rapid liquid-phase sintering gives rise to ceramics with large piezoelectric coefficient and high remnant polarization [1]. An improvement in the ferroelectric polarization for a sample of composition x = 0.125 as well as an enhancement in the magnetic properties have also been observed using this method of synthesis [6, 7]. Conventional and modified solid-state reaction synthesis have been also reported to improve magnetic [2-4], dielectric [8] and pyroelectric [1] properties of the bulk ceramics. A combination of mechanical activation with solid state reaction also gives rise to $Bi_{1-x}Sm_xFeO_3$ ceramics with enhanced properties [5, 9, 10]. Additionally, several chemical routes such as sol-gel [11-15], tartaric acid modified sol-gel [16], and other wet chemical methods [17] have been employed for this purpose. However, there is no consensus regarding the crystal structure and physical properties of the bulk ceramics as a function of the samarium content. On the one hand, Karimi et al. reported that the polar R3c structure of $BiFeO_3$ is retained for samarium content in the range $0 \leq x \leq 0.15$ [4], but in other works it has been concluded that the main phase for x = 0.15 can be

indexed in the Pbam space group [3, 18, 19]. On the other hand, Khodabakhsh et al. consider that at this composition, two phases, R3c and Pbnm, coexist [14]. Moreover, discrepancies are not only found in the crystal structures at different compositions but also in the phase transition temperatures. Different phase transition temperatures are reported for samples with the same composition. These discrepancies may be due to the different synthesis methods employed, which play an extremely important role in the resulting properties of the materials [20], as it has been pointed out in Section 1.2. Additionally, many of them normally give rise to routine impurities, mainly $Bi_2Fe_4O_9$ and $Bi_{25}FeO_{39}$ [1, 2, 8, 19, 21, 22].

For these reasons, it is extremely hard to get a true view of the effects of samarium substitution on the crystal structure and the physical behaviour of $BiFeO_3$ unencumbered by the presence of secondary phases or compositional inhomogeneity. Alternative methods for the preparation of the $Bi_{1-x}Sm_xFeO_3$ system are mechanochemical approaches. To the best of our knowledge, direct mechanosynthesis has never been employed for the preparation of this system. Mechanosynthesis appears to be well suited to addressing the synthetic challenges associated with the preparation of $BiFeO_3$ and related compounds, since pure and highly insulating compounds have been previously reported [23-26].

5.2. OBJECTIVES

All in all, the objective of this chapter is the preparation of high quality samples of the $Bi_{1-x}Sm_xFeO_3$ system, in terms of homogeneity and phase-purity by mechanosynthesis followed by sintering in a wide range of compositions, as well as their characterization by an exhaustive analysis of the crystal structure, microstructure, optical, electrical and magnetic

properties by XRD, Raman spectroscopy, DSC, X-ray thermodiffraction, dielectric thermal analysis (DEA), electron microscopy techniques, UV-visible spectroscopy, impedance spectroscopy and magnetic measurements. Based on the data collected from the Rietveld refinements, DSC, X-Ray thermodiffraction, DEA and TEM, a tentative phase diagram is proposed as well.

5.3. EXPERIMENTAL

Powders of six different compositions of the general formula $Bi_{1-x}Sm_xFeO_3$ (x = 0.05, 0.10, 0.125, 0.15, 0.175 and 0.20) were prepared by mechanosynthesis in the planetary Micro Mill PULVERISETTE 7 Premium Line according to the procedure detailed in Section 3.2.1 (Chapter 3). The optimum milling time in order to induce the reactions of the pristine oxides depends on the composition of the products and it is listed in Table 5. 1.

Table 5. 1. Optimum milling times associated with each composition.

$Bi_{1-x}Sm_xFeO_3$	Milling time (h)
x = 0.05	5
x = 0.10	6
$0.125 \leq x \leq 0.20$	8

The powders were pressed into the shape of pellets and were conventionally sintered at 900 ^oC in air. TEM measurements were carried out in the 200 kV TEM Philips CM 200 microscope described in Section 3.3.5 (Chapter 3).

5.4. RESULTS AND DISCCUSION

5.4.1. Mechanosynthesis and sintering

The reaction of the pristine oxides to form products with the general formula $Bi_{1-x}Sm_xFeO_3$ was followed by X-ray diffraction. As an example, XRD patterns at periodic intervals of the milling process are shown in Figure 5. 1 for x = 0.05 and x = 0.10 compositions. The same behaviour can be clearly observed for both compositions as milling proceeds.

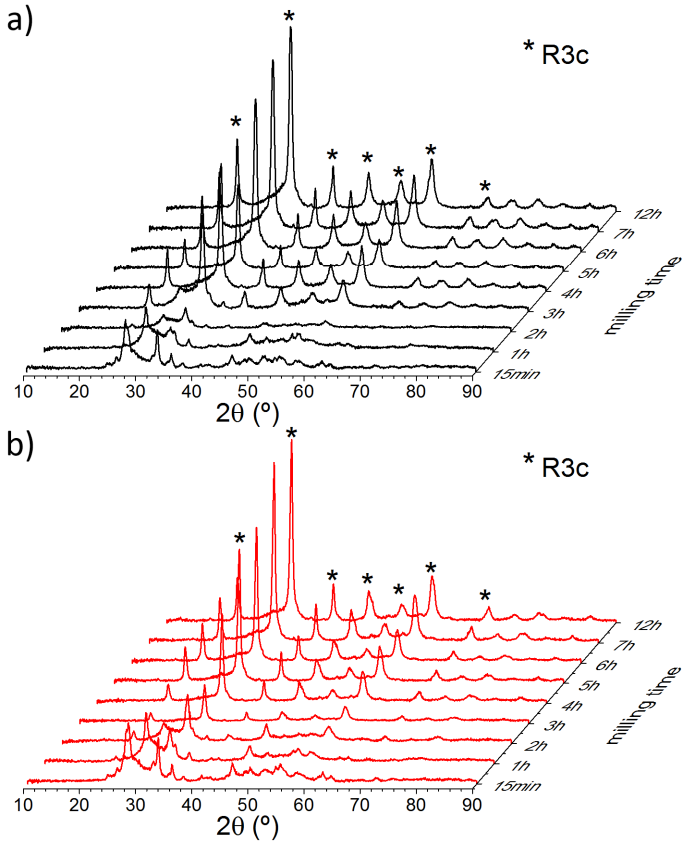

Figure 5. 1. XRD patterns as a function of milling time for the samples: a) $Bi_{0.95}Sm_{0.05}FeO_3$ and b) $Bi_{0.90}Sm_{0.10}FeO_3$.

The starting oxides suffer an initial amorphization during the milling treatment, as inferred from the comparison of the XRD data registered after 15 min and 2 h of milling of Figure 5. 1. It is followed by the crystallization of the new phases as grinding continues up to 5-6 h, approximately. Further mechanical treatments did not produce modifications in the powders of any composition, as it is observed from XRD measurements after 12 h of milling.

To sum up, Figure 5. 2 depicts the X-ray powder diffraction data collected from the $Bi_{1-x}Sm_xFeO_3$ samples prior to sintering, along with the optimum milling time required to carry out the full reaction of starting oxides. It can be seen that the milling time required to complete the reaction increased with samarium content. The broad diffraction peaks observed in Figure 5. 2 are attributable to the nanometric crystallite size of the samples, which make it hard to extract detailed crystallographic information. Nevertheless, it is clear that the diffraction profile of the x = 0.2 sample is significantly different from those of the other compositions.

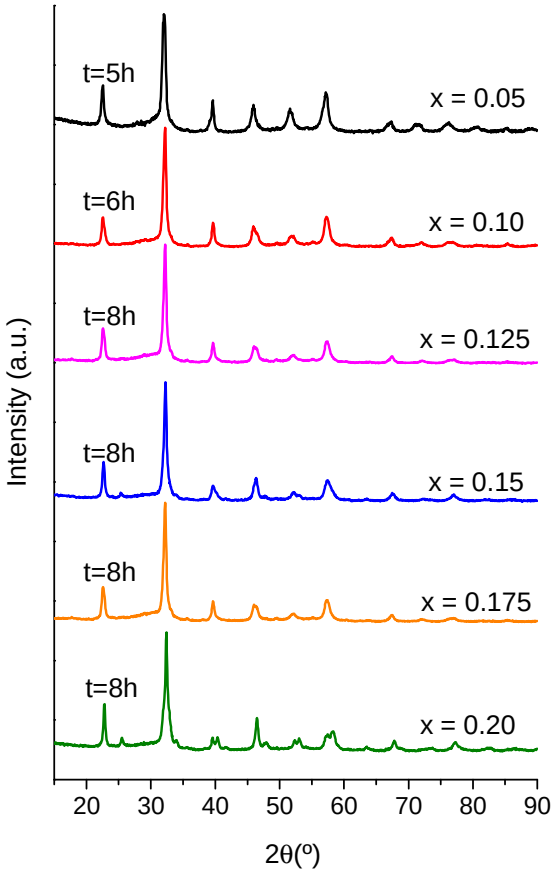

Figure 5. 2. XRD patterns of powders of composition $Bi_{1-x}Sm_xFeO_3$ obtained after milling suitable stoichiometric ratios of the single oxides in oxygen (7 bar) for the indicated milling times.

Conventionally sintered samples were employed to obtain more detailed crystallographic information since the crystallinity of the samples increased after the sintering treatment. Figure 5. 3 shows expanded sections of the XRD data collected, in the range $20^o < 2\theta < 45^o$, for $Bi_{1-x}Sm_xFeO_3$ samples after sintering at 900 ^oC. The achieved relative pellet densities for each composition are shown in Table 5. 2.

Table 5. 2. Relative pellet density associated with each composition.

$Bi_{1-x}Sm_xFeO_3$	Relative density (%)
x = 0.05	97
x = 0.10	96
x = 0.125	95
x = 0.15	93
x = 0.175	94
x = 0.20	95

Close examination reveals dramatic changes in the powder diffraction data as a function of samarium content in Figure 5. 3. The x = 0.05 and x = 0.10 samples can be indexed using a rhombohedral unit cell (space group R3c), typical of $BiFeO_3$ at room temperature. As the samarium content increases above x = 0.125 there are significant changes in the XRD patterns. For example, for x = 0.15 and x = 0.175 compositions the peak at 22° splits into two peaks while the double peak at 32° merges. For x = 0.20 composition, the double peak at 22° merges again and new peaks appear at about 25.4°, 31.8°, 32.8° and 33.8°. Hence, it is clear that the data can no longer be indexed by a single rhombohedral unit cell, indicating that a change in structure has occurred.

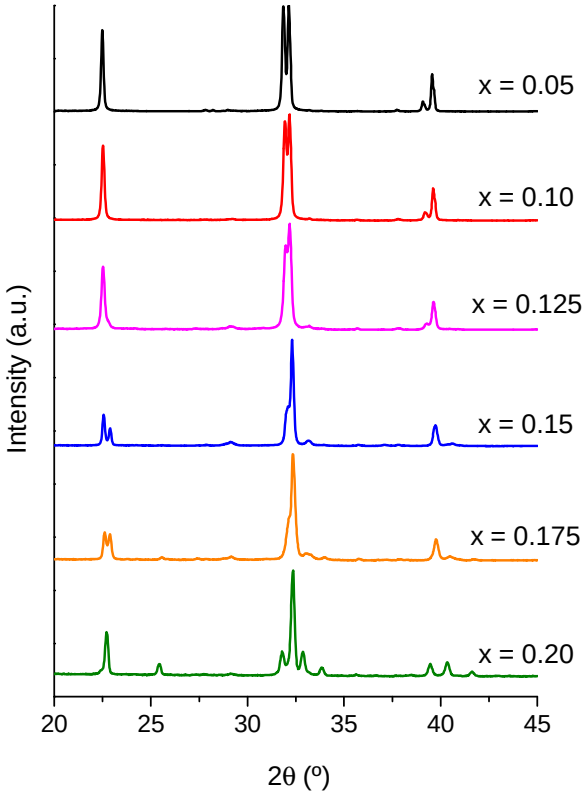

Figure 5. 3. XRD patterns of the mechanosynthesized samples of composition $Bi_{1-x}Sm_xFeO_3$ registered after sintering at 900 ºC.

5.4.2. Structural characterization

Detailed crystallographic characterization of the $Bi_{1-x}Sm_xFeO_3$ system was obtained by the Rietveld method. Figures 5. 4 and 5. 5 show the Rietveld refinements of the x = 0.05 and x = 0.10 samples, respectively.

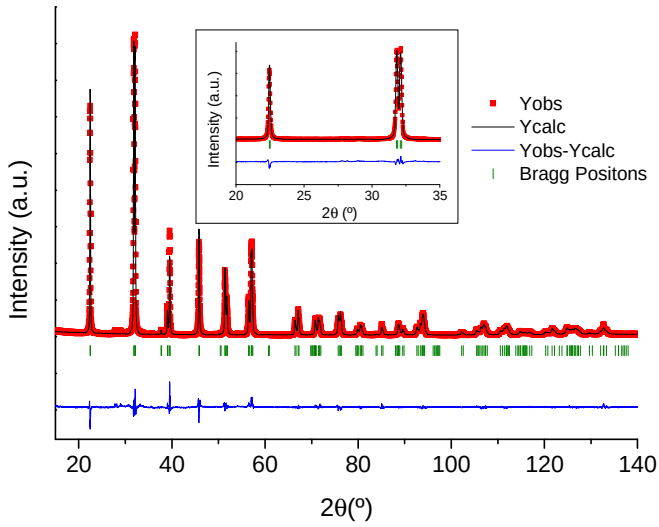

Figure 5. 4. XRD pattern of $Bi_{0.95}Sm_{0.05}FeO_3$ obtained after 5 h milling and sintering at 900 ºC (dots). The solid line corresponds to the fit from the Rietveld refinement. Bragg reflections for R3c space group are indicated by sticks. The inset shows an expanded section of the diffractogram in the 2θ region from 20º to 35º.

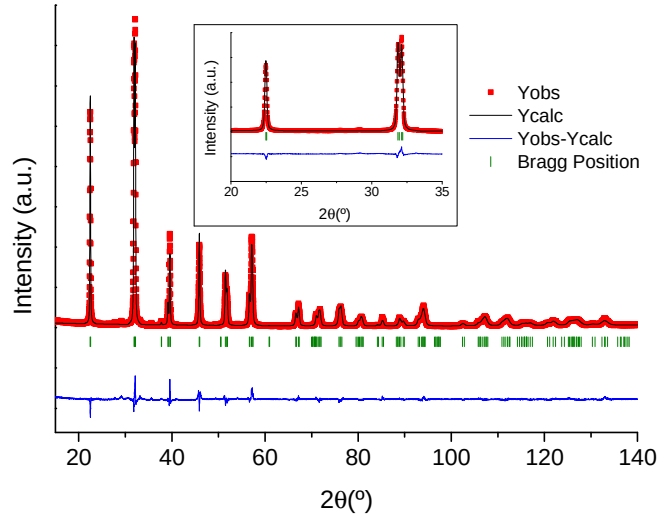

Figure 5. 5. XRD pattern of $Bi_{0.90}Sm_{0.10}FeO_3$ obtained after 6 h milling and sintering at 900 ºC (dots). The solid line corresponds to the fit from the Rietveld refinement. Bragg reflections for R3c space group are indicated by sticks. The inset shows an expanded section of the diffractogram in the 2θ region from 20º to 35º.

The XRD data of both samples (x = 0.05 and x = 0.10) can be successfully fitted using a rhombohedral R3c structure with good reliability factors (Table 5. 3). Both samples appear to be phase-pure, although very small features can be observed that may correspond to extremely small amounts of secondary phases that, therefore, cannot be identified and quantified.

Attempts were made to index the diffraction data from x ≥ 0.125 samples using a number of different unit cells and space groups, according with those proposed in the literature for the $Bi_{1-x}Sm_xFeO_3$ system. For the x = 0.15 composition, the following space groups were tested: R3c, Pnma, Pbam, Amm2, C221, Imma, P2mm, $Pmc2_1$, $Pn2_1a$. Very high reliability factors were obtained for some space groups since they do not account for all the observed peaks in the diffractogram. Nevertheless, this sample could be readily indexed using an orthorhombic unit cell, in the centrosymmetric space group Pbam (Figure 5. 6). Refinement of a crystallographic model constructed in this unit cell gave the best fit to the data (Table 5. 4) indicating that the XRD pattern of $Bi_{0.85}Sm_{0.15}FeO_3$ does not present significant peaks corresponding to secondary phases. This is in agreement with results previously reported for this samarium composition [3, 18], although other authors have suggested the presence of a mixture of R3c+Pbnm phases [14]. These discrepancies may be due to the methods of synthesis employed, which normally give rise to impurities and bismuth deficiency, in contrast to the mechanochemical approach. The same strategy was employed to index and refine the diffraction data from the x = 0.20 sample (Figure 5. 7). Thus, the space groups $Pn2_1a$, R3c, Pbam and Pnma were tested, as well as a possible mixture of Pnma+Pbam. The best results were obtained by using an orthorhombic unit cell in space group Pnma (Table 5. 4).

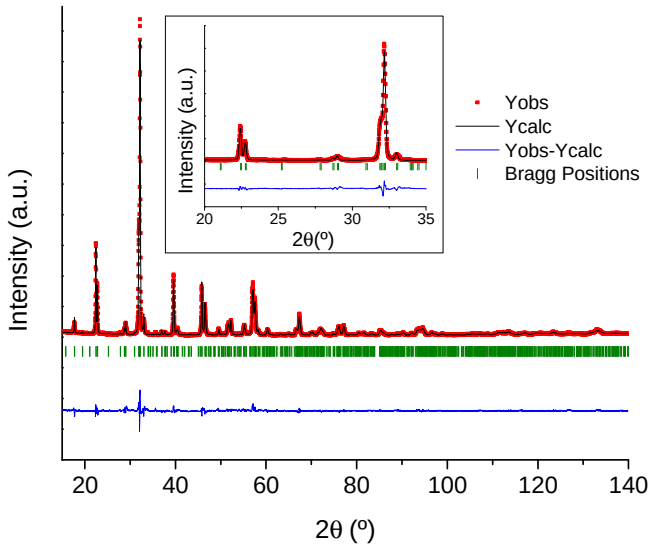

Figure 5. 6. XRD pattern of $Bi_{0.85}Sm_{0.15}FeO_3$ obtained after 8 h milling and sintering at 900 ºC (dots). The solid line corresponds to the fit from the Rietveld refinement. Bragg reflections for Pbam space group are indicated by sticks. The inset shows an expanded section of the diffractogram in the 2θ region from 20º to 35º.

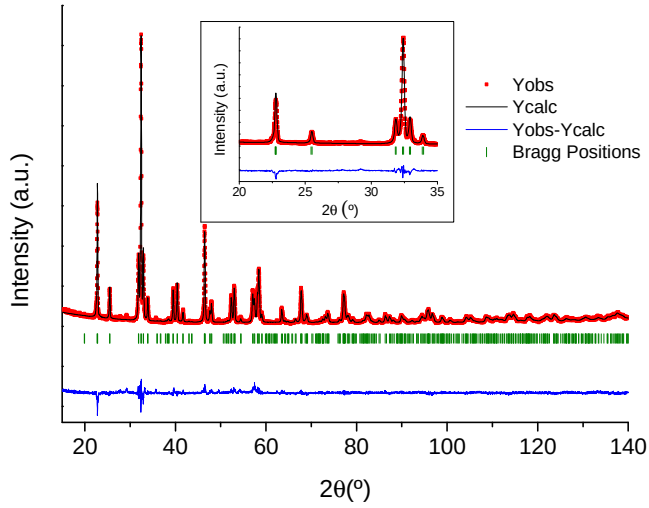

Figure 5. 7. XRD pattern of $Bi_{0.80}Sm_{0.20}FeO_3$ obtained after 8 h milling and sintering at 900 ºC (dots). The solid line corresponds to the fit from the Rietveld refinement. Bragg reflections for Pnma space group are indicated by sticks. The inset shows an expanded section of the diffractogram in the 2θ region from 20º to 35º.

The diffraction data collected from the x = 0.125 and x = 0.175 samples could not be indexed by single unit cells. However, these data could be fitted well using a structural model containing two phases. As shown in Figure 5. 8 and Table 5. 3, fits to the data from the x = 0.125 sample demonstrate that it is a mixture of an R3c phase (72%) and a Pbam phase (28%). This indicates that a phase transition takes place from $x \geq 0.125$. Similarly, fits to the diffraction data collected from the x = 0.175 composition demonstrate that it is a mixture of a Pbam phase (74%) and Pnma phase (26%) (Figure 5. 9, Table 5. 4). The coexistence of several phases with the same composition has been widely observed by other authors in Sm substituted $BiFeO_3$ ceramics [5, 10, 14].

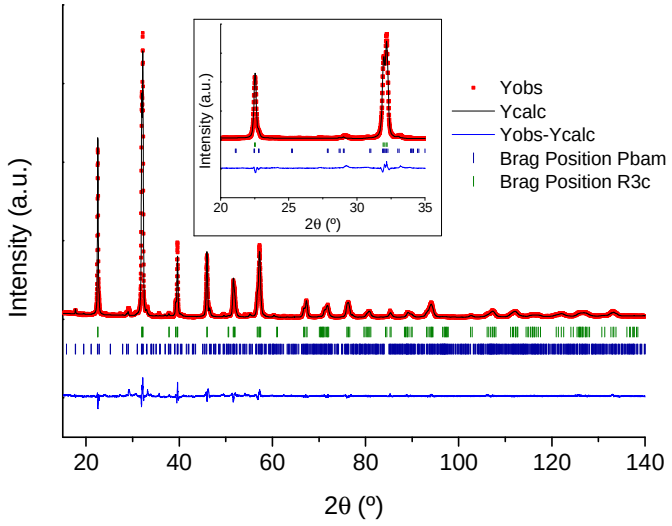

Figure 5. 8. XRD pattern of $Bi_{0.875}Sm_{0.125}FeO_3$ obtained after 8 h milling and sintering at 900 ºC (dots). The solid line corresponds to the fit from the Rietveld refinement. Bragg reflections for R3c and Pbam space groups are indicated by sticks. The inset shows an expanded section of the diffractogram in the 2θ region from 20º to 35º.

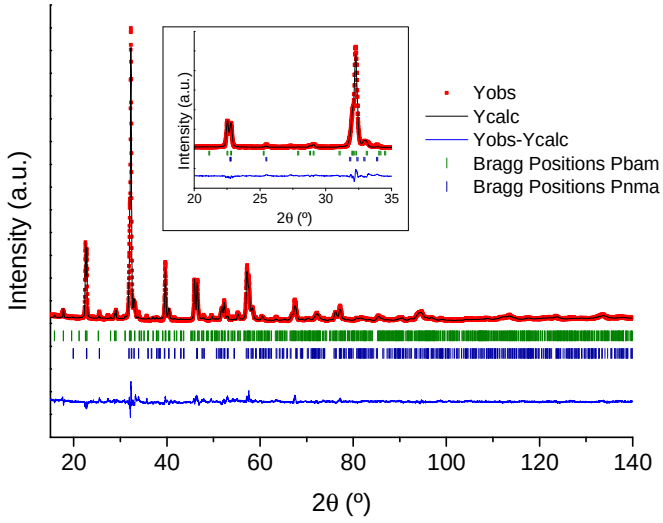

Figure 5. 9. XRD pattern of $Bi_{0.825}Sm_{0.175}FeO_3$ obtained after 8 h milling and sintering at 900 ºC (dots). The solid line corresponds to the fit from the Rietveld refinement. Bragg reflections for Pbam and Pnma space groups are indicated by sticks. The inset shows an expanded section of the diffractogram in the 2θ region from 20º to 35º.

Additionally, Table 5. 3 and Table 5. 4 list all the calculated parameters from the Rietveld analysis and the compositional dependence of the unit cell volume of the system $Bi_{1-x}Sm_xFeO_3$ with the amount of samarium. A considerable reduction of the unit cell volume is observed as the samarium content increases, which is related to both samarium substitution and the phase transitions.

Table 5. 3. Rietveld refinement and structural parameters obtained from the XRD patterns of the samples $Bi_{0.95}Sm_{0.05}FeO_3$, $Bi_{0.90}Sm_{0.10}FeO_3$ and $Bi_{0.875}Sm_{0.125}FeO_3$, sintered at 900 °C.

Sample	$Bi_{0.95}Sm_{0.05}FeO_3$	$Bi_{0.90}Sm_{0.10}FeO_3$	$Bi_{0.875}Sm_{0.125}FeO_3$	
Space group	R3c (100% w/w)	R3c (100% w/w)	R3c (72 ± 2% w/w)	Pbam (28 ± 2% w/w)
a (Å)	5.5742(1)	5.5695(1)	5.5655(10)	5.5887(21)
b (Å)	5.5742(2)	5.5695(1)	5.5655 (10)	11.2213(13)
c (Å)	13.8352(1)	13.7989(3)	13.7744(28)	7.8044(10)
Volume (Å^3)	372.283(3)	370.594(4)	369.493(2)	489.434(5)
Atomic positions				
Bi (1)	0.00, 0.00, 0.00	0.00, 0.00, 0.00	0.00, 0.00, 0.00	0.7197(3), 0.1242(4), 0.00
Bi (2)	-	-	-	0.7038(5), 0.1336(2), 0.50
Sm (1)	0.00, 0.00, 0.00	0.00, 0.00, 0.00	0.00, 0.00, 0.00	0.7197(1), 0.1242(2), 0.00
Sm (2)	-	-	-	0.7038(2), 0.1336(5), 0.50
Fe	0.00, 0.00, 0.2219(4)	0.00, 0.00, 0.2246(3)	0.00, 0.00, 0.2239(5)	0.2264(6), 0.11658(5),0.2375(4)
O (1)	0.4391(3), 0.0059(2), 0.9544(4)	0.4449(4), 0.0105(2), 0.9553(1)	0.4453(2), 0.0214(6), 0.9510(1)	0.2890(2), 0.1690(1), 0.00
O (2)	-	-	-	0.3190(3), 0.1090(4), 0.50
O (3)	-	-	-	0.0240(5), 0.2630(7), 0.2870(4)
O (4)	-	-	-	0.00, 0.50, 0.2050(3)
O (5)	-	-	-	0.00, 0.00, 0.2400(2)
Confidence factors				
R_{Bragg}	7.59	8.13	7.35	
R_{exp}	5.29	5.30	4.99	
R_{wp}	10.76	10.90	10.60	
χ^2	4.14	4.23	4.51	

Table 5. 4. Rietveld refinement and structural parameters obtained from the XRD patterns of the samples $Bi_{0.85}Sm_{0.15}FeO_3$, $Bi_{0.825}Sm_{0.175}FeO_3$ and $Bi_{0.80}Sm_{0.20}FeO_3$, sintered at 900 °C.

Sample	$Bi_{0.85}Sm_{0.15}FeO_3$	$Bi_{0.825}Sm_{0.175}FeO_3$		$Bi_{0.80}Sm_{0.20}FeO_3$
Space group	Pbam (100% w/w)	Pbam (74 ±1 % w/w)	Pnma (26 ±1 % w/w)	Pnma (100% w/w)
a (Å)	5.5887(1)	5.5792(2)	5.6216(2)	5.6216(1)
b (Å)	11.2208(3)	11.1887(4)	7.8141(5)	7.8141(2)
c (Å)	7.8039(2)	7.7985(3)	5.4429(2)	5.4429(1)
Volume (Å3)	489.434(3)	486.846(5)	239.098(6)	239.10(3)
Atomic positions				
Bi (1)	0.7163(2), 0.1232(1), 0.00	0.7209(6), 0.1245(4), 0.00	0.0255(2), 0.2500, 0.988(3)	0.0457(2), 0.25,0.9960(5)
Bi (2)	0.7017(5), 0.1341(4), 0.50	0.7053(3), 0.1343(2), 0.50	-	-
Sm (1)	0.7163(6), 0.1232(3), 0.00	0.7209(1), 0.1245(4), 0.00	0.0255(3), 0.2500, 0.9883(5)	0.0457(4), 0.25,0.9960(6)
Sm (2)	0.7017(2), 0.1341(1), 0.50	0.7053(3), 0.1343(6), 0.50	-	-
Fe	0.2344(5), 0.1177(4),0.2490(3)	0.2402(5), 0.1223(2),0.2567(3)	0.00, 0.00, 0.50(2)	0.00, 0.00,0.50(4)
O (1)	0.2448(3), 0.1836(2), 0.00	0.2286(7), 0.1936(3), 0.00	0.4853(3), 0.2500, 0.0764(4)	0.4817(1), 0.25,0.0889(3)
O (2)	0.3000(1), 0.1222(5), 0.50	0.3024(3), 0.1429(4), 0.50	0.2095(6), 0.5340(3), 0.2148(2)	0.2896(2), 0.0409(5),0.7128(6)
O (3)	0.0240(2), 0.2639(3),0.2243(4)	0.0240(2), 0.2662(1), 0.50	-	-
O (4)	0.00, 0.50, 0.1852(1)	0.00, 0.50, 0.1625(6)	-	-
O (5)	0.00, 0.00, 0.2209(5)	0.50, 0.00,0.2021(4)	-	-
Confidence factors				
R_{Bragg}	8.17	9.62		7.56
R_{exp}	4.76	5.60		5.97
R_{wp}	10.97	13.00		9.85
χ^2	5.31	5.38		2.72

According to Shannon, the ionic radii of Bi^{3+} and Sm^{3+} (in eightfold coordination) are 1.17 Å and 1.079 Å, respectively [27]. Hence, the tolerance factors, t, can be calculated according to equation (1.1). Table 5. 5 represents the tolerance factors values associated with each studied composition of the $Bi_{1-x}Sm_xFeO_3$ system along with their space group. It can be seen that the tolerance factor, t, decreases proportionally with the samarium content.

Table 5. 5. Space group and tolerance factor, t, associated with each composition.

$Bi_{1-x}Sm_xFeO_3$	Space group	t
x = 0.05	R3c	0.887
x = 0.10	R3c	0.886
x = 0.125	R3c+Pbam	0.885
x = 0.15	Pbam	0.884
x = 0.175	Pbam+Pnma	0.883
x = 0.20	Pnam	0.882

As the tolerance factors are smaller than unity, it means that Sm^{3+} does not fill the A-site space fully in Sm-substituted $BiFeO_3$ samples and, therefore, the Fe-O bonds are compressed, whereas the Bi-O bonds are under tension, causing the octahedral to rotate co-operatively to relieve lattice stress [28, 29]. Figure 5. 10 shows the perovskite crystal structure of the samples x = 0.05 (R3c) and x = 0.20 (Pnma), where the bond angle Fe-O(1)-Fe decreases with samarium content.

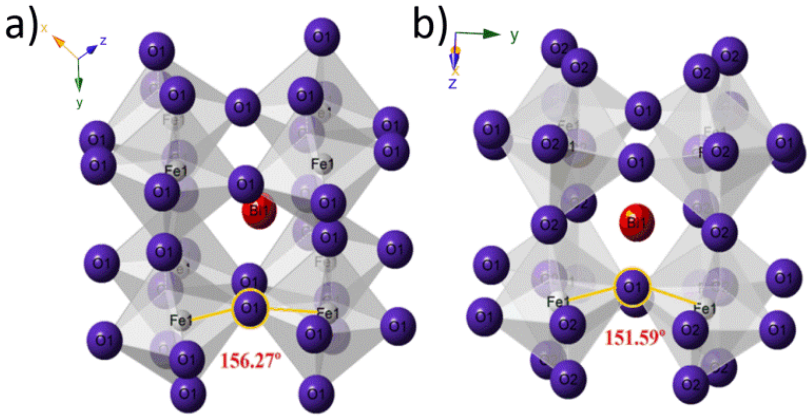

Figure 5. 10. The perovskite crystal structure of the samples: a) $Bi_{0.95}Sm_{0.05}FeO_3$ and b) $Bi_{0.80}Sm_{0.20}FeO_3$.

In Figure 5. 11, the Raman spectra of the sintered samples are shown for x = 0.05, 0.10, 0.15 and 0.20 compositions.

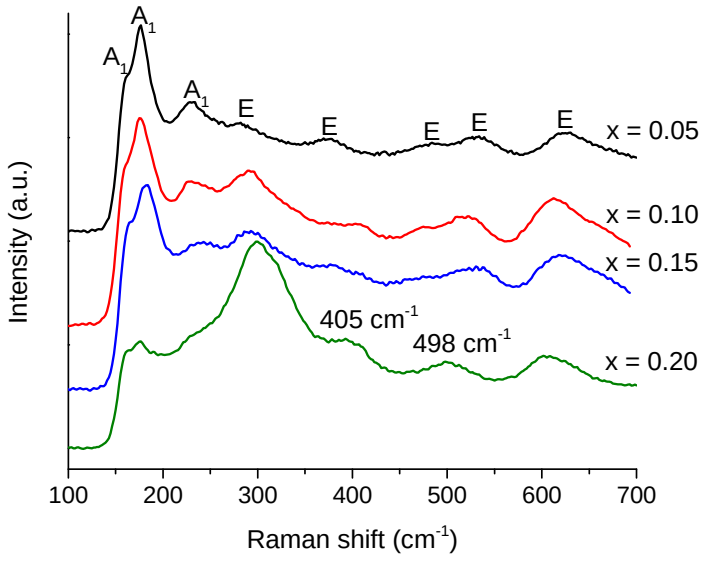

Figure 5. 11. Raman spectra of the $Bi_{1-x}Sm_xFeO_3$ system: a) x = 0.05, b) x = 0.10, c) x = 0.15 and d) x = 0.20.

The Raman spectra confirm that the substitution of bismuth for samarium is taking place. As stated in Section 4.4.3 (Chapter 4), the rhombohedral R3c symmetry exhibits 13 active Raman modes: $4A_1$+9E [30]. When the amount of samarium is low, it is easy to recognize eight of these modes. Three of them corresponds to the vibrational modes A_1 (at 159, 177, 230 cm^{-1}), whereas the others can be attributed to the vibrational modes E (at 285, 376, 483, 532 and 625 cm^{-1}). Certain differences between the Raman spectra can be found when the amount of samarium increases. Specifically, for x = 0.15 and x = 0.20 compositions, the vibrational modes bellow 200 cm^{-1} decrease their relative intensity significantly, as these modes are related to the reduction in the number of Bi-O bonds due to the

partial substitution of bismuth for samarium. For x = 0.20 composition, new intense bands appear at 300 cm^{-1} and at 498 cm^{-1}. Additionally, the band at 375 cm^{-1} suffers an important displacement to 405 cm^{-1}. This is an indication that a structural transformation takes place due to the effective substitution of bismuth for samarium, being consistent with the XRD data. A similar behaviour has been reported by other authors not only for samarium substituted $BiFeO_3$ but also for other substituents, including ytterbium substitution (Section 4.4.3, Chapter 4) [1, 6, 12, 14, 18, 25, 30-33].

5.4.3. Temperature dependant behaviour

Figures 5. 12 a) and b) show the DSC data from sintered samples of $Bi_{1-x}Sm_xFeO_3$ in the temperature ranges -50 < T/°C < 400 °C and 400 < T/°C < 850 °C, respectively. Data from all $Bi_{1-x}Sm_xFeO_3$ samples exhibit an endothermic peak at T~370 °C which corresponds to the onset of magnetic order (T_N = 360 °C for $BiFeO_3$). In addition, data from all samples, with the exception of the x = 0.2 sample, show an additional endothermic peak which appears at a temperature which declines with increasing samarium content. A similar behaviour related to the displacement of T_C to lower temperatures as the amount of substituent increases has been previously reported, including the partial substitution of bismuth for ytterbium until its solubility limit, as it has been studied in Section 4.4.2 (Chapter 4) [14, 18, 25]. Thus, the second enthodermic peaks may be related to the Curie temperature of the samples. The values of T_N and the temperatures associated with these second endothermic peaks (denoted as T_t) are included in Table 5. 6 for each composition.

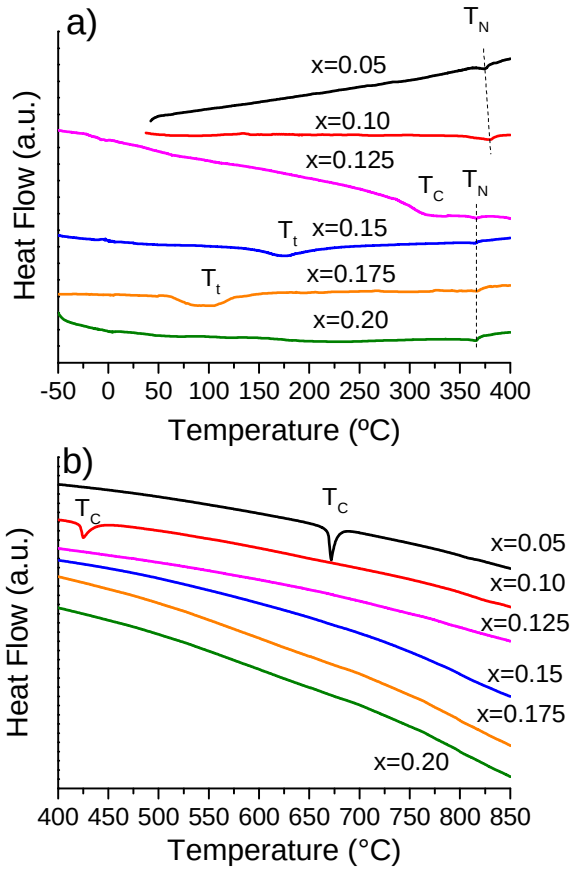

Figure 5. 12. DSC traces of the mechanosynthesised samples of composition $Bi_{1-x}Sm_xFeO_3$ registered after sintering at 900 ºC. The dashed lines linking T_N are guides to the eye. T_N, T_C and T_t denote the Néel, Curie and phase transition temperatures, respectively.

Table 5. 6. Néel temperatures, T_N, and transition temperatures, T_t, associated with each composition.

$Bi_{1-x}Sm_xFeO_3$	T_N (°C)	T_t (°C)
x = 0.05	374	671
x = 0.10	379	424
x = 0.125	366	314
x = 0.15	366	175
x = 0.175	366	107
x = 0.20	366	-

In order to establish the nature of the phase transitions associated with these latter endothermic features, XRD patterns were collected in air for $Bi_{0.95}Sm_{0.05}FeO_3$, $Bi_{0.90}Sm_{0.10}FeO_3$, $Bi_{0.875}Sm_{0.125}FeO_3$, $Bi_{0.85}Sm_{0.15}FeO_3$ and $Bi_{0.825}Sm_{0.175}FeO_3$ under *in-situ* conditions of heating at temperatures close to these DSC endothermic peaks. Figure 5. 13 shows a series of X-ray powder diffraction data collected as a function of temperature, in the range $20^o < 2\theta < 45^o$ from the $0.05 \leq x \leq 0.175$ compositions. Figures 5. 13 a) and b) reveal that the endothermic peaks seen at 671 ^{o}C and 424 ^{o}C in the DSC for the x = 0.05 and x = 0.10 samples, respectively, correspond to the structural phase transitions from the polar R3c structure at low temperature to a centrosymmetric Pnma structure at high temperature, as the double peak at 32.5^o 2θ merges into a new multiple peak at high temperature and new weak peaks appear at 25.2^o and 33.8^o, which intensities increase with temperature. The phase transition observed for nonsubstituted $BiFeO_3$ at its Curie temperature (830 ^{o}C) takes place in a directly analogous manner [34]. Thus, the Curie temperatures of the x = 0.05 and x = 0.10 samples can be identified at 671 ^{o}C and 424 ^{o}C, respectively. Figure 5. 13 d) shows a series of X-ray powder diffraction data collected as a function of temperature from the x = 0.15 sample, confirming that the peak observed at 175 ^{o}C in the DSC data corresponds to a phase transition from a Pbam structure at low temperature to a Pnma structure at high temperature, being both space groups centrosymmetric. Analogous variable temperature X-ray powder diffraction data collected from the x = 0.125 and x = 0.175 samples, at temperatures around the DSC peaks observed for these two phases (314 ^{o}C for x = 0.125, 107 ^{o}C for x = 0.175), are shown in Figures 5. 13 c) and e), respectively. A steady evolution is observed, corresponding to a change from the two phase mixtures at low temperature (R3c+Pbam for x = 0.125, Pbam+Pnma for x =

0.175) to a Pnma structure at high temperature. These data are summarized in Table 5. 7, along with the lattice parameters of the high-temperature Pnma phases, determined by use of the Celref software.

These results are consistent with the DSC data presented in Figure 5. 12 and confirm, for the first time, that the nature of the high temperature paraelectric phase is Pnma for the $Bi_{1-x}Sm_xFeO_3$ system.

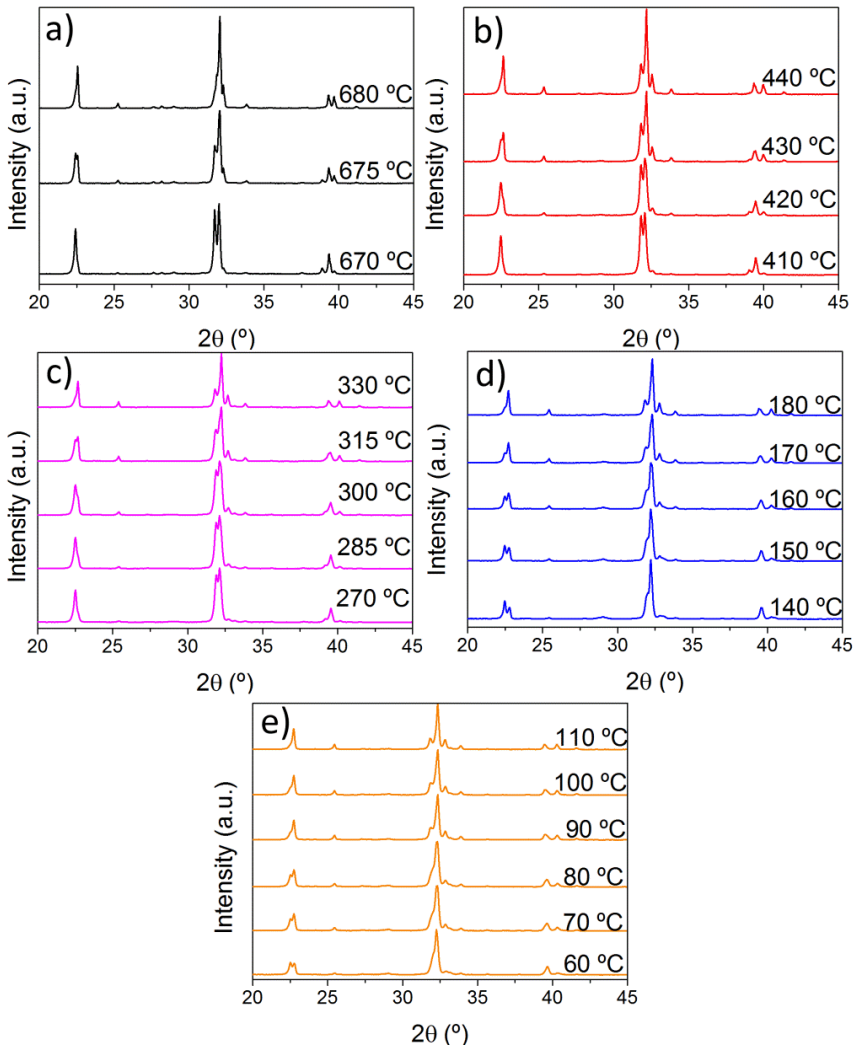

Figure 5. 13. *In-situ* XRD patterns of the samples at different temperatures: a) $Bi_{0.95}Sm_{0.05}FeO_3$, b) $Bi_{0.90}Sm_{0.10}FeO_3$, c) $Bi_{0.875}Sm_{0.125}FeO_3$, d) $Bi_{0.85}Sm_{0.15}FeO_3$ and e) $Bi_{0.825}Sm_{0.175}FeO_3$.

Table 5. 7. Phase transition temperatures and cell parameters at 800 ºC, 500 ºC, 400 ºC, 200 ºC and 150 ºC for x = 0.05, x = 0.10, x = 0.125, x = 0.15 and x=0.175 compositions, respectively.

Sample	T (ºC)	Phase transition	Cell parameters
$Bi_{0.95}Sm_{0.05}FeO_3$	671	R3c→Pnma	T=800ºC
			a=5.6237(3), b=7.9166(2), c=5.5709(4), $\alpha = \beta = \gamma$ =90º
$Bi_{0.90}Sm_{0.10}FeO_3$	424	R3c→Pnma	T=500ºC
			a=5.6338(5), b=7.8677(5), c=5.5264(2), $\alpha = \beta = \gamma$ =90º
$Bi_{0.875}Sm_{0.125}FeO_3$	314	R3c+Pbam→Pnma	T=400ºC
			a=5.6376(4), b=7.8714(3), c=5.5199(5), $\alpha = \beta = \gamma$ =90º
$Bi_{0.85}Sm_{0.15}FeO_3$	175	Pbam→Pnma	T=200ºC
			a=5.6323(3), b=7.8351(2), c=5.4884(2), $\alpha = \beta = \gamma$ =90º
$Bi_{0.825}Sm_{0.175}FeO_3$	107	Pbam+Pnma→Pnma	T=150ºC
			a=5.6243(5), b=7.8499(5), c=5.4755(4), $\alpha = \beta = \gamma$ =90º

Figure 5. 14 shows relative permittivity data collected as a function of temperature at a frequency of 100 KHz from the x = 0.10, 0.125, 0.15 and 0.175 samples, in order to further confirm the results obtained from the DSC and X-ray thermodiffraction studies. The data from the x = 0.10 and x = 0.125 samples show maxima in the permittivity at 425 ºC and 315 ºC, respectively, which provide confirmation that the phase transitions in these samples at these temperatures correspond to transitions from ferroelectric to paraelectric states, associated with the Curie temperatures. Likewise, the lack of equivalent maxima in the permittivity's of the samples x = 0.15 and x = 0.175 (which present a step in the permittivity at ~170 ºC and ~110 ºC, respectively) are also consistent with the structural phase transitions described in Table 5. 7. It is worth remarking the high values of permittivity obtained for composition x = 0.15 in the entire range of temperatures studied, as compared with the permittivity values of the rest of samples.

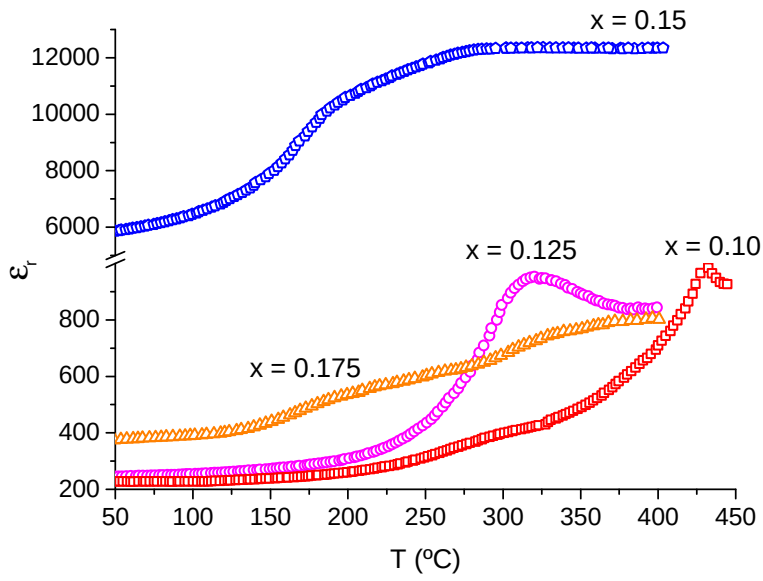

Figure 5. 14. Temperature dependence of relative permittivity at a frequency of 100 KHz for x = 0.10, 0.125, 0.15 and 0.175 compositions.

The Rietveld refinements, DSC, X-ray thermodiffraction and permittivity data allow a tentative phase diagram of the $Bi_{1-x}Sm_xFeO_3$ system to be constructed as shown in Figure 5. 15. It can be observed the compositional dependence of T_C and T_N, together with the corresponding phase transition temperatures of compositions x = 0.15, 0.175 and 0.20. Two compositional ranges of phase coexistence may be approximately identified: R3c + Pbam for 0.10 < x < 0.15 and Pbam + Pnma for 0.175 < x < 0.20. Additionally, it is important to remark that the high temperature phase Pnma has been confirmed for the first time for the $Bi_{1-x}Sm_xFeO_3$ system by X-ray thermodiffraction. This phase diagram is consistent with others for different rare-earth $Bi_{1-x}RE_xFeO_3$ systems [20].

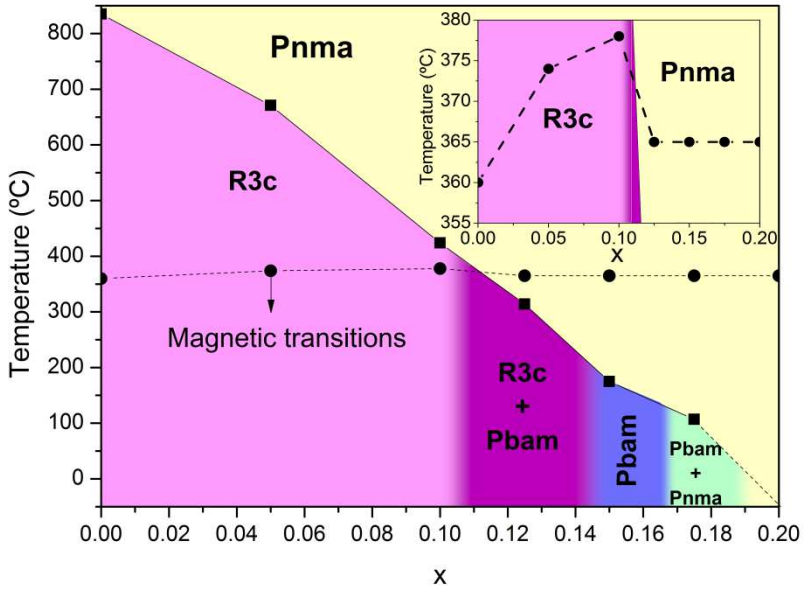

Figure 5. 15. Tentative phase diagram for the $Bi_{1-x}Sm_xFeO_3$ system. Néel (T_N), Curie (T_C) and phase transition (T_t) temperatures were taken from the DSC traces shown in Figure 5. 12. The inset details the changes of T_N in the studied compositional range.

5.4.4. Microstructural and chemical characterization

The microstructure of the samples prepared by mechanosynthesis and sintering at 900 ºC was analysed by means of TEM and SEM.

Representative results obtained by TEM, for samples of x = 0.10, x = 0.15 and x = 0.20 compositions are presented in Figure 5. 16.

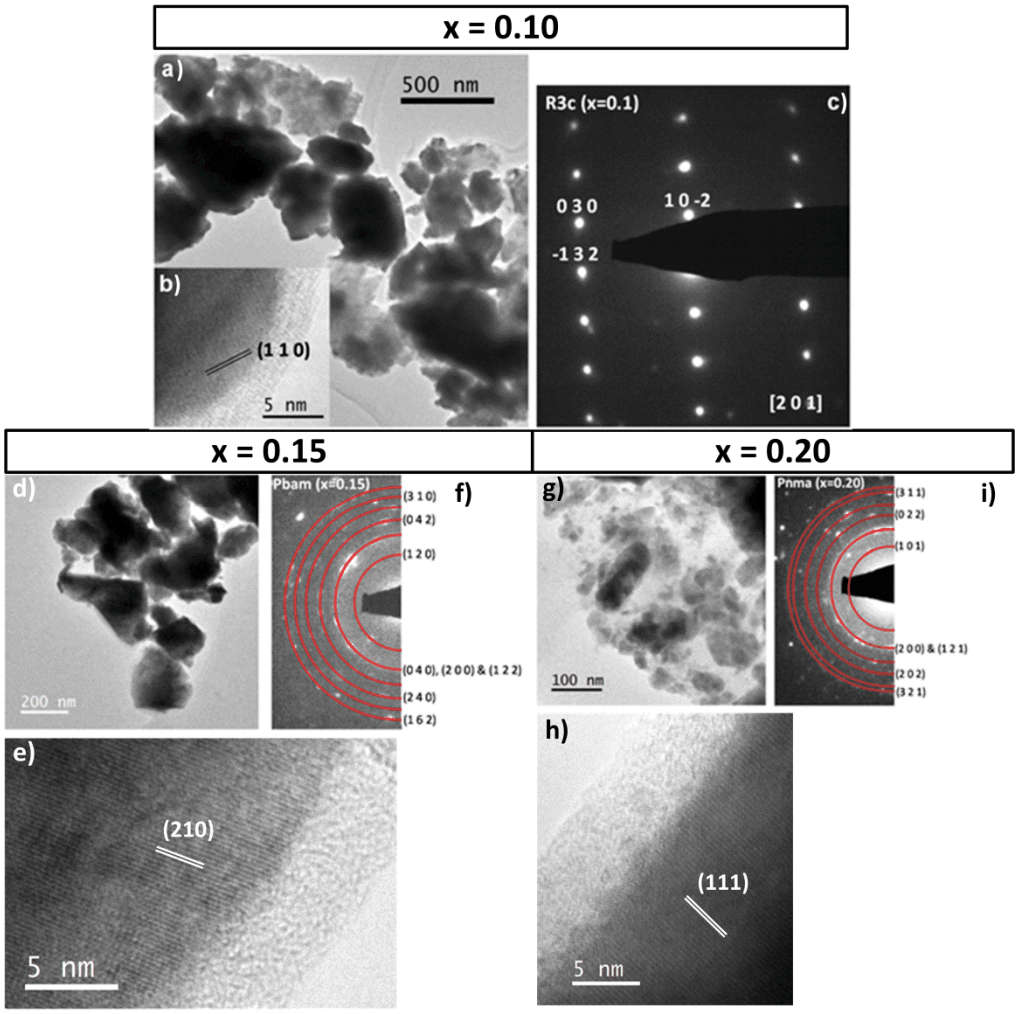

Figure 5. 16. TEM micrographs, high resolution images and ED patterns of samples with different compositions: x = 0.10 (a, b, c), x = 0.15 (d, e, f) and x = 0.20 (g, h, i).

All samples resulted to be formed by agglomerated crystalline domains that oscillate between 100 and 300 nm, as it can be seen in Figures 5. 16 a), d) and g). For the x = 0.10 sample, a high resolution micrograph of one of these domains is presented in Figure 5. 16 b), where the (1 1 0) plane, corresponding with the symmetry R3c of the analysed phase, have been identified (marked in the high resolution image). Due to the size of

the crystalline domains, many of the obtained electron diffraction (ED) patterns are formed by rings, although some larger domains could be oriented like the one depicted in Figure 5. 16 c) along the [2 0 1] zone axis. Samples x = 0.15 and x = 0.20 showed smaller crystalline domains than x = 0.10. The ED patterns are basically formed by rings as Figures 5. 16 f) and i) depict and are in good agreement with the X-ray diffraction data. Resolved high resolution images for x = 0.15 and x = 0.20 compositions are shown in Figures 5. 16 e) and h), respectively, where the (2 1 0) and (1 1 1) planes corresponding with the symmetries Pbam and Pnma have been also identified.

Figure 5. 17 shows the SEM micrographs and the EDX spectra obtained for the $Bi_{1-x}Sm_xFeO_3$ samples after sintering at 900 ^oC for x = 0.05, 0.10, 0.15 and 0.20 compositions. The microstructure of the samples is composed by densely packed grains with a quite wide distribution size. It can be clearly observed that the grain size decreases with the amount of substituent, in an analogous directly manner to the ytterbium substitution (Section 4.4.5, Chapter 4). For instance, the grain size for composition x = 0.05 is between 1 and 4 μm while the sample with the higher amount of samarium (x = 0.20) presents smaller grains oscillating between 0.5 and 2 μm. This tendency has been previously observed by several authors as well [4, 6, 12, 14, 35]. Table 5. 8 lists the elemental composition of the samples, determined by the semiquantitative analysis of the EDX spectra shown in Figure 5. 17. As it may be observed, the experimental results are consistent with the expected compositions and, therefore, the materials maintain the nominal composition after the whole synthesis process. However, slight differences are observed, which can be attributed to the intrinsic errors of the EDX method.

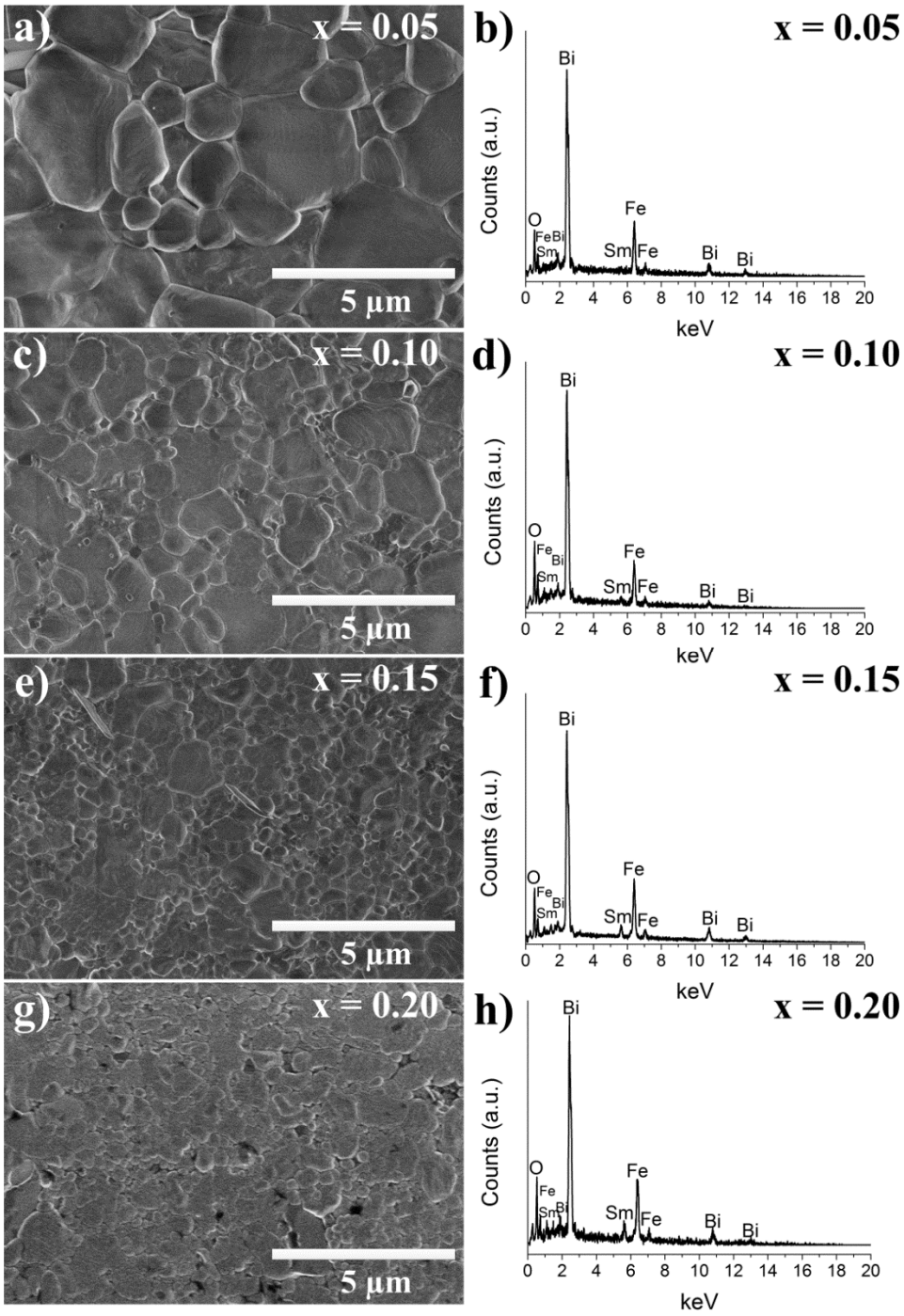

Figure 5. 17. SEM micrographs and EDX spectra of samples obtained after milling and sintering at 900 °C for x = 0.05 (a, b), x = 0.10 (c, d), x = 0.15 (e, f) and x = 0.20 (g, h) compositions.

Table 5. 8. Elemental composition of the samples prepared by mechanosynthesis and sintering at 900 ºC, determined by the semicuantitative analysis of EDX spectra.

		Experimental atomic composition (%)		
Sample	Theoretical atomic composition Fe/Sm/Bi (%)	Fe	Sm	Bi
$Bi_{0.95}Sm_{0.05}FeO_3$	50.0/2.5/47.5	51.0 ± 1.9	2.2 ± 0.7	46.8 ± 1.5
$Bi_{0.90}Sm_{0.10}FeO_3$	50.0/5.0/45.0	49.2 ± 1.7	5.0 ± 0.5	45.8 ± 1.5
$Bi_{0.85}Sm_{0.15}FeO_3$	50.0/7.5/42.5	49.4 ± 1.5	7.6 ± 0.7	43.0 ± 1.7
$Bi_{0.80}Sm_{0.20}FeO_3$	50.0/10.0/40.0	50.7 ± 1.8	9.9 ± 0.6	39.4 ± 1.6

5.4.5. Optical properties

The optical properties of the $Bi_{1-x}Sm_xFeO_3$ system was studied by UV-Vis diffuse reflectance spectroscopy. Figure 5. 18 shows the absorption spectra for samples of x = 0.05, x = 0.10, x = 0.15 and x = 0.20 compositions. It clearly suggests the potential use of the $Bi_{1-x}Sm_xFeO_3$ system as visible-light photocatalyst, as it can absorb considerable amount of light in the visible region for the whole studied compositional range. From the insets of Figure 5. 18, the band gap energy (E_g) of the samples can be calculated according to the procedure explained in Section 3.3.6 (Chapter 3). The E_g values obtained for each composition are presented in Table 5. 9.

Table 5. 9. Band gap energy, E_g, for the $Bi_{1-x}Sm_xFeO_3$ system.

$Bi_{1-x}Sm_xFeO_3$	E_g (eV)
x = 0.05	2.06
x = 0.10	2.04
x = 0.15	2.00
x = 0.20	1.94

The E_g values are similar to those obtained for the ytterbium substituted $BiFeO_3$ samples (Section 4.4.6, Chapter 4). In an analogous manner, there is a slight tendency, as the band gap energy slightly decreases when the amount of substituent increases. Moreover, the E_g

values obtained are smaller than those previously reported for samarium substituted samples, which highlight the promising character of the materials obtained as photocatalysts [36, 37].

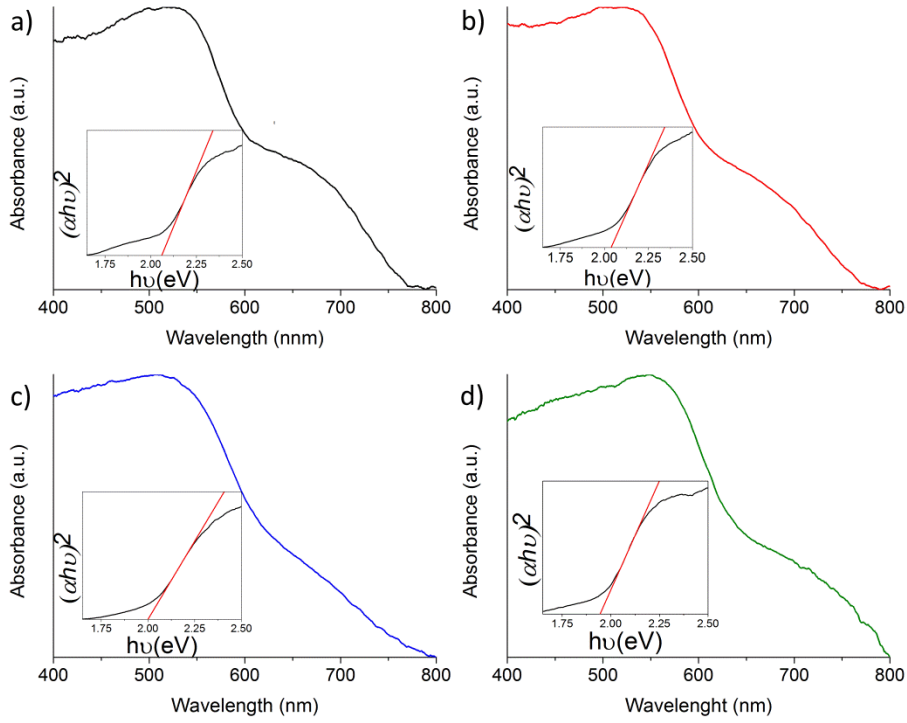

Figure 5. 18. UV-Vis diffuse reflectance spectra of the $Bi_{1-x}Sm_xFeO_3$ system: a) x = 0.05, b) x = 0.10, c) x = 0.15 and d) x = 0.20 compositions. The insets represent $(\alpha h\upsilon)^2$ versus photon energy for the calculation of the corresponding band gap energy.

5.4.6. Electrical properties

The electrical behaviour of the samples was studied as a function of temperature by impedance spectroscopy. The samples were highly insulating at room temperature, presenting low conductivity from 300 ºC. Figures 5. 19, 5. 20, 5. 21 and 5. 22 present impedance data from 300 ºC to 380 ºC for x = 0.05, 0.10, 0.15 and 0.20 compositions, respectively. The impedance complex plane plots (Figures 5.19 a), 5. 20 a), 5. 21 a) and 5. 22 a)) show single arcs at each temperature. Additionally, Figures 5.19 b), 5. 20 b), 5. 21 b) and 5. 22 b) represent the Z''/M'' spectroscopic plots at 380 ºC associated with each composition. The Z''/M'' plots are formed by single broad peaks, practically coincident at the maxima frequencies in all the samples. Moreover, any additional peaks at lower frequencies in the Z'' spectrum are observed. These results support the electrical homogeneity of the $Bi_{1-x}Sm_xFeO_3$ system prepared by mechanosynthesis and sintering at 900 ºC. The capacitance data as a function of frequency are presented in Figures 5. 19 c), 5. 20 c), 5. 21 c) and 5. 22 c) for x = 0.05, x = 0.10, x = 0.15 and x = 0.20 compositions, respectively, where similar tendencies can be clearly observed. For every studied composition, the capacitance data are composed by high-frequency plateaus that are followed by small increase in the C' values at low frequency. This tendency may indicate a possible power law response [38].

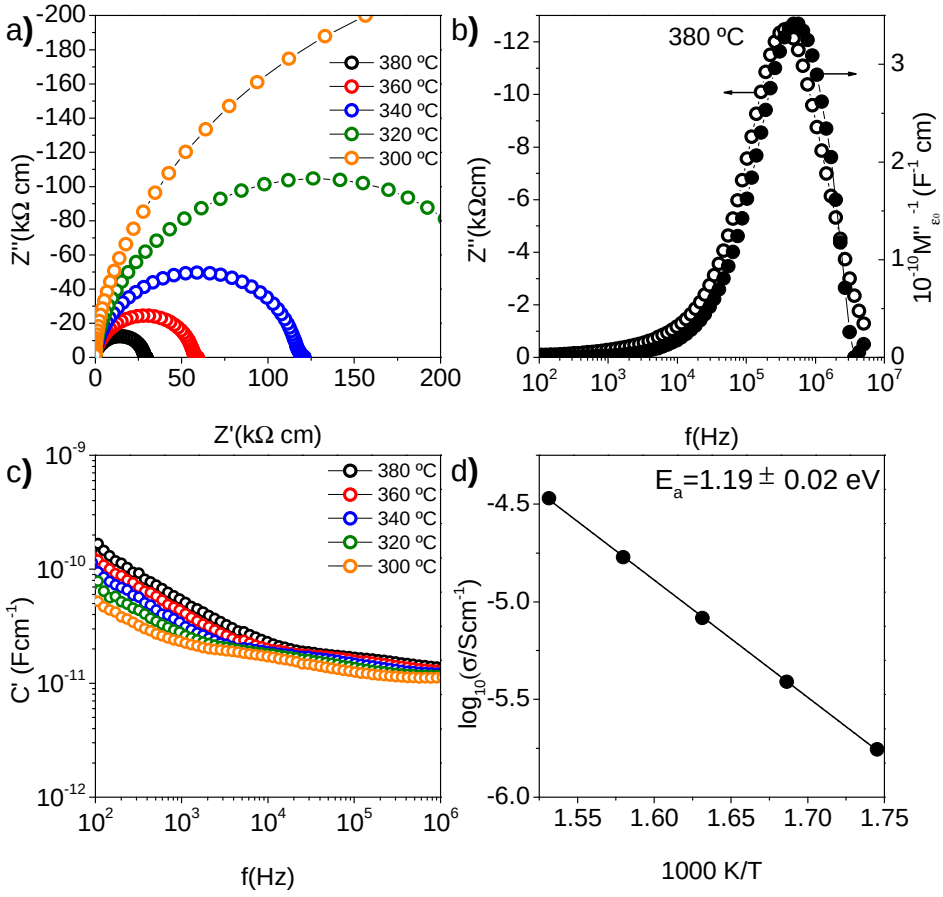

Figure 5. 19. a) Impedance complex plane plots, b) Z″/M″ spectroscopic plots at 380 ºC, c) C′ versus frequency and d) bulk Arrhenius plot for the sample of x = 0.05 composition obtained after milling and sintering at 900 ºC.

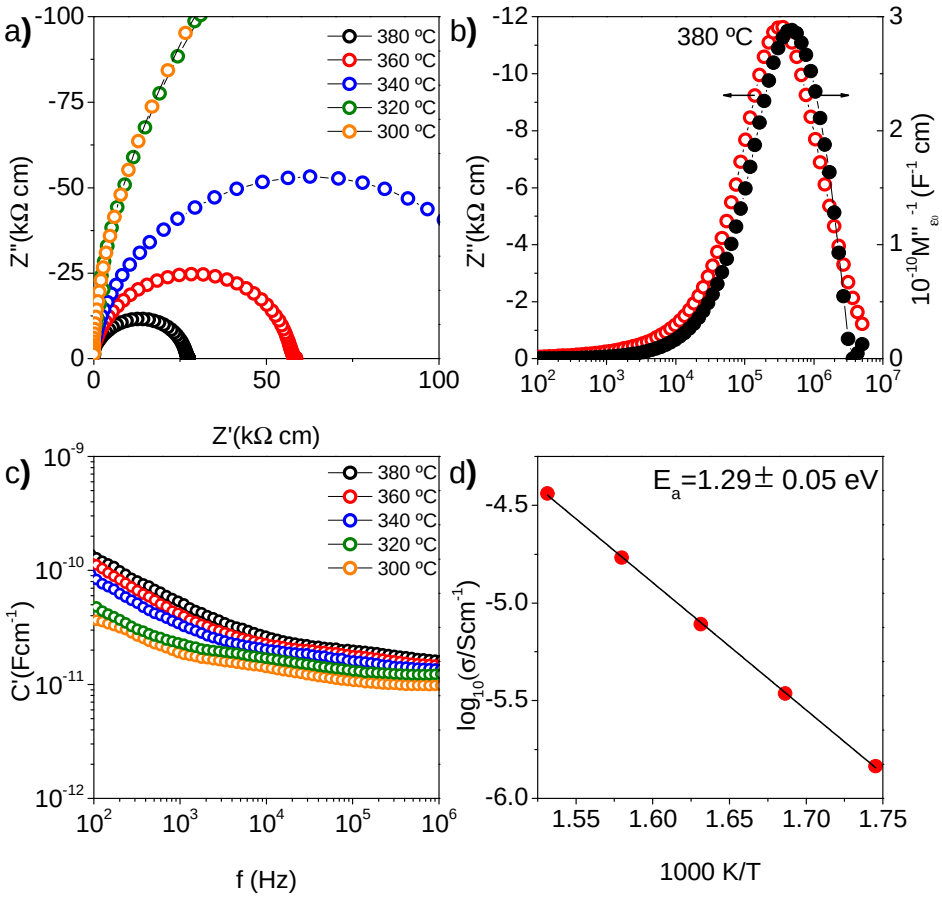

Figure 5. 20. a) Impedance complex plane plots, b) Z″/M″ spectroscopic plots at 380 ºC, c) C′ versus frequency and d) bulk Arrhenius plot for the sample of x = 0.10 composition obtained after milling and sintering at 900 ºC.

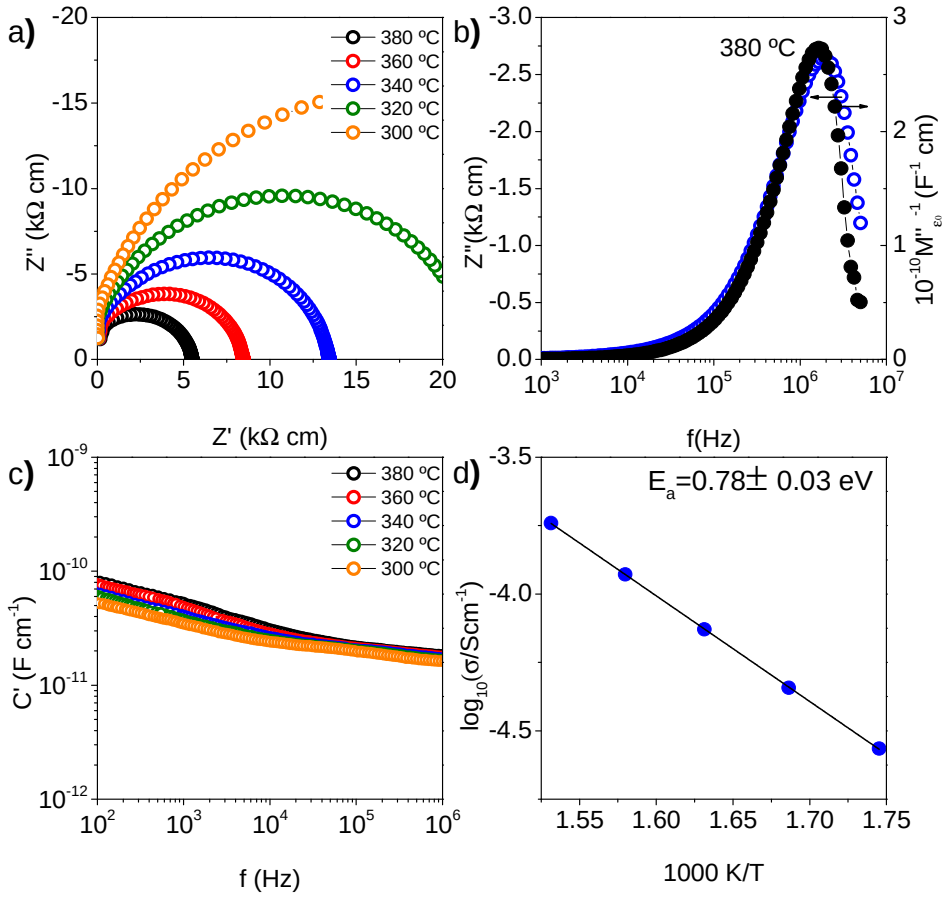

Figure 5. 21. a) Impedance complex plane plots, b) Z″/M″ spectroscopic plots at 380 ºC, c) C′ versus frequency and d) bulk Arrhenius plot for the sample of x = 0.15 composition obtained after milling and sintering at 900 ºC.

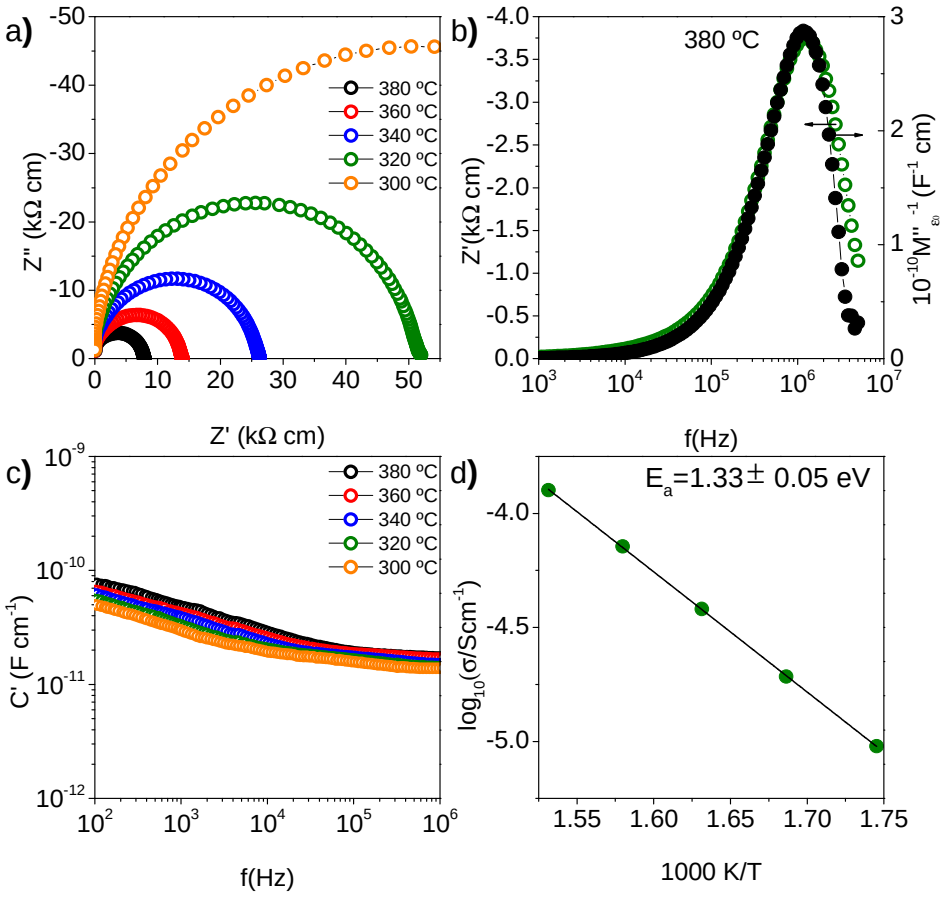

Figure 5. 22. a) Impedance complex plane plots, b) Z″/M″ spectroscopic plots at 380 ºC, c) C′ versus frequency and d) bulk Arrhenius plot for the sample of x = 0.20 composition obtained after milling and sintering at 900 ºC.

The resistivity values for each studied temperature obtained from the interception on the real Z′ axes (Figures 5. 19 a), 5. 20 a), 5. 21 a) and 5. 22 a)), in conventional Arrhenius format are individually presented for each composition in Figures 5. 19 d), 5. 20 d), 5. 21 d) and 5. 22 d). For the sake of clarity and comparison purposes, Figure 5. 23 presents the bulk conductivity data for all compositions. Extrapolating from this graph, the

conductivities of the samples are small with resistivity values between 2×10^{17} and 1×10^{12} Ω cm at room temperature. These low conductivities suggest that other sources of conductivity, such as mixed valence of Fe associated with possible oxygen non-stoichiometry, have been avoided during the sample synthesis in contrast with the results presented by other authors, whose samples present high levels of conductivity [8]. Additionally, the conductivity exhibits a linear trend with temperature with activation energies of 1.19, 1.29, 0.78 and 1.33 eV for x = 0.05, x = 0.10, x = 0.15 and x = 0.20, respectively. In general, the conductivity increases with the samarium content, with the exception of $Bi_{0.85}Sm_{0.15}FeO_3$ that presents the lowest activation energy as well as the highest conductivity.

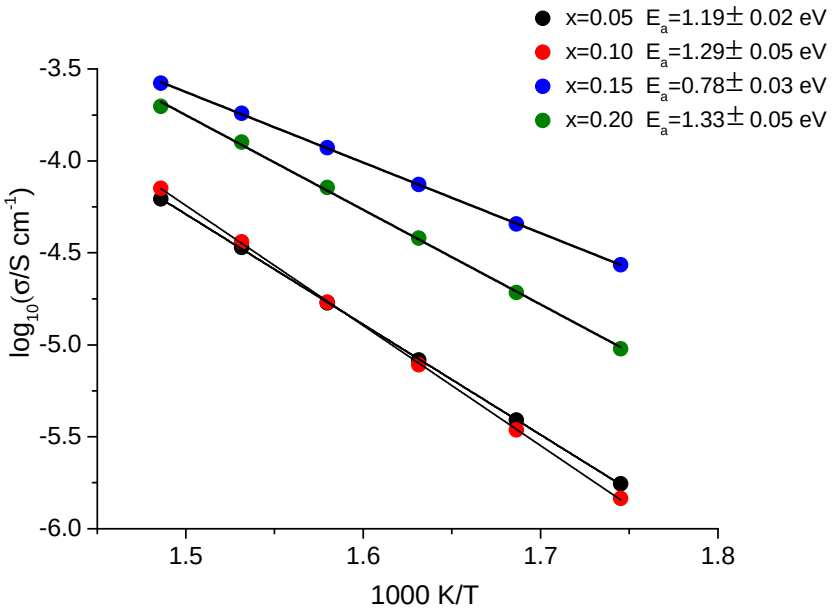

Figure 5. 23. Bulk conductivity data for $Bi_{1-x}Sm_xFeO_3$ samples of x = 0.05, x = 0.10, x = 0.15 and x = 0.20 compositions.

The conduction mechanism of the samples was studied at 380 ºC by measuring the impedance under different oxygen partial pressure

atmospheres (nitrogen, air and nitrogen), as shown in Figure 5. 24 for x = 0.05, x = 0.10, x = 0.15 and x = 0.20 compositions.

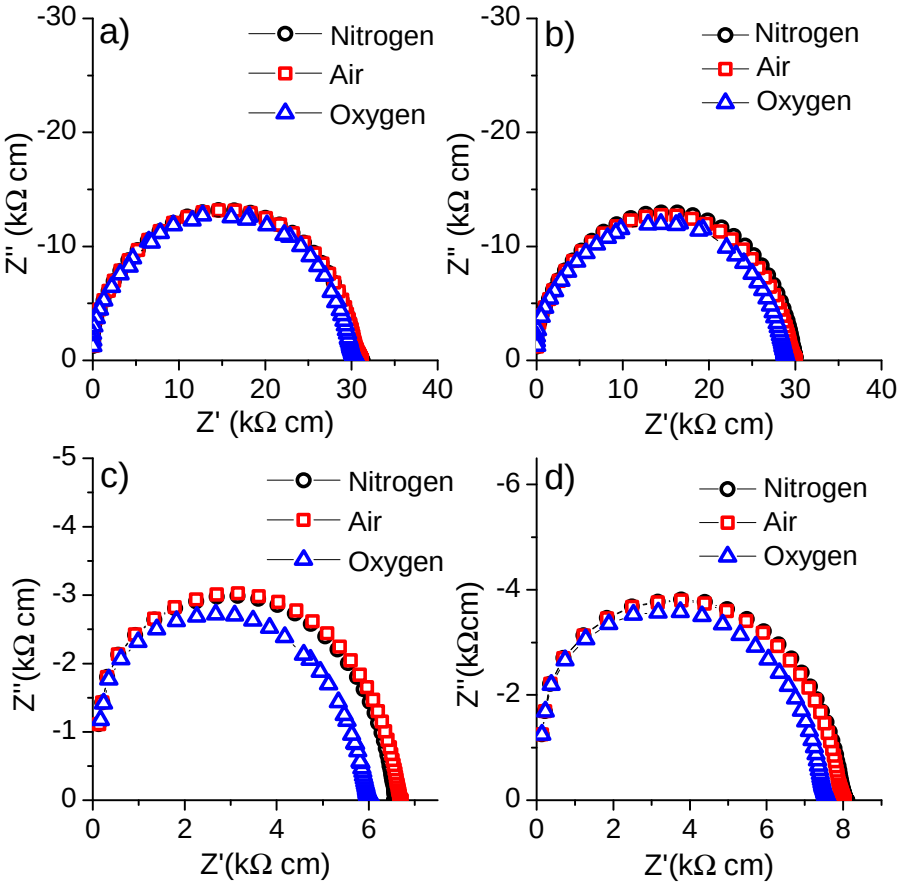

Figure 5. 24. Impedance complex-plane plots at 380 °C in nitrogen, air and oxygen for $Bi_{1-x}Sm_xFeO_3$ samples: a) x = 0.05, b) x = 0.10, c) x = 0.15 and d) x = 0.20 compositions.

The resistivity of all samples slightly decreases as the partial pressure of oxygen increases, indicating a possible p-type conduction mechanism. Although the resistivity changes as a function of the oxygen partial pressure are small, the same general tendency has been observed in

every sample, which may indicate that the conduction is intrinsic but slightly dominated by holes, as explained in Section 4.4.6 of Chapter 4 for the $Bi_{1-x}Yb_xFeO_3$ system. A similar behaviour has been observed for other Bi substituted $BiFeO_3$ samples [25, 26].

5.4.7. Magnetic properties

Figure 5. 25 shows the magnetisation data from the $Bi_{1-x}Sm_xFeO_3$ system (x = 0.05, x = 0.10, x = 0.15 and x = 0.20) collected at 5 K and the maximum temperature attained by the instrument (350 K), as a function of the applied field. The extracted parameters of the magnetisation data: coercive field, H_C, remnant magnetization, M_r, and magnetization at 5 T, M_{5T}, at 5 K and 350 K are presented in Table 5. 10. At both temperatures these parameters increase with samarium content for x = 0.05 and x = 0.10 compositions. Moreover, it can be observed from the data collected at 350 K, a nearly linear field-dependent magnetization for these samples with a very weak hysteresis loop that do not saturate at the maximum field applied (Figure 5. 25 a)). Conversely, and as expected due to the minimization of thermal energy, data collected at 5 K from x = 0.05 and x = 0.10 compositions exhibit larger hysteresis. This behaviour has been previously observed for mechanosynthesized $BiFeO_3$ and related compounds [25, 39, 40], confirming the antiferromagnetic nature of the samples at these temperatures. As the amount of samarium increases, there is a dramatic increase in M_r, which is remarkable for composition x = 0.15. Large M_r values for x = 0.15 are obtained not only at 5 K but also at 350 K. It may be associated with the change to the Pbam structure. However, it is necessary to point out that this sample (x = 0.15) is in the paraelectric compositional range.

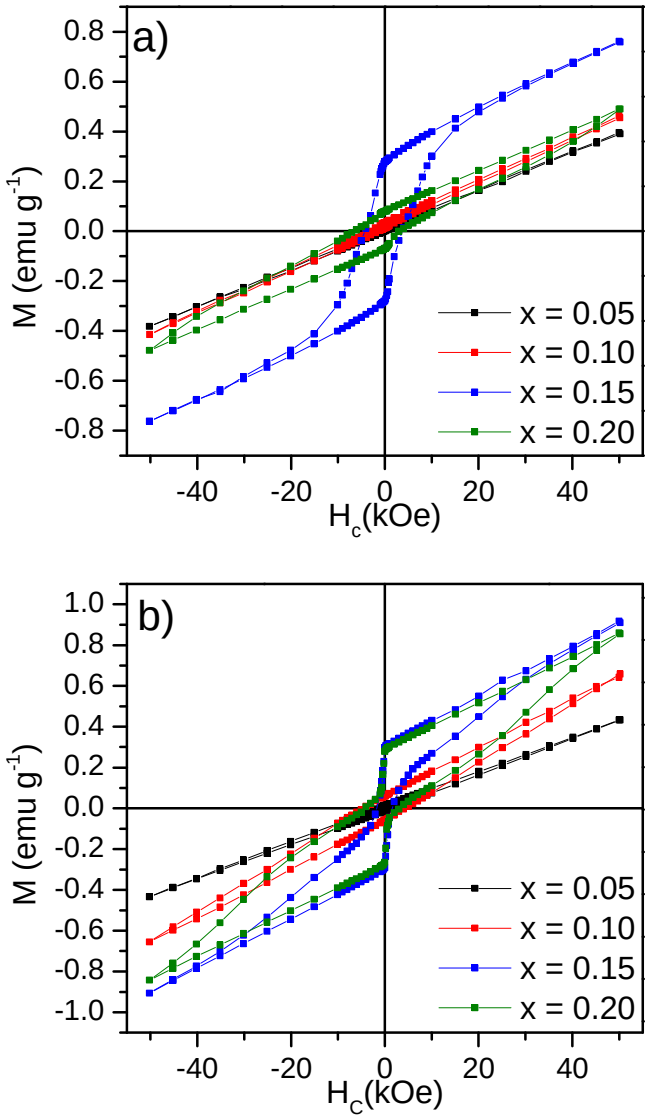

Figure 5. 25. Magnetisation data collected as a function of applied filed for the samples of the $Bi_{1-x}Sm_xFeO_3$ system (x = 0.05, x = 0.10, x = 0.15 and x = 0.20) at: a) 350 K and b) 5 K.

Table 5. 10. Coercive field (H_C), remnant magnetization (M_r) and 5 Tesla magnetization (M_{5T}) extracted from magnetisation data collected at 5 K and 350 K as a function of applied field from samples of the $Bi_{1-x}Sm_xFeO_3$ system (x = 0.05, x = 0.10, x = 0.15 and x = 0.20), obtained by mechanosynthesis and sintering at 900 °C.

Temperature	5 K			350 K		
$Bi_{1-x}Sm_xFeO_3$	H_c (Oe)	M_r (emu g^{-1})	M_{5T} (emu g^{-1})	H_c (Oe)	M_r (emu g^{-1})	M_{5T} (emu g^{-1})
5	1578	0.0034	0.43399	792	0.0178	0.3960
10	4413	0.0809	0.64227	759	0.0311	0.4629
15	1627	0.3037	0.9150	4028	0.3342	0.76170
20	3737	0.2823	0.8583	4750	0.0739	0.48991

5.5. CONCLUSIONS

High-quality samples of the $Bi_xSm_{1-x}FeO_3$ system ($0.05 \leq x \leq 0.2$) have been successfully prepared by mechanosynthesis and conventional sintering. Pellets of the samples sintered at 900 °C present densities above 93% in all cases. Rietveld refinements demonstrate that, basically, single phase ceramics are obtained for x = 0.05, 0.10, 0.15 and 0.20 samples and two phase mixtures for x = 0.125 and 0.175. Therefore, the samarium content governs the crystallographic structure of the samples, as assayed by Rietveld refinements and further confirmed Raman spectroscopy. Particularly, for x = 0.05 and 0.10, the corresponding XRD diffraction patterns can be indexed in the rhombohedral non-centrosymmetric R3c space group. For x = 0.15 and x = 0.20, phase transitions take place to the orthorhombic centrosymmetric Pbam and Pnma structures, respectively. On the other hand, mixtures of rhombohedral and orthorhombic phases have been detected by XRD for x = 0.125 and x = 0.175 compositions. For x = 0.125, the system is comprised by R3c (72%) and Pbam (28%) phases, and for x = 0.175 a mixture of Pbam (74%) and Pnma (26%) phases was obtained. Additionally, by a combination of the crystallographic

information extracted by the Rietveld refinements, TEM, DSC, temperature-dependent DRX and permittivity data a tentative phase diagram has been constructed, where the presence of the high temperature Pnma phase has been confirmed for the first time for the $Bi_xSm_{1-x}FeO_3$ system. Scanning electron microscopy measurements show that the samples contain densely packed grains whose size decrease with the amount of substituent. The EDX spectra reveal that the initial stoichiometry of the samples has been maintained after the synthesis and sintering processes. The optical band gap of the samples, measured by diffuse reflectance UV-vis spectroscopy, is small and decreases with the amount of samarium, which reveals their potential use as visible-light photocatalysts. The electrical and magnetic properties of the $Bi_xSm_{1-x}FeO_3$ system have been unambiguously measured by impedance spectroscopy and magnetisation measurements. Regarding the electrical properties, the samples resulted to be electrically homogenous and highly insulating at room temperature. Moreover, a possible p-type conduction mechanism has been detected by measuring the impedance data under atmospheres with different oxygen partial pressures. Samarium substitution enhances the magnetic properties of the $Bi_xSm_{1-x}FeO_3$ system, being particularly remarkable the dramatic increase in the remnant magnetization when the level of samarium substitution drives a structural phase transition to the Pbam phase ($x = 0.15$). However, as ferroelectric behaviour is lost at this point, the enhancement in magnetic properties does not lead to improved magnetoelectric performance.

In summary, it has been shown that mechanical approaches allow the preparation of single-phase samples in which the possible amount of secondary phases, that hamper the study of the physical properties, is reduced to a minimum, in contrast to many published works describing

the synthesis of bulk $Bi_{1-x}Sm_xFeO_3$ samples by several methods. They often report significant amounts of secondary phases, such as $Bi_2Fe_4O_9$ [21, 22, 41-48], that do not allow the unambiguous evaluation of the physical properties of the prepared samples. This highlights the importance of choosing an appropriate method of synthesis, which is probably related to the big data discrepancies found in the literature regarding the crystal structure as a function of samarium content and the physical behaviour.

5.6. REFERENCES

[1] Yao Y.B., Liu W.C. and Mak C.L., *Pyroelectric properties and electrical conductivity in samarium doped $BiFeO_3$ ceramics*. Journal of Alloys and Compounds, **2012**, 527, p. 157-162.

[2] Nalwa K.S., Garg A. and Upadhyaya A., *Effect of samarium doping on the properties of solid-state synthesized multiferroic bismuth ferrite*. Materials Letters, **2008**, 62 (6–7), p. 878-881.

[3] Khomchenko V.A., Paixao J.A., Costa B.F.O., Karpinsky D.V., Kholkin A.L., Troyanchuk I.O., Shvartsman V.V., Borisov P. and Kleemann W., *Structural, ferroelectric and magnetic properties of $Bi_{0.85}Sm_{0.15}FeO_3$ perovskite*. Crystal Research and Technology, **2011**, 46 (3), p. 238-242.

[4] Pattanayak S., Choudhary R.N.P. and Das P., *Effect of Sm-substitution on structural, electrical and magnetic properties of $BiFeO_3$*. Electronic Materials Letters, **2014**, 10 (1), p. 165-172.

[5] Walker J., Bryant P., Kurusingal V., Sorrell C., Kuscer D., Drazic G., Bencan A., Nagarajan V. and Rojac T., *Synthesis-phase-composition relationship and high electric-field-induced electromechanical behavior of*

samarium-modified $BiFeO_3$ ceramics. Acta Materialia, **2015**, 83, p. 149-159.

[6] Singh H. and Yadav K.L., *Structural, dielectric, vibrational and magnetic properties of Sm doped $BiFeO_3$ multiferroic ceramics prepared by a rapid liquid phase sintering method*. Ceramics International, **2015**, 41 (8), p. 9285-9295.

[7] Chen X.M., Wang J.L., Yuan G.L., Wu D., Liu J.M., Yin J. and Liu Z.G., *Structure, ferroelectric and piezoelectric properties of multiferroic $Bi_{0.875}Sm_{0.125}FeO_3$ ceramics*. Journal of Alloys and Compounds, **2012**, 541, p. 173-176.

[8] Godara P., Agarwal A., Ahlawat N. and Sanghi S., *Crystal structure refinement, dielectric and magnetic properties of Sm modified $BiFeO_3$ multiferroic*. Journal of Molecular Structure, **2015**, 1097, p. 207-213.

[9] Maurya D., Thota H., Garg A., Pandey B., Chand P. and Verma H.C., *Magnetic studies of multiferroic $Bi_{1-x}Sm_xFeO_3$ ceramics synthesized by mechanical activation assisted processes*. Journal of Physics-Condensed Matter, **2009**, 21 (2).

[10] Alikin D.O., Turygin A.P., Walker J., Rojac T., Shvartsman V.V., Shur V.Y. and Kholkin A.L., *Quantitative phase separation in multiferroic $Bi_{0.88}Sm_{0.12}FeO_3$ ceramics via piezoresponse force microscopy*. Journal of Applied Physics, **2015**, 118 (7).

[11] Puli V.S., Pradhan D.K., Martinez R., Coondoo I., Panwar N. and Katiyar R.S., *Temperature Dependent Magnetic, Dielectric Studies of Sm-Substituted Bulk $BiFeO_3$*. Journal of Superconductivity and Novel Magnetism, **2012**, 25 (4), p. 1109-1114.

[12] Dai H.Y., Chen Z.P., Li T. and Li Y., *Microstructure and properties of Sm-substituted $BiFeO_3$ ceramics*. Journal of Rare Earths, **2012**, 30 (11), p. 1123-1128.

[13] Mukherjee A., Basu S., Manna P.K., Yusuf S.M. and Pal M., *Giant magnetodielectric and enhanced multiferroic properties of Sm doped bismuth ferrite nanoparticles*. Journal of Materials Chemistry C, **2014**, 2 (29), p. 5885-5891.

[14] Khodabakhsh M., Sen C., Khassaf H., Gulgun M.A. and Misirlioglu I.B., *Strong smearing and disappearance of phase transitions into polar phases due to inhomogeneous lattice strains induced by A-site doping in $Bi_{(1-x)}A_{(x)}FeO_{(3)}$ (A: La, Sm, Gd)*. Journal of Alloys and Compounds, **2014**, 604, p. 117-129.

[15] Walker J., Budic B., Bryant P., Kurusingal V., Sorrell C.C., Bencan A., Rojac T. and Valanoor N., *Robust Polarization and Strain Behavior of Sm-Modified $BiFeO_3$ Piezoelectric Ceramics*. Ieee Transactions on Ultrasonics Ferroelectrics and Frequency Control, **2015**, 62 (1), p. 83-87.

[16] Thakuria P. and Joy P.A., *High room temperature ferromagnetic moment of Ho substituted nanocrystalline $BiFeO_3$*. Applied Physics Letters, **2010**, 97 (16).

[17] Wu Y.-J., Chen X.-K., Zhang J., Liu J., Xiao W.-S., Wu Z. and Chen X.-J., *Pressure effect on structural and vibrational properties of Sm-substituted $BiFeO_3$*. Journal of Applied Physics, **2013**, 114 (15).

[18] Karimi S., Reaney I.M., Han Y., Pokorny J. and Sterianou I., *Crystal chemistry and domain structure of rare-earth doped $BiFeO_3$ ceramics*. Journal of Materials Science, **2009**, 44 (19), p. 5102-5112.

[19] Khomchenko V.A., Paixao J.A., Shvartsman V.V., Borisov P., Kleemann W., Karpinsky D.V. and Kholkin A.L., *Effect of Sm substitution on ferroelectric and magnetic properties of $BiFeO_3$*. Scripta Materialia, **2010**, 62 (5), p. 238-241.

[20] Arnold D.C., *Composition-Driven Structural Phase Transitions in Rare-Earth-Doped $BiFeO_3$ Ceramics: A Review*. Ieee Transactions on Ultrasonics Ferroelectrics and Frequency Control, **2015**, 62 (1), p. 62-82.

[21] Nalwa K.S. and Garg A., *Phase evolution, magnetic and electrical properties in Sm-doped bismuth ferrite*. Journal of Applied Physics, **2008**, 103 (4).

[22] Iorgu A.I., Maxim F., Matei C., Ferreira L.P., Ferreira P., Cruz M.M. and Berger D., *Fast synthesis of rare-earth (Pr^{3+}, Sm^{3+}, Eu^{3+} and Gd^{3+}) doped bismuth ferrite powders with enhanced magnetic properties*. Journal of Alloys and Compounds, **2015**, 629, p. 62-68.

[23] Perejon A., Maso N., West A.R., Sanchez-Jimenez P.E., Poyato R., Criado J.M. and Perez-Maqueda L.A., *Electrical Properties of Stoichiometric $BiFeO_3$ Prepared by Mechanosynthesis with Either Conventional or Spark Plasma Sintering*. Journal of the American Ceramic Society, **2013**, 96 (4), p. 1220-1227.

[24] Perejon A., Murafa N., Sanchez-Jimenez P.E., Criado J.M., Subrt J., Dianez M.J. and Perez-Maqueda L.A., *Direct mechanosynthesis of pure $BiFeO_3$ perovskite nanoparticles: reaction mechanism*. Journal of Materials Chemistry C, **2013**, 1 (22), p. 3551-3562.

[25] Perejon A., Sanchez-Jimenez P.E., Perez-Maqueda L.A., Criado J.M., de Paz J.R., Saez-Puche R., Maso N. and West A.R., *Single*

phase, electrically insulating, multiferroic La-substituted $BiFeO_3$ prepared by mechanosynthesis. Journal of Materials Chemistry C, **2014**, 2 (39), p. 8398-8411.

[26] Perejon A., Gil-Gonzalez E., Sanchez-Jimenez P.E., Criado J.M. and Perez-Maqueda L.A., *Structural, Optical, and Electrical Characterization of Yttrium-Substituted $BiFeO_3$ Ceramics Prepared by Mechanical Activation*. Inorganic Chemistry, **2015**, 54 (20), p. 9876-9884.

[27] Shannon R.D., *Revised effective ionic-radii and systematic studies of interatomic distances in halides and chalcogenides.* Acta Crystallographica Section A, **1976**, 32 (SEP1), p. 751-767.

[28] Catalan G. and Scott J.F., *Physics and Applications of Bismuth Ferrite*. Advanced Materials, **2009**, 21 (24), p. 2463-2485.

[29] Li J.B., Rao G.H., Xiao Y., Liang J.K., Luo J., Liu G.Y. and Chen J.R., *Structural evolution and physical properties of $Bi_{1-x}Gd_xFeO_3$ ceramics*. Acta Materialia, **2010**, 58 (10), p. 3701-3708.

[30] Palai R., Katiyar R., Schmid H., Tissot P., Clark S., Robertson J., Redfern S., Catalan G. and Scott J., *β phase and γ-β metal-insulator transition in multiferroic $BiFeO_3$*. Physical Review B, **2008**, 77 (1), p. 014110.

[31] Chen X., Wang Y., Yang Y., Yuan G., Yin J. and Liu Z., *Structure, ferroelectricity and piezoelectricity evolutions of $Bi_{1-x}Sm_xFeO_3$ at various temperatures*. Solid State Communications, **2012**, 152 (6), p. 497-500.

[32] Yang Y., Yu-Long L., Ke Z., Li-Yan Z., Shu-Yuan M., Jie L. and Yi-Jian J., *Structural properties of $Bi_{1-x}La_xFeO_3$ studied by micro-Raman scattering*. Chinese Phys. B, **2010**, 19.

[33] Hu W., Chen Y., Yuan H., Li G., Qiao Y., Qin Y. and Feng S., *Structure, Magnetic, and Ferroelectric Properties of $Bi_{1-x}Gd_xFeO_3$ Nanoparticles*. Journal of Physical Chemistry C, **2011**, 115 (18), p. 8869-8875.

[34] Arnold D.C., Knight K.S., Morrison F.D. and Lightfoot P., *Ferroelectric-Paraelectric Transition in BiFeO3: Crystal Structure of the Orthorhombic beta Phase*. Physical Review Letters, **2009**, 102 (2), p. 4.

[35] Verma V., *Structural, electrical and magnetic properties of rare-earth and transition element co-doped bismuth ferrites*. Journal of Alloys and Compounds, **2015**, 641, p. 205-209.

[36] Arora M. and Kumar M., *Electron spin resonance probed enhanced magnetization and optical properties of Sm doped $BiFeO_3$ nanoparticles*. Materials Letters, **2014**, 137, p. 285-288.

[37] Nguyen V.M. and Dao V.T., *Multiferroic materials $Bi_{1-x}Sm_xFeO_3$: A study of Raman and absorption spectroscopies*. Journal of Nonlinear Optical Physics & Materials, **2010**, 19 (2), p. 247-254.

[38] Jonsher A.K., *Universal relaxation law*. **1996**, London: Chelsea Dielectric Press.

[39] Da Silva K.L., Menzel D., Feldhoff A., Kübel C., Bruns M., Paesano A., Düvel A., Wilkening M., Ghafari M., Hahn H., Litterst F.J., Heitjans P., Becker K.D. and Šepelák V., *Mechanosynthesized $BiFeO_3$ nanoparticles with highly reactive surface and enhanced magnetization*. Journal of Physical Chemistry C, **2011**, 115 (15), p. 7209-7217.

[40] Freitas V.F., Grande H.L.C., de Medeiros S.N., Santos I.A., Cótica L.F. and Coelho A.A., *Structural, microstructural and magnetic investigations in high-energy ball milled $BiFeO_3$ and $Bi_{0.95}Eu_{0.05}FeO_3$*

powders. Journal of Alloys and Compounds, **2008**, 461 (1–2), p. 48-52.

[41] Sharma P., Satapathy S., Varshney D. and Gupta P.K., *Effect of sintering temperature on structure and multiferroic properties of $Bi_{0.825}Sm_{0.175}FeO_3$ ceramics*. Materials Chemistry and Physics, **2015**, 162, p. 469-476.

[42] Dai H., Chen Z., Xue R., Li T., Liu H. and Wang Y., *Structure and multiferroic properties of Eu-substituted $BiFeO_3$ ceramics*. Applied Physics A, **2013**, 111 (3), p. 907-912.

[43] Yan Z., Wang K.F., Qu J.F., Wang Y., Song Z.T. and Feng S.L., *Processing and properties of Yb-doped $BiFeO_3$ ceramics*. Applied Physics Letters, **2007**, 91 (8).

[44] Sati P.C., Kumar M., Chhoker S. and Jewariya M., *Influence of Eu substitution on structural, magnetic, optical and dielectric properties of $BiFeO_3$ multiferroic ceramics*. Ceramics International, **2015**, 41 (2, Part A), p. 2389-2398.

[45] Dhanalakshmi R., Muneeswaran M., Shalini K. and Giridharan N.V., *Enhanced photocatalytic activity of La-substituted $BiFeO_3$ nanostructures on the degradation of phenol red*. Materials Letters, **2016**, 165, p. 205-209.

[46] Jia D.-C., Xu J.-H., Ke H., Wang W. and Zhou Y., *Structure and multiferroic properties of $BiFeO_3$ powders*. Journal of the European Ceramic Society, **2009**, 29 (14), p. 3099-3103.

[47] Yan X., Chen J., Qi Y., Cheng J. and Meng Z., *Hydrothermal synthesis and characterization of multiferroic $Bi_{1-x}La_xFeO_3$ crystallites*. Journal of the European Ceramic Society, **2010**, 30 (2), p. 265-269.

[48] Luo L., Wei W., Yuan X., Shen K., Xu M. and Xu Q., *Multiferroic properties of Y-doped $BiFeO_3$*. Journal of Alloys and Compounds, **2012**, 540, p. 36-38.

6. FLASH SINTERING OF $BiFeO_3$

6.1. INTRODUCTION

The synthesis methods employed to prepare $BiFeO_3$, including mechanochemistry, usually yield particulate samples that should be sintered to get dense high purity pellets as required for many applications. Conventional sintering relies on high temperature and, very often, long treatments to achieve full densification. It can be particularly tricky for $BiFeO_3$ and related materials, as it may lead to the presence of secondary phases and undesired stoichiometry or microstructure. Thus, alternative procedures have been proposed for the sintering of $BiFeO_3$ and related materials, such as rapid liquid phase sintering [1, 2] or Spark Plasma Sintering (SPS) [3-12]. The current-activated SPS method has been proven to be a very useful sintering technique for $BiFeO_3$ and related materials, because it yields high density samples with fine grains at lower temperatures avoiding the degradation of the material. Nevertheless, the reducing SPS conditions (vacuum, graphite die, high DC current) yield densified $BiFeO_3$ pellets with very low resistivity due to sample reduction that requires further oxidation treatments to increase such low resistivity. Thus, exploring an alternative electric-assisted method of sintering, such as flash sintering (described in Section 1.4.3), is of the most interest, because the major drawbacks of SPS, such as the highly reducing conditions, are in principle avoided.

6.2. OBJECTIVES

The scope of this chapter is to explore the densification of mechanosynthesized powders of the perovskite oxide $BiFeO_3$ by flash sintering. The effects of experimental parameters, such as the applied electric field, the current and the flash temperature threshold on the purity, density and microstructure of the flash-sintered samples are investigated.

6.3. EXPERIMENTAL

Powders samples of $BiFeO_3$ were prepared by mechanosynthesis according to the procedure described in Section 3.2.1 (Chapter 3), using the planetary Micro mill Pulverisette 7 Premium Line. Eight hours of milling were required to obtain the final product [13]. Then, the powders were uniaxially pressed at 250 MPa into dog-bone-shaped green bodies. As an example, Figure 6. 1 shows a $BiFeO_3$ dog-bone-shaped green body with platinum paste in the holes and handles.

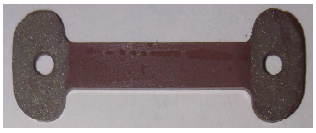

Figure 6. 1. Dog-bone-shaped green body.

Subsequently, the green bodies were flash-sintered following the protocol detailed in Section 3.2.2 (Chapter 3). For this purpose, they were suspended in the centre of a tubular furnace by means of two platinum wires attached to the handles of the dog-boned-shaped specimens. The furnace temperature was linearly increased at 10 $^{o}C\ min^{-1}$ up to the flash

event. A DC electric field was applied through the two platinum wires and was maintained constant up to the point of the flash event, which was signalled by a non-linear rise in conductivity. The power supply was switched from the voltage controlled mode to current controlled mode when the current reached the preset limit. Constant current was held for 15 seconds approximately before the power supply was switched off. At this point, the furnace was turned off. A total of five experiments were performed at electric fields of 0 (conventional sintering), 15, 50, 100 and 150 V cm^{-1}. The current limit for the 150 and 100 V cm^{-1} runs was set at 20 mA mm^{-2}, while for the 50 and 15 V cm^{-1} runs was set at 40 mA mm^{-2}.

6.4. RESULTS AND DISCCUSION

6.4.1. Flash sintering of mechanosynthesised $BiFeO_3$

Figure 6. 2 shows an example of a flash sintering experiment of the mechanosynthesised $BiFeO_3$ sample. The electric field applied across the specimen gage length at the start of the experiment was 100 V cm^{-1} while the furnace was heated at a constant rate of 10 °C min^{-1}. The three stages of a flash sintering experiment can be clearly observed [14]. In stage I, the current intensity rises slowly while a constant electrical bias (E=100 V cm^{-1}) is applied. As expected for a ceramic material, the resistivity of the sample decreases with the increasing temperature. In stage II the flash event takes place. The current intensity (J) across the sample suffers a sharp non-linear increase up to the predefined intensity limit, which in this experiment was set to 20 mA mm^{-2}. Most of the sample densification takes place during this stage II, as shown in Figure 6. 2 b) that includes the evolution of both shrinkage, $\Delta L/L_0$, and power density dissipated, P, (appraised as $P = J\ E$) as a function of the furnace temperature. At this

point, the power supply switches to current-controlled mode and Stage III, characterized by a constant state of flash, begins. Stage III was held for approximately 15 seconds.

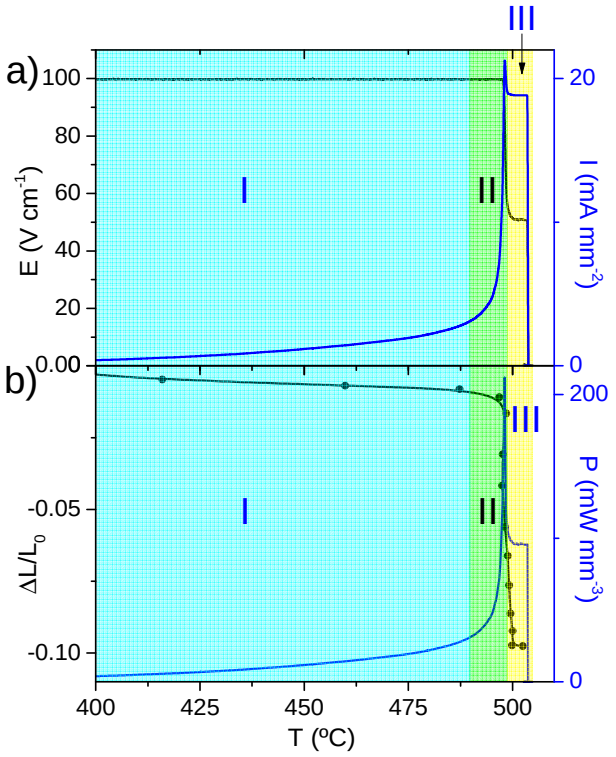

Figure 6. 2. a) Evolution of electrical field, E, and current intensity, I, and b) evolution of linear shrinkage, $\Delta L/L_0$, and dissipated electrical power, P, as a function of furnace temperature for a flash sintering experiment of a $BiFeO_3$ sample under linear heating rate conditions (10^o C min^{-1}) at a constant electrical field of 100 V cm^{-1} and a limit current intensity of 20 mA mm^{-2}.

The linear shrinkage and power dissipation curves obtained for different applied DC fields for $BiFeO_3$, including the data for conventional sintering at 0 V cm^{-1}, are presented in Figures 6. 3 a) and b), respectively.

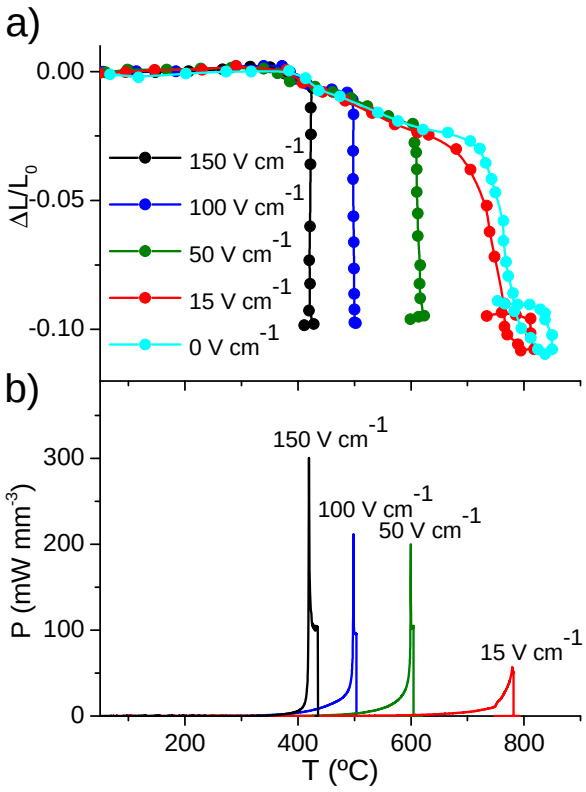

Figure 6. 3 Sintering curves for a) linear shrinkage, $\Delta L/L_0$, and b) power dissipation, P, measured at different applied DC fields in experiments carried out at constant heating rate (10 ^{o}C min^{-1}).

Final densities of pellets, as measured by Archimedes method, were for all studied conditions within the 91-92% range. Low applied DC field, such as 15 V cm^{-1}, has little effect on the sintering behavior and the densification curve is just slightly shifted to lower temperatures as compared with the conventionally sintered experiment. This behavior is known as field-assisted sintering (FAST) [15-19]. Conversely, higher applied DC fields (50, 100 and 150 V cm^{-1}) produce significant shifts in the densification curves to lower temperatures and acceleration of the

densification. For these higher applied DC fields, the densification takes place in two steps. Initially, the sample sinters at a lower rate in a FAST regime followed by a FLASH regime where the shrinkage takes place within seconds and there is a sharp increase in the current intensity up to the selected limit (20 mA mm^{-2}) that corresponds to the maximum dissipated power in Figure 6. 3 b). The contribution of the FLASH to the overall sintering (measured as the ratio to total shrinkage) is very much dependent on the field (Figure 6. 4). Thus, for the experiment at 15 V cm^{-1} the process is pure FAST while for those at higher voltages the contribution of FLASH is predominant and its contribution to the overall densification increases with the applied field.

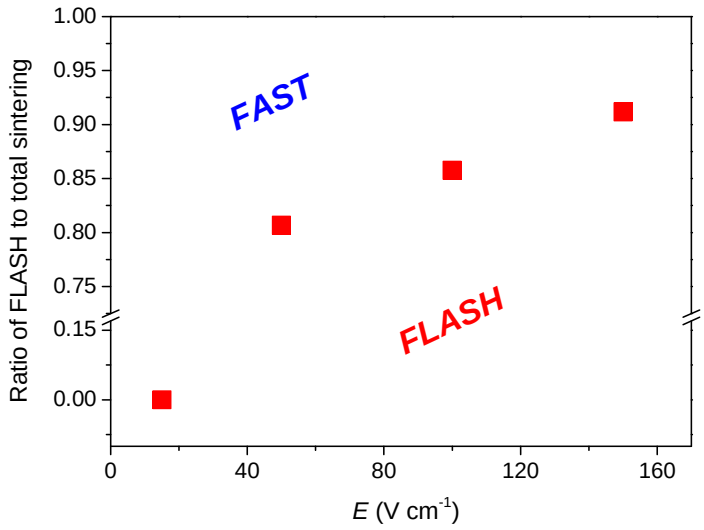

Figure 6. 4. Contribution of the FLASH to the overall sintering (measured as the ratio to total shrinkage) as a function of the applied DC field.

Another interesting feature of these experiments is related to the onset temperature for the FLASH effect. As shown in Figure 6. 5, there is a linear dependence of the logarithm of the applied DC field, $ln(E)$, and the

inverse of the onset temperature for the FLASH, $1/T_{on}$, in agreement with the postulate of Dong et al. [20]. For the 15 V cm^{-1} experiment, the temperature at which the sintering is completed has also been shown in Figure 6. 5. This temperature is way below that required for triggering the FLASH, that according to the linear relation in Figure 6. 5 should be about 1000 ºC (this point has been marked with a star in Figure 6. 5), although below this temperature the densification has been completed, as can be seen in Figure 6. 3 a).

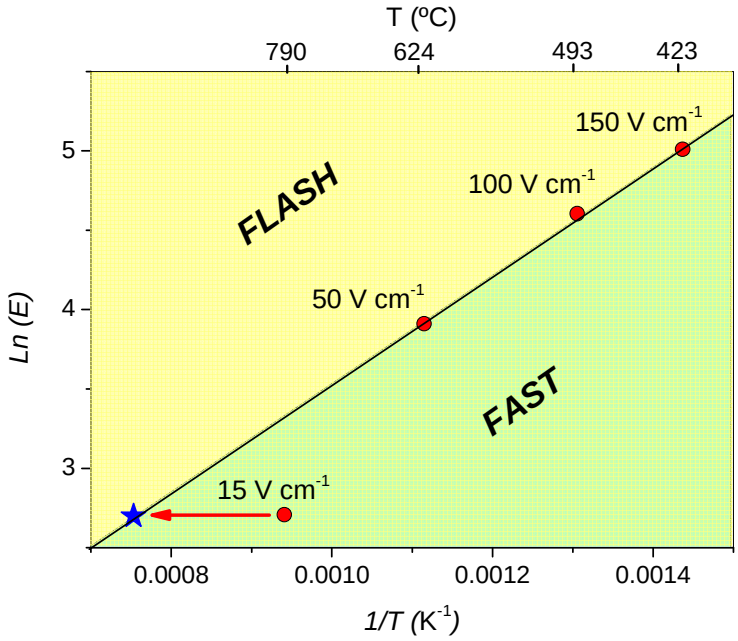

Figure 6. 5. Dependence of the logarithm of the applied DC field, *ln(E)*, and the inverse onset temperature for the FLASH, $1/T_{on}$. FLASH and FAST regimes have been marked in the figure.

6.4.2. Structural characterization

Figure 6. 6 includes the X-ray diffraction data from the mechanosynthesized $BiFeO_3$ samples sintered under different applied DC fields. The effect of the electric field on the structural composition of the samples is very significant. The sample sintered at the lowest electric field (15 V cm^{-1}), which showed a pure FAST sintering behavior, has a significant amount of secondary phases in its composition. Conversely, samples sintered at higher electric fields (50-150 V cm^{-1}), which showed mostly FLASH sintering behavior, consist of pure R3c perovskite phase, free of secondary phases, as shown in the X-ray diffraction patterns in Figure 6. 6. Thus, sintering conditions have a clear effect on the phase composition of the resulting materials, being FLASH the optimum conditions for obtaining phase-pure compositions.

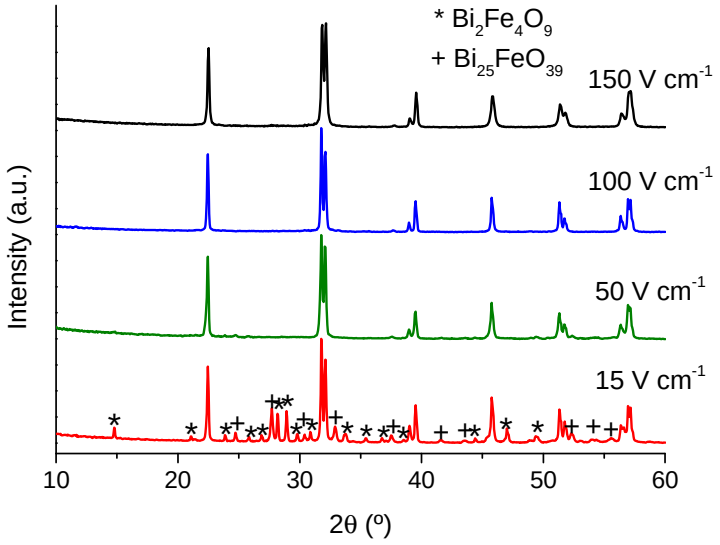

Figure 6. 6. X-ray diffraction patterns of mechanosynthesized $BiFeO_3$ samples sintered at different applied DC fields. Diffraction peaks corresponding to secondary phases have been marked while all other main peaks correspond to the $BiFeO_3$ perovskite phase R3c.

6.4.3.Microstructural characterization

Microstructure of flash sintered samples of $BiFeO_3$ under applied DC fields of 100 V cm^{-1} and 50 V cm^{-1} were characterized by means of SEM, as shown in Figures 6. 7 a) and d), respectively. It is noteworthy that under these flash sintering conditions, they resulted to be phase-pure, unlike samples sintered at lower fields. The microstructures of both samples correspond to well-sintered materials with low porosity. The grain size distributions in both cases were estimated by ImageJ software [21]. They are presented in histogram graphs in Figures 6.7. b) and e). The sample sintered at 100 V cm^{-1} and a current density limit of 20 mA mm^2 has an average grain size of approximately 20 $\pm$ 6 nm and a narrow grain size distribution (from 11 nm to 34 nm) where 61% of the grains have a size between 11 nm and 20 nm. More grain growth is observed for the sample sintered at 50 V cm^{-1} and a current density limit of 40 mA mm^{-2} (Figure 6. 7 d)) as compared to that sintered at 100 V cm^{-1} and a current density limit of 20 mA mm^{-2} (Figure 6. 7 a)). It may be due to the effect of the current density, in agreement with Francis et al. [22] who showed that higher current density causes more grain growth in 3mol% yttria-stabilized zirconia. From Figure 6. 7 e) can be inferred that in this case 100% of the grains are ranging from 22 nm to 95 nm, with an average value of 42 $\pm$ 15 nm. Likewise for the sample sintered at 100 V cm^{-1}, the grain size distribution is quite uniform, as approximately 77% of the grains have a size between 22 nm and 50 nm. The chemical compositions of the flash sintered specimens, as determined by EDX (Figures 6. 7 c) and f)), are included in Table 6. 1. They correspond to the nominal stoichiometric compositions.

Thus, it is remarkable that the experimental conditions employed in the flash sintering technique give rise to stoichiometric, well-sintered $BiFeO_3$ ceramics with an uniform nanometric grain size distribution.

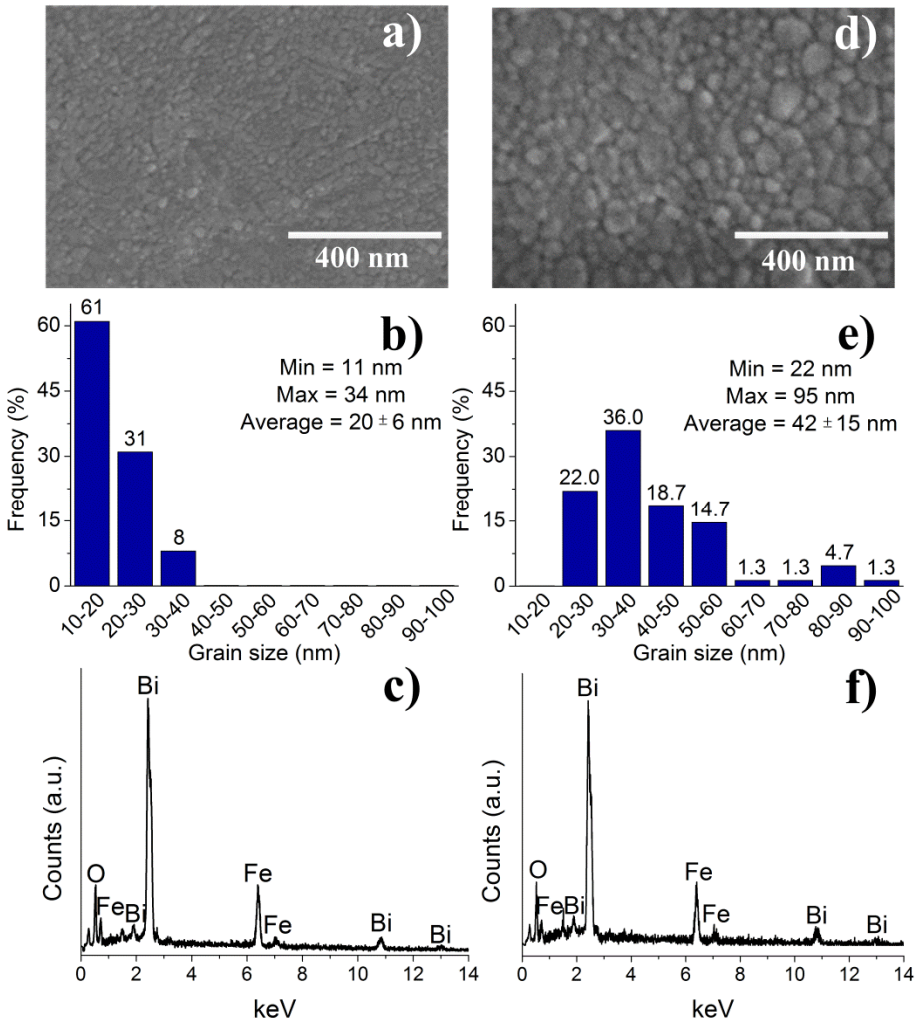

Figure 6. 7. SEM micrographs, grain size distribution histograms and EDX spectra for $BiFeO_3$ samples flash sintered under 100 V cm^{-1} and 20 mA mm^{-2} (a), b) and c)) and 50 V cm^{-1} and 40 mA mm^{-2} (d), e) and f)).

Table 6. 1. Nominal stoichiometric and experimental atomic compositions of the flash sintered $BiFeO_3$ samples.

		Experimental atomic composition (%)	
Sample $BiFeO_3$	Theoretical atomic composition Fe/Bi (%)	Fe	Bi
(100 V cm^{-1},20 mA mm^2)	50/50	51.92±3.05	48.08±2.97
(50 V cm^{-1}, 40 mA mm^{-2})	50/50	50.95±2.68	49.05±3.45

6.4.4. Electrical properties

The electrical properties of the flash sintered $BiFeO_3$ samples that resulted to be single-phase (150 V cm^{-1}, 100 V cm^{-1} and 50 V cm^{-1}) were measured by impedance spectroscopy. Due to the similarities found in the electrical properties of the samples, just the results for the flash sintered sample at 100 V cm^{-1} and 20 mA mm^{-2} are depicted in Figure 6. 8, as a way of example.

The sample resulted to be highly insulating at room temperature, presenting modest levels of semiconductivity above 300 ºC. Thus, impedance spectroscopy data were recorded from 300 ºC to 380 ºC, this upper limit being constrained by the gold coating which served as the electrodes. Figure 6. 8 a) shows the complex impedance plane plots at different temperatures, which are composed by single, semicircular arcs. This is an evidence of the electrical homogeneity of the sample. Additionally, the imaginary parts of the modulus, M'', and the impedance, Z'', as a function of frequency at 300 ºC are plotted in Figure 6. 8 b). Two single peaks with a very small displacement in their frequency maxima were obtained, newly indicating that the flash sintered $BiFeO_3$ sample is electrically homogeneous. The capacitance values, calculated from the imaginary part of the impedance, are shown in Figure 6. 8 c). They remain approximately constant in the entire frequency range with a value of ~10

pF cm^{-1}, which correspond to the bulk response of the sample. Thus, the electrical homogeneity of the sample is again evidenced. The permittivity was calculated by dividing the capacity by the permittivity of free space, resulting to be equal to 113.

Figure 6. 8 d) presents the bulk conductivity data in Arrhenius format for the flash sintered $BiFeO_3$. The activation energy was 1.11 eV, being within the range of the values reported for high quality single crystals, 1.3 eV [23]. The room temperature resistivity, extrapolated from the Arrhenius plot was $6x10^{14}$ Ω cm.

Thus, it can be concluded that flash sintered samples of $BiFeO_3$ ceramics resulted to be electrically homogenous and highly insulating at room temperature. Conversely, previous results of $BiFeO_3$ samples sintered by SPS, showed that the specimens presented lower resistance and were electrically inhomogeneous [10, 24-27]. This highlights the validity of flash sintering, as compared to other techniques, for the processing of complex oxides with low thermal stability.

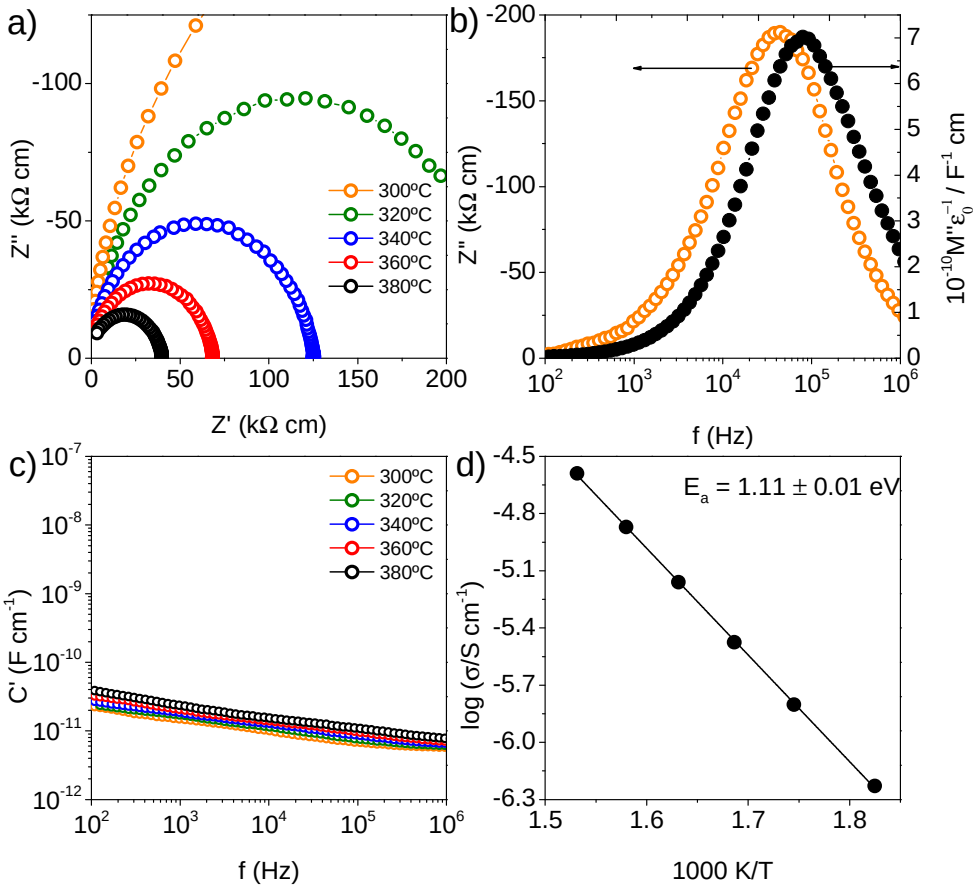

Figure 6. 8. a) Impedance complex plane plots, b) Z''/M'' spectroscopic plots at 300 ºC, c) C' versus frequency and d) bulk Arrhenius plot for $BiFeO_3$ obtained by mechanosynthesis and flash sintered at 100 V cm^{-1} and 20 mA mm^{-2}.

6.5. CONCLUSIONS

Flash sintering has been proven to be a useful technique for the densification of $BiFeO_3$, which decomposes and produces secondary phases during the high temperatures and long processing times that are normally required in conventional sintering. It has been shown that flash

sintering leads to dense, pure and stoichiometric $BiFeO_3$ materials, where the grain size of the flash sintered specimens is nanometric. The electrical properties of the flash sintered $BiFeO_3$ samples were measured by impedance spectroscopy. They resulted to be essentially electrically homogeneous and highly insulating at room temperature, unlike $BiFeO_3$ samples sintered by SPS. It is probably due to the fact that experimental conditions are not so severe and the atmosphere in the surrounding of the sample can be controlled. Therefore, flash sintering technique is presented as a very useful procedure for processing complex oxides with low thermal stability.

6.6. REFERENCES

[1] Wang Y.P., Zhou L., Zhang M.F., Chen X.Y., Liu J.M. and Liu Z.G., *Room-temperature saturated ferroelectric polarization in $BiFeO_3$ ceramics synthesized by rapid liquid phase sintering*. Applied Physics Letters, **2004**, 84 (10), p. 1731-1733.

[2] Yuan G.L., Or S.W., Wang Y.P., Liu Z.G. and Liu J.M., *Preparation and multi-properties of insulated single-phase $BiFeO_3$ ceramics*. Solid State Communications, **2006**, 138 (2), p. 76-81.

[3] Wang L.C., Wang Z.H., He S.L., Li X., Lin P.T., Sun J.R. and Shen B.G., *Enhanced magnetization and suppressed current leakage in $BiFeO_3$ ceramics prepared by spark plasma sintering of solgel derived nanoparticles*. Physica B: Condensed Matter, **2012**, 407 (8), p. 1196-1202.

[4] Correas C., Hungría T. and Castro A., *Mechanosynthesis of the whole $xBiFeO_3$-(1-x)$PbTiO_3$ multiferroic system: Structural characterization*

and study of phase transitions. Journal of Materials Chemistry, **2011**, 21 (9), p. 3125-3132.

[5] Dai Z. and Akishige Y., *Electrical properties of multiferroic $BiFeO_3$ ceramics synthesized by spark plasma sintering*. Journal of Physics D: Applied Physics, **2010**, 43 (44).

[6] Mazumder R., Chakravarty D., Bhattacharya D. and Sen A., *Spark plasma sintering of $BiFeO_3$*. Materials Research Bulletin, **2009**, 44 (3), p. 555-559.

[7] Jiang Q.H., Nan C.W., Wang Y., Liu Y.H. and Shen Z.J., *Synthesis and properties of multiferroic $BiFeO_3$ ceramics*. Journal of Electroceramics, **2008**, 21 (1-4), p. 690-693.

[8] Jiang Q.H., Ma J., Lin Y.H., Nan C.W., Shi Z. and Shen Z.J., *Multiferroic properties of $Bi_{0.87}La_{0.05}Tb_{0.08}FeO_3$ ceramics prepared by spark plasma sintering*. Applied Physics Letters, **2007**, 91 (2).

[9] Perejon A., Gil-Gonzalez E., Sanchez-Jimenez P.E., Criado J.M. and Perez-Maqueda L.A., *Structural, Optical, and Electrical Characterization of Yttrium-Substituted $BiFeO_3$ Ceramics Prepared by Mechanical Activation*. Inorganic Chemistry, **2015**, 54 (20), p. 9876-9884.

[10] Perejón A., Masó N., West A.R., Sánchez-Jiménez P.E., Poyato R., Criado J.M. and Pérez-Maqueda L.A., *Electrical Properties of Stoichiometric $BiFeO_3$ Prepared by Mechanosynthesis with Either Conventional or Spark Plasma Sintering*. Journal of the American Ceramic Society, **2013**, 96 (4), p. 1220-1227.

[11] Song S.H., Zhu Q.S., Weng L.Q. and Mudinepalli V.R., *A comparative study of dielectric, ferroelectric and magnetic properties of*

$BiFeO_3$ multiferroic ceramics synthesized by conventional and spark plasma sintering techniques. Journal of the European Ceramic Society, **2015**, 35 (1), p. 131-138.

[12] Correas C., Jiménez R., Hungría T., Amorin H., Ricote J., Vila E., Algueró M., Castro A. and Galy J., *Spark plasma sintering of nanostructured ceramic materials with potential magnetoelectricity*. Ceramic Transactions. **Vol**. 212. **2010**. 41-53.

[13] Perejon A., Murafa N., Sanchez-Jimenez P.E., Criado J.M., Subrt J., Dianez M.J. and Perez-Maqueda L.A., *Direct mechanosynthesis of pure $BiFeO_3$ perovskite nanoparticles: reaction mechanism*. Journal of Materials Chemistry C, **2013**, 1 (22), p. 3551-3562.

[14] Jha S.K., Terauds K., Lebrun J.-M. and Raj R., *Beyond flash sintering in 3 mol % yttria stabilized zirconia*. Journal of the Ceramic Society of Japan, **2016**, 124 (4), p. 283-288.

[15] Orrù R., Licheri R., Locci A.M., Cincotti A. and Cao G., *Consolidation/synthesis of materials by electric current activated/assisted sintering*. Materials Science and Engineering: R: Reports, **2009**, 63 (4–6), p. 127-287.

[16] Munir Z.A., Anselmi-Tamburini U. and Ohyanagi M., *The effect of electric field and pressure on the synthesis and consolidation of materials: A review of the spark plasma sintering method*. Journal of Materials Science, **2006**, 41 (3), p. 763-777.

[17] Garay J.E., *Current-Activated, Pressure-Assisted Densification of Materials*. Annual Review of Materials Research, **2010**, 40 (1), p. 445-468.

[18] Suarez M., Fernandez A., Menendez J.L., Torrecillas R., U H., Hennicke J., Kirchner R. and Kessel T., *Challenges and Opportunities for Spark Plasma Sintering: A Key Technology for a New Generation of Materials*. **2013**.

[19] Grasso S., Sakka Y., Rendtorff N., Hu C., Maizza G., Borodianska H. and Vasylkiv O., *Modeling of the temperature distribution of flash sintered zirconia*. Journal of the Ceramic Society of Japan, **2011**, 119 (1386), p. 144-146.

[20] Dong Y., Chen I.W. and Gaukler L., *Predicting the Onset of Flash Sintering*. Journal of the American Ceramic Society, **2015**, 98 (8), p. 2333-2335.

[21] *ImageJ*. **2016**. p. https://imagej.net/.

[22] Francis J.S.C. and Raj R., *Influence of the Field and the Current Limit on Flash Sintering at Isothermal Furnace Temperatures*. Journal of the American Ceramic Society, **2013**, 96 (9), p. 2754-2758.

[23] Catalan G. and Scott J.F., *Physics and Applications of Bismuth Ferrite*. Advanced Materials, **2009**, 21 (24), p. 2463-2485.

[24] Garcia-Zaleta D.S., Torres-Huerta A.M. and Dominguez-Crespo M.A., *Synthesis of Dense Fine-Grained Ceramics by Sol-Gel Technique of RE-substituted $Bi_{1-x}A_{(x)}FeO_3$ Nanopowders (A = La^{3+}, Y^{3+}, Dy^{3+}, Ce^{3+}): Structural, Electrical, and Magnetic Characterization*. Metallurgical and Materials Transactions a-Physical Metallurgy and Materials Science, **2016**, 47A (4), p. 1720-1728.

[25] Wang T., Song S.H., Wang M., Li J.Q. and Ravi M., *Effect of annealing atmosphere on the structural and electrical properties of $BiFeO_3$ multiferroic ceramics prepared by sol-gel and spark plasma*

sintering techniques. Ceramics International, **2016**, 42 (6), p. 7328-7335.

[26] Perejon A., Sanchez-Jimenez P.E., Poyato R., Maso N., West A.R., Criado J.M. and Perez-Maqueda L.A., *Preparation of phase pure, dense fine grained ceramics by conventional and spark plasma sintering of La-substituted $BiFeO_3$ nanoparticles*. Journal of the European Ceramic Society, **2015**, 35 (8), p. 2283-2293.

[27] Dai Z.H. and Akishige Y., *Electrical properties of multiferroic $BiFeO_3$ ceramics synthesized by spark plasma sintering*. Journal of Physics D-Applied Physics, **2010**, 43 (44).

9. GENERAL CONCLUSIONS

- Ytterbium-substituted $BiFeO_3$ samples ($Bi_{1-x}Yb_xFeO_3$) were prepared by mechanosynthesis followed by conventional sintering. Based on the XRD patterns and DSC data, it was found that the ytterbium solubility in the $Bi_{1-x}Yb_xFeO_3$ system is limited to approximately x = 0.03. Samples with nominal x > 0.03 present the main R3c phase together with ytterbium enriched secondary phases. The multiferroic behaviour of the samples has been studied by DSC and X-ray thermodiffraction. The UV-Vis measurements suggested the potential use of the samples in photocatalytic applications. Electrical measurements show that samples are electrically homogeneous and highly insulated at room temperature. The magnetic data interpretation is hampered by the presence of the secondary ytterbium-rich phase.

- High-quality samples of the $Bi_xSm_{1-x}FeO_3$ system ($0.05 \leq x \leq 0.2$) have been successfully prepared by direct mechanosynthesis. Rietveld refinements demonstrate that single phase ceramics were obtained for x = 0.05, 0.10, 0.15 and 0.20 compositions and two phase mixtures for x = 0.125 and 0.175. A tentative phase diagram has been proposed from the information extracted by the Rietveld refinements, TEM, DSC, temperature-dependent XRD and permittivity data. Moreover, the high temperature Pnma phase for the $Bi_xSm_{1-x}FeO_3$ system has been confirmed as well. The potential use of the samples in photocatalytic applications has been also